Growth and Characterization of cubic AlGaN/GaN based Devices

Dem Department Physik
der Universität Paderborn
zur Erlangung des akademischen Grades eines

Doktors der Naturwissenschaften

vorgelegte

Dissertation

von

Stefan Potthast

Paderborn, November 2006

Abstract

Cubic GaN and AlGaN layers are grown by radio frequency plasma assisted molecular beam epitaxy on freestanding 3C-SiC (001) substrates. Detailed analysis of the substrate quality reveal a direct dependence of the roughness of the 3C-SiC on the dislocation density. Additionally a strong influence of the substrate quality on the quality of cubic GaN layers is found. GaN, AlGaN and AlN buffer layers grown at different temperatures are used to improve the structural properties of the c-GaN buffer. Best values are obtained for AlN buffers deposited at $T_{Subs} = 720°C$. Furthermore, the growth temperature of the buffer itself is varied. Optimized results are found for $T_{Subs} = 720°C$ grown under a Ga coverage of one monolayer. On top of the GaN buffer, AlGaN films $(0 < x < 0.74)$ are grown using Ga coverages of one monolayer and much greater than one monolayer. A linear dependence between the Al metal flux and the Al mole fraction is measured. Investigation of the growth front using reflection high energy electron diffraction as a probe, show a predominant two-dimensional growth mode. With increasing Al mole fraction, a change in the resistivity of the AlGaN layer is observed due to the gettering of oxygen by aluminum and the variation of the oxygen ionization energy as a function of the Al content. Schottky diodes are fabricated on GaN and AlGaN using nickel as contact material. A strong deviation of the current voltage characterisitics from thermionic emission theory is found, measuring anormal high leakage current, caused by the presence of oxygen donors near the surface. It is investigated, that thermal annealing in air reduces the reverse current by three orders of magnitude. AlGaN/GaN are used to fabricate heterojunction field effect transistor structures. Analysis of the capacitance-voltage characteristics at T=150 K revealed clear evidence for the existence of a two-dimensional electron gas, and a sheet carrier concentration of about $1.6x10^{12}cm^{-2}$ is measured at the interface in good agreement with the numerical simulation. The source-drain current source-drain voltage characteristics measured at 155 K exhibit a clear field effect of source-drain current induced by the gate voltage. A strong influence of the conductive buffer on the source-drain current source-drain voltage characteristics is observed. Neglecting this influence, a clear evidence for the current transport via a two-dimensional electron gas is found.

List of Figures

2.1 The zincblende structure of cubic GaN. 2
2.2 Heteroepitaxy: a) separated layers b)strained c)relaxed with incorporation of defects. 3
2.3 Critical thickness of $c - Al_xGa_{1-x}N$ on c-GaN as function of the Al mole fraction x on GaN. 4
2.4 Schematic drawing of the materials research diffractometer system. . . . 7
2.5 Schematic drawing of the Photoluminescence spectroscopy system. 9
2.6 Schematic drawing of the I-V measurement setup. 10
2.7 Schematic drawing of the C-V measurement setup. 11
2.8 Schematic drawing of the temperature dependence of carrier mobility for bulk material (solid line) and a two-dimensional electron gas (2DEG) (dashed line). 12
2.9 Schematic drawing of the contact arrangement and the current flow during a four-point probe measurement. 14

3.1 Schematic drawing of the structure of the investigated c-GaN layers. . . . 16
3.2 Measured RHEED intensity during the initial growth of c-GaN. The RHEED intensity after opening the N shutter yields the amount of excess Ga on the c-GaN surface. 17
3.3 Terrace width of a c-GaN film. 19
3.4 RMS roughness on a $5x5\mu m^2$ scan range as function of the FWHM of the X-ray rocking curve for $\phi = 0°$ (triangles) and $\phi = 90°$ (squares) of the freestanding 3C-SiC substrates. 19
3.5 The FWHM of the X-ray rocking curve of c-GaN as function of the SiC RMS roughness on a $5x5\mu m^2$ scan range for $\phi = 0°$ (triangles) and $\phi = 90°$ (squares). 20
3.6 The RMS roughness of c-GaN as function of the SiC RMS roughness on a $5x5\mu m^2$ scan range. 21
3.7 The FWHM of the X-ray rocking curve of c-GaN as function of the buffer type. 22
3.8 The RMS roughness (circles) and the amount of hexagonal phase inclusion (squares) of c-GaN as function of the buffer type. 23
3.9 The FWHM of the X-ray rocking curve of c-GaN as function of substrate temperature. 24

3.10 The RMS roughness (circles) and the amount of hexagonal phase inclusion (squares) of c-GaN as function of the substrate temperature. 25
3.11 Measured RHEED intensity during the initial growth of $c-Al_{0.25}Ga_{0.75}N$. The RHEED intensity after opening the N shutter yields the amount of excess Ga on the c-GaN surface. After opening the Al shutter the excess of Ga increases and RHEED oscillations are observed indicating a two-dimensional growth mode with a rate of 177nm/h. 26
3.12 Relation between the Al mole fraction x of all $Al_xGa_{1-x}N$ and the flux ratio of Al to the total metal flux in the vapor phase for films grown under 1ML and >>1ML Ga coverage. The mole fraction was determined by HRXRD. 27
3.13 $Al_xGa_{1-x}N$ growth rate derived by RHEED oscillation and optical measurements for Al mole fraction between x=0 and x=0.74 at a constant nitrogen flux of $F_N = 2.2 * 10^{14} cm^{-2} s^{-1}$. The data reveal a constant growth rate for all AlxGa1-xN alloys independent on the Al flux. 28
3.14 RMS roughness on a 5x5μm^2 area for $Al_xGa_{1-x}N$ alloys with an Al mole fraction between x=0 and x=0.74 grown under the coverage of 1ML (circles) and >>1ML (triangles) at 720°C. The lines are a guide for the eyes. 29
3.15 Reciprocal Space Map arround the (-1-13) reflex of an $Al_{0.25}Ga_{0.75}N$ film. 30
3.16 Strain status of $Al_{0.25}Ga_{0.75}N$ films as function of the layer thickness. . . 30
3.17 Unintentional doping level of $Al_xGa_{1-x}N$ films as function of the Al content x before (circles) and after (squares) change of the purifier. 31
3.18 Photograph of the investigated AlGaN/GaN samples. 32
3.19 Equivalent current circle of the investigated AlGaN/GaN samples. 33
3.20 Relative conductance and carrier concentration as function of the Al mole fraction x. 34

4.1 Schematic drawing of the energy bands of a metal and a semiconductor before contact. 37
4.2 Schematic drawing of the energy bands of a metal and a semiconductor in contact. 37
4.3 Schematic draw of the carrier distribution, the electric field strength and the potential (from upside to downside). 40
4.4 Comparison of the IV curve of a real Ni/c-GaN Schottky diode (GNJ1204) (open circles) and an ideal diode using the Schotty-Mott equation (solid line). 41
4.5 Arrangement of the metal contact used for the c-GaN Schottky diodes (left side) and the equivalent circuit (right side). 42
4.6 Sketch of the circuit for a real Schottky diode under forward bias. 43
4.7 Comparision of the measured IV curve (full circles), without the limitation by the serial resistance (open circles) and the Schottky-Mott equation (solid line) in forward direction for GNJ1204. 44
4.8 Sketch of the circuit for a real Schottky diode under reverse bias. 45

4.9 Comparison of the measured I-V curve (full circles), eliminating the influence of R_S (open circles) and the calculation using the Schottky-Mott equation (solid line) in reverse direction for GNJ1204. 46
4.10 IV curves in forward direction measured at different temperatures of 300K (open circles), 150K (full circles) and 50K (open squares) of sample GNJ1204. 47
4.11 IV curves in reverse direction measured at different temperatures of 300K (open circles), 150K (full circles) and 50K (open squares) of GaN film (GNJ1204). 48
4.12 IV curves in reverse direction measured at different temperatures of 300K (open circles), 150K (full circles) and 50K (open squares) of a $GaN/Al_{0.35}Ga_{0.65}N/GaN$ heterostructure (GANS1352). 48
4.13 Temperature dependence of the Schottky barrier height calculated from the built-in voltage at different temperatures between 5K and 300K of a Ni/GaN (open squares)(GNJ1204) and a Pd/GaN/AlGaN/GaN (full circles) (GANS1352) Schottky diode. 49
4.14 Schematic sketch of the Thin Surface Barrier (TSB) model. 51
4.15 Schematic sketch of the formation of the current plateau in the forward direction of a Schottky diode. 52
4.16 Carrier concentration profile of a Pd/c-GaN/c-AlGaN/c-GaN Schottky diode (GANS1352) measured at temperatures between 175K and 350K. . 53
4.17 Room temperature current voltage characteristics of a Ni/c-GaN Schottky diode (GNS1285) before annealing (open circles) and after annealing in air at $200C$ (full circles). 54
4.18 Breakdown voltage of Ni/c-GaN Schottky diode before annealing (GNJ1204) (open circles) and after annealing in air at $200C$ (GNS1285) (full circles). 55
4.19 Breakdown voltages vs net donor concentration of Schottky diodes on c-GaN and c-AlGaN (full symbols) and h-GaN (open symbols). 56

5.1 Experimental setup for the investigation of the photoconductivity: a) sample structure b) contact arrangement. 58
5.2 IV curves of the Schottky contacts on a 750nm c-GaN measured (GNS1382) at T=300K. 59
5.3 IV curve of the Ni Schottky contacts (2)-(3) on a 750nm c-GaN (GNS1382) measured at T=300K. 60
5.4 Comparison of the IV curve measured in the darkness (open circles) and under illumination (full squares) of the structure (GNS1382) excited with P=4.5mW at $\lambda = 325nm$. 61
5.5 Effective photo current of the MSM structure measured at T=300K. . . . 62

6.1 Schematic drawing of a AlGaN/GaN based HEMT device. 64
6.2 Steps in the construction of the band diagram for a doped AlGaN and GaN heterojunction. 65

6.3 Band diagram of a AlGaN/GaN based HEMT device calculated with the 1D Poisson program for a temperature of 175K. 66
6.4 Sheet carrier concentration of the 2DEG and the residual carrier concentration of the AlGaN barrier as function of the Al mole fraction x for a temperature of 300K. 67
6.5 Sheet carrier concentration of the 2DEG and residual carrier concentration of the AlGaN barrier as a function of the AlGaN donor concentration for a temperature of 300K. 68
6.6 Sheet carrier concentration of the 2DEG and the residual carrier concentration of the AlGaN barrier as a function of the AlGaN barrier thickness for a temperature of 300K. 69
6.7 Photoluminescence spectra of different structures measured at T=2K. a) pure GaN-layer, b) $Al_{0.2}Ga_{0.8}N/GaN$ heterostructure, c) pure $Al_{0.2}Ga_{0.8}N$ layer. 70
6.8 Photoluminescence spectra of $Al_xGa_{1-x}N/GaN$ heterostructures with Al mole fractions of 0.25, 0.30 and 0.35 measured at T=2K. 72
6.9 Photoluminescence spectra of $Al_{0.35}Ga_{0.65}N/GaN$ heterostructures with different background doping concentrations of $N_D = 1{*}10^{17}cm^{-3}$ (GANS1384) (open circles) and $N_D = 1 * 10^{18}cm^{-3}$(GNP1429) (full circles) measured at T=2K. 72
6.10 Principle of the change in the band bending at the heterointerface due to the change in the c-GaN background doping 73
6.11 PL spectra of a $Al_{0.35}Ga_{0.65}N/GaN$ heterostructure (GANS1384) measured at different temperatures between 2K and 300K. 74
6.12 The peak position of the X, DAP1, DAP2 and the 2DEG correlated transition for temperatures between 2K and 300K for a $Al_{0.35}Ga_{0.65}N/GaN$ heterostructure (GANS1384). 75
6.13 The normalized PL intensity of the X, DAP and the 2DEG correlated transition for excitation power between $0.2Wcm^{-2}$ and $20Wcm^{-2}$ of a $Al_{0.35}Ga_{0.65}N/GaN$ heterostructure (GANS1384). 76
6.14 The peak position energy of the 2DEG related transition for excitation power between $0.2Wcm^{-2}$ and $20Wcm^{-2}$ for GANS1384 77
6.15 The peak position energy of the 2DEG related transition for applied voltages between -1.5V and +1.5V for GANS1228 78
6.16 Schematic drawing of the AlGaN/GaN heterostructure. 79
6.17 Current-Voltage characteristic of $Al_{0.35}Ga_{0.65}N/GaN$ heterostructures with different GaN cap layer thickness of 5nm (GANS1356)(triangles), 10nm (GANS1357)(squares) and 20nm (GANS1352)(circles). 80
6.18 Influence of the RMS roughness on the electrical behaviour of heterostructures with different cap layer thicknesses. 80
6.19 Capacity-Voltage characteristics of the $Al_{0.35}Ga_{0.65}N/GaN$ heterostructure (GANS1352) at temperatures of 300K, 175K and 150K. 81

6.20 Carrier concentration profile of the $Al_{0.35}Ga_{0.65}N/GaN$ heterostructure (GANS1352) at temperatures of 300K (circles), 175K (squares) and 150K (triangles). 82
6.21 Experimental (full circles) and simulated (dotted line) carrier concentration vs. the distance from the surface. The experimental data were calculated from a CV measurement done at 150 K. 83
6.22 Structure and photograph of the AlGaN/GaN heterostructure which is used for the Hall-effect analysis. 84
6.23 Electron concentration and mobility of a $Al_{0.35}Ga_{0.65}N$/GaN heterostructure for various temperatures between 10K and 300K. 85
6.24 Electron mobility limited by acoustic phonon scattering for various temperatures between 1K and 300K. 87
6.25 Electron mobility limited by impurity scattering for a temperature of T=10K. 88
6.26 Electron mobility limited by dislocation scattering for various carrier densities in the channel in the range of $N_{2D} = 10^{12}cm^{-2}$ to $N_{2D} = 10^{13}cm^{-2}$. 89
6.27 Electron mobility limited by roughness scattering for various carrier densities in the channel in the range of $N_{2D} = 10^{12}cm^{-2}$ to $N_{2D} = 10^{13}cm^{-2}$ 91
6.28 Electron mobility limited by different scattering mechanism for various carrier densities in the channel in the range of $N_{2D} = 10^{12}cm^{-2}$ to $N_{2D} = 10^{13}cm^{-2}$ and the comparison to experimental result 91
6.29 Arrangement of the source, drain and gate contact for our FET structures with a gate length of $6\mu m$ and a gate width of $100\mu m$ using Ref. [73]. . . 92
6.30 The different masks used for the fabrication of our FETs. a)Mesa structure b)Source and Drain contacts c)Gate contact. 93
6.31 a)A schematic sketch of the FET structure and the Mesa arrangement realized on GANS1416, b)An optical micrograph with the contacts and an enlargement of the gate region (GANS1416). 94
6.32 Source-gate I-V curve of FET structure B-1 realized on GANS1416 measured at a temperature of T=155K. 95
6.33 Source-drain I-V curve of FET structure B-1 realized on GANS1416 measured at a temperature of T=155K. 96
6.34 Current circuit used for the investigation of the field effect at our FET structure. 96
6.35 Source-drain I-V curve of FET structure B-1 for different gate voltages between -0.25V and +1V realized on GANS1416 measured at a temperature of T=155K. 97
6.36 Calculated banddiagrams of the FET structure for V_G=+0.5V and V_G=-0.25V. 97
6.37 Source-drain I-V curve of FET structure B-1 for different gate voltages between +0.25V and +1V without the influence of the buffer conductivity realized on GANS1416 measured at a temperature of T=155K. 98

List of abbrevations

2DEG	*Two-Dimensional Electrongas*
AFM	*Atomic Force Microscopy*
AlGaN	*cubic $Al_xGa_{1-x}N$*
BEP	*Beam Equivalent Pressure*
C-V	*Capacitance Voltage*
cw	*Continious Wave*
DAP	*Donor Acceptor Pair*
ECV	*Electrochemical Capacitance Voltage*
EL	*Electroluminescence*
FET	*Field Effect Transistor*
FWHM	*Full Width at Half Maximum*
GaN	*cubic GaN*
HEMT	*High Electron Mobility Transistor*
HFET	*Heterojunction Field Effect Transistor*
HRXRD	*High Resolution X-Ray Diffraction*
I-V	*Current Voltage*
MBE	*Molecular Beam Epitaxy*
MESA	*(span.) table, freestanding structures on one substrate*
MODFET	*Modulation Doped Field Effect Transistor*
MSM	*Metal-Semiconductor-Metal Structure*
PAMBE	*Plasma-assisted Molecular Beam Epitaxy*
PL	*Photoluminescence*
rf	*Radio Frequency*
RHEED	*Reflection High Energy Electron Diffraction*
RIE	*Reactive Ion Etching*
RSM	*Reciprocal Space Map*
SD	*Schottky Diode*
TFE	*Thermionic Field Emission*
TSB	*Thin Surface Barrier*
UHV	*Ultra High Vacuum*
UV	*Ultraviolet*
X	*Exciton*

List of symbols

a, b	deformation potentials	(eV)
a_0	lattice constant	$\mathring{A}$
A	contact area	cm^2
b	burgers vector	$\mathring{A}$
ϵ	relative dielectric permittivity	
ϵ_0	vacuum dielectric permittivity	
E	energy	(eV)
E_A	acceptor energy	(eV)
E_C	conduction band energy	(eV)
E_D	donor energy	(eV)
E_F	Fermi energy	(eV)
E_g	band gap energy	(eV)
E_V	valence band energy	(eV)
f	lattice mismatch	
F_{Al}	Al metal flux	$(cm^{-2}s^{-1})$
F_{Ga}	Ga metal flux	$(cm^{-2}s^{-1})$
h_c	critical thickness	(nm)
I	current	(mA)
J	current density	(Acm^{-2})
L	channel width	(nm)
μ	carrier mobility	$(cm^2(Vs)^{-1})$
m_e^*	effective electron mass	
m_h^*	effective hole mass	
n	free electron concentration	(cm^{-3})
N_A	acceptor concentration	(cm^{-3})
N_D	donor concentration	(cm^{-3})
N_C	conduction band density of states	(cm^{-3})
N_{2D}	2DEG concentration	(cm^{-2})
ρ	resistivity	(Ωcm)
R_H	Hall constant	$(cm^3(As)^{-1})$
ν	Poisson ratio	
V	voltage	(V)
T	temperature	(K)

Contents

1 Introduction **1**

2 Fundamentals **2**
2.1 Physical properties of cubic III-Nitrides 2
2.2 Growth and structuring techniques 5
2.2.1 Molecular beam epitaxy 5
2.2.2 Photolithography 6
2.3 Characterization techniques 6
2.3.1 X-ray Diffraction 6
2.3.2 Luminescence spectroscopy 8
2.3.3 Electrical measurements 10

3 Growth of GaN and AlGaN **16**
3.1 Growth of GaN 16
3.2 Growth of AlGaN 25
3.3 Electrical properties of GaN and AlGaN 30

4 GaN and AlGaN Schottky diodes **36**
4.1 Thermionic Emission Theory 36
4.2 Thin Surface Barrier Model 50
4.3 Breakdown Voltages of Schottky Diodes 55

5 Photoconductivity in GaN based Schottky diodes **58**

6 AlGaN/GaN based field effect transistors **63**
6.1 Structure and band diagram 63
6.2 Optical properties 70
6.3 Electrical properties 78
6.3.1 I-V and C-V analysis 79
6.3.2 Hall effect analysis 84
6.3.3 Theoretical description of carrier scattering 85
6.3.4 Fabrication and electrical characterization of HFET structures . . 92

7 Conclusion **99**

1 Introduction

A main point of modern research in physics is the reduction of dimensionality in optoelectronic and electronic devices, like quantum wells, quantum dots or high electron mobility transistors, which allow a more faster and efficient way of data transfer in electro optical communication systems.
AlGaN/GaN heterojunction field effect transistors (HFETs) are presently of outstanding interest for electronic devices, in particular, for high power and high frequency amplifiers. This is motivated by the potential commercial and military field application, namely, in the area of communication systems, radar, wireless stations, high temperature electronics and high power solid state switching [1][2]. The Group III-nitrides crystallize in the stable wurtzite structure or in the metastable zincblende structure. An important difference between these material modifications is the presence of strong internal electric fields in hexagonal (wurtzite) III-nitrides grown along the polar c-axis, while these build-in fields are absent in cubic (zincblende) III-nitrides. Since polarization fields can limit the performance of HEMTs some attention has been focused recently on the growth of wurtzite structures with nonpolar orientations e.g., growth along a, m or R directions [3][4][5] and also on cubic nitrides [6][7]. The cubic III-nitride polytype is metastable and can only be grown successfully in a narrow window of process conditions [[8] and references therein]. The realization of devices based on cubic nitrides has also been limited due to the difficulty to grow phase pure cubic nitrides with smooth interfaces, low defect density, high resistivity and the lack of appropriate substrates. The most promising candidate nowadays is 3C-SiC having a cubic crystal symmetry with a lattice mismatch between 0.7% (AlN) and 3.5% (GaN). This low lattice mismatch is connected with a high chemical inertness and a high thermal stability and conductivity. On the other hand due to the conductance of the substrates the devices show poor electrical characteristics.
The work will describe the growth and characterization of device structures based on cubic nitrides. They base on AlGaN/GaN layers grown by plasma-assisted molecular beam epitaxy on freestanding 3C-SiC (001). Chapter 3 will give an introduction in the optimization of the growth of GaN and AlGaN and the influence of the substrate quality and growth parameters on the crystal quality. In chapter 4 the properties of Schottky diodes, which will be used as gate contacts in field effect transistors, will be described. In chapter 5 some results about photoconductivity in our Schottky diodes, will be presented, which demonstrates the suitability of c-GaN for the realization of solarblind photodectors. Chapter 6 deals with the main issue of the thesis. Here the theory, the optical and electrical properties of AlGaN/GaN heterostructures will be described. At the end of chapter 6 the device operation of a AlGaN/GaN heterojunction field effect transistor structure will be demonstrated. All the results are summarized in chapter 7.

2 Fundamentals

2.1 Physical properties of cubic III-Nitrides

The basic issue of this work is the epitaxial growth of cubic AlN and GaN and their ternary alloys on freestanding 3C-SiC (001) and carbonized Si (001) substrates. This section will give an introduction in the physical properties of cubic group-III nitrides.

The crystallographic structure of the cubic group III-nitrides, which is drawn in Fig. 2.1

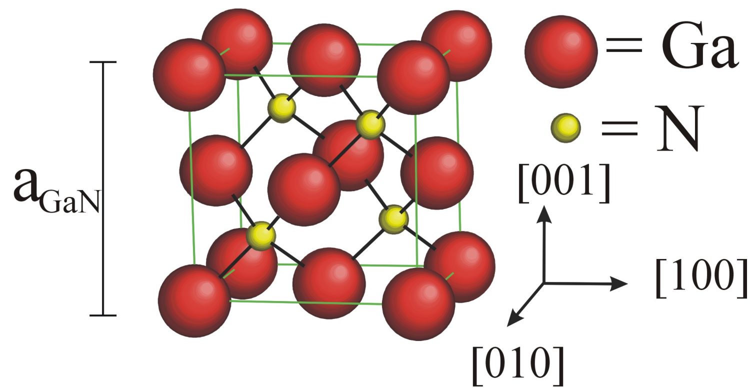

Figure 2.1: The zincblende structure of cubic GaN.

is based on a face centered unit cell with a base of two atoms. In case of stoichiometric growth conditions the metal is incorporated on the (0,0,0) lattice point, and the nitrogen is placed on the $(\frac{1}{4},\frac{1}{4},\frac{1}{4})$ lattice site. In the direction of the basic vectors the crystal consists of two altering layers which content only metal or nitrogen. The structure is very similar to that of diamond and the bond shows a strong covalent nature due to the comparable covalence radius of each element. This results in a high chemical inertness and thermodynamical stability. In addition a high isotropy of other parameters, like conductivity or refractive index is found. The table 2.1 gives a short overview of the physical properties of GaN and AlN. The parameter of the ternary alloys are calculated by the linear interpolation of the binary compounds.

Parameter	AlN	GaN	References
Lattice constant(Å)	4,38	4,52	[9][10]
Band gap(direct)(eV)	5,14	3,24	[11]
effective conduction band mass			
$(\frac{m_e}{m_0})$	0,19	0,15	[11]
effective hole mass			
$(\frac{m_{hh}}{m_0})$	1,20	0,80	[11]
$(\frac{m_{lh}}{m_0})$	0,33	0,18	[11]
Deformation potential (eV)			
a_c	-6,8	-2,77	[12][13]
b	-1,5	-2,67	[13][14]
Elastic coefficients (GPa)			
c_{11}	304	296	[13]
c_{12}	152	154	[13]

Table 2.1: Overview of the physical parameters of cubic AlN and GaN.

The paremeter, which are given in the table, are used for the calculation of the critical thickness as well as for the determination of the band diagram (see chapter 6) and for the modeling of the carrier mobility (also chapter 6).
During growth of different layers with different lattice constants one can distinguish three types of growth modes of the top layer. The schematic principle is shown in Fig. 2.2. In the case of a lattice matched top layer, the film is deposited on the substrate

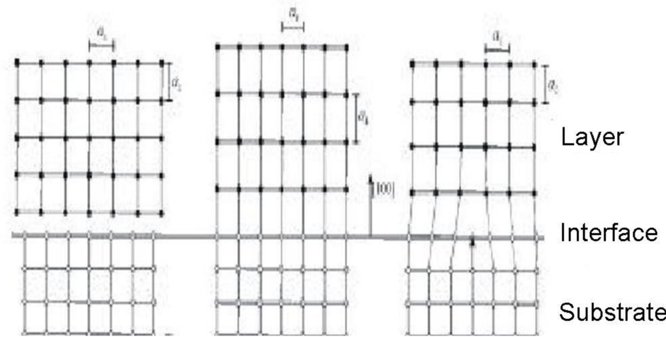

Figure 2.2: Heteroepitaxy: a) separated layers b)strained c)relaxed with incorporation of defects.

with out any changes in the unit cells. In the case of a layer with a lattice constant larger than that of the substrate, the in-plane lattice constant is reduced, whereas the constant in the growth direction is enlarged, due to the constant volume of the unit cell. If the layer has a smaller constant, the changes in the in-plane and perpendicular lattice constant are switched in comparision to the first case. The change in the lattice constants during heteroepitaxy creates energy which is stored as elastic energy in the crystal. On the other hand the total energy of the crystal can be minimized by the

incorporation of defectcs. For that at a certain thickness (critical thickness) it is better for the crystal to incorporate defects in order to minimize its energy. The value for the critical thickness can be calculated from the equality of the elastic and defect energy, which ends in an implicite equation for the critical thickness after Matthwes et al. [15].

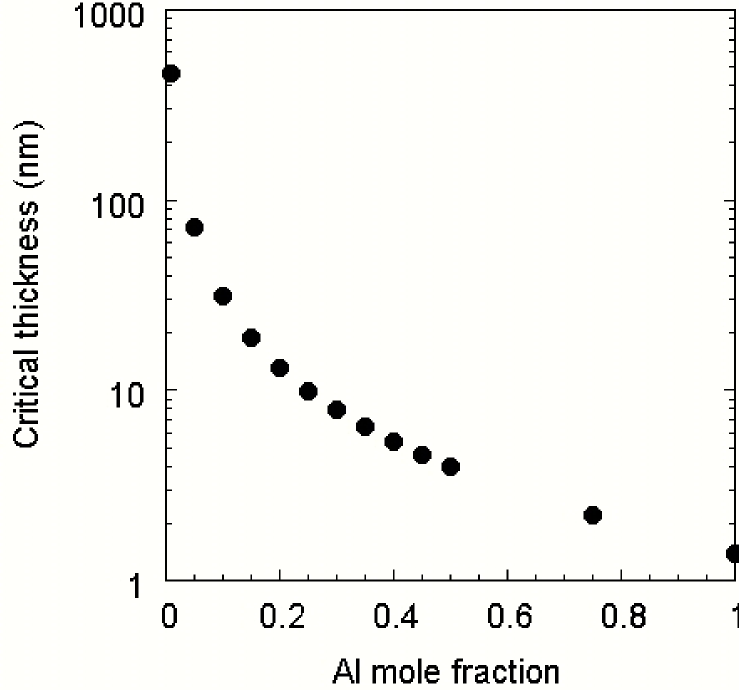

Figure 2.3: Critical thickness of $c - Al_xGa_{1-x}N$ on c-GaN as function of the Al mole fraction x on GaN.

$$h_c = \frac{b}{2\pi f} * \frac{(1 - \nu cos^2\alpha)}{(1+\nu)cos\lambda} * (ln\frac{h_c}{b} + 1) \tag{2.1}$$

in which b is the length of the Burgers vector, $\nu = \frac{c_{12}}{c_{12}+c_{11}}$ the Poisson ratio and $f = \frac{a_{layer} - a_{substrate}}{a_{layer}}$ the lattice mismatch. α and λ are the angles which describe the geometry of the defects. This equation is modified by Sherwin et al. [16] for a group-III nitride/ 3C-SiC system:

$$h_c = \frac{a_{layer}(1 - \nu/4)}{4\sqrt{2}\pi(1+\nu)f} * (ln\frac{\sqrt{2}h_c}{a_{substrate}} + 1) \tag{2.2}$$

This equation can be transferred to the cubic AlGaN/GaN system, if the following things are regarded:

$$h_c = \frac{a_{GaN}(1 - \nu/4)}{4\sqrt{2}\pi(1+\nu)f} * (ln\frac{\sqrt{2}h_c}{a_{GaN}} + 1) \tag{2.3}$$

$$\text{with} \quad f = \frac{a_{GaN} - a_{AlGaN}}{a_{GaN}}$$
$$\text{and} \quad \nu = \frac{c_{12}}{c_{12} + c_{11}}$$
$$\text{using} \quad c_{11} = x * c_{11,AlN} + (1 - x) * c_{11,GaN}$$
$$c_{12} = x * c_{12,AlN} + (1 - x) * c_{12,GaN}$$

in which f is the lattice mismatch between GaN and AlGaN and ν is the Poisson ratio derived from the elastic constants c_{11} and c_{12} of the AlGaN. With the variation of the Al mole fraction x, we can determine the critical thickness of AlGaN layers on GaN as function of x. The results of the calculation are plotted in Fig. 2.3. The plot illustrates the decrease of the critical thickness from ∞ for pure GaN to a value of 1.3nm for pure AlN on GaN.
The knowledge and the manipulation of the critical thickness has a direct influence on the strain status of epitaxial layers, which influences the defect density and the positions of the conduction and valence bands. Especially in low-dimensional device structures this changes can have a lot of effects on their performance, for example on the density of a two-dimensional electron gas (2DEG) in an AlGaN/GaN heterostructure.

2.2 Growth and structuring techniques

2.2.1 Molecular beam epitaxy

All the samples presented in this work are based on the epitaxial growth of thin semiconductor layer by Molecular Beam Epitaxy (MBE)[17]. MBE allows the growth of crystalline films on mono crystalline substrates, based on the evaporation of solid and liquid materials out of so called Knudsen-cells in ultra-high vacuum (UHV, p< $10^{-10} mbar$). Gases are dissociated with plasma sources or they are cracked on the substrate surface. Under these conditions a molecular beam, which can be interrupted by metallic shutters, hits the substrate and condensates on the surface. This method allows growth rates in the order of a few hundred nm/h. The quantity of the evaporated material can be controlled by the temperature of the source, because the atomic flux of a source is direct proportional to its temperature. The flux of the atoms is measured with an ionisation gauge (Bayard- Alpert). With the knowledge of the atomic fluxes of the different materials the composition of ternary compounds can be controlled by the temperatures of the cells. The control of the temperature of the source is done by a thermocouple, which is mounted below the bottom of the crucibile and connected with a temperature controller. In order to incorporate as less impurities as possible, high purity (99.9999%) source materials are used.
In this work a commercial Riber 32 MBE system is used. Details and a schematic draw can be found in Ref. [18]. The chamber is equipped with Knudsen cells for Al, Ga, In, and Si. For the Nitrogen a plasma source from Oxford Applied Research model HD25 was bought.

During growth a liquid nitrogen reduces the amount of impurities by one order of magnitude within the growth chamber .
The growth is monitored in situ by reflection of high energy electron diffraction (RHEED). This method uses a high energetically electron beam (10-20kV acceleration voltage), which hits the surface with an angle of $1° - 3°$. The electrons are diffracted at the atoms of the surface, after the reflection they can be monitored on a fluorescence screen. The RHEED pattern gives some information about the conditions on the surface. The main point during the growth of cubic group-III nitrides is the control of the stoichiometry. This can be checked by the change in the surface reconstructions from a c(2x2) to a (2x2), and the control of the intensity of the main streak [39].

2.2.2 Photolithography

Photolithography is the most used commercial technique to create lateral structures in semiconductor technology [20],[21],[22]. The principle of the photolithography bases on the transfer of lateral structures of a metal (NiCr) mask to the surface of a semiconductor.
In order to guarantee a perfect transfer the sample surface has to be cleaned from dust and organic contamination. Therefore the samples are rinsed in Aceton, Propanol and DI water for 5min. The surface oxide is removed using Buffer oxide etching (Ammonuim-fluoride, Flouride acid and DI water). Then the samples are rinsed in DI water and dried with nitrogen. After the cleaning procedure the surface is covered with an UV light sensitive photo resist(AR-P 3510). The resist has to be dried by thermal annealing for 30min at a temperature of 93°. After that the sample is put under the metal mask and exposed to UV light for 20s. Following by developing and fixing of the structure for 20s using a mix of developer:DI water=1:1. The exposed resist is removed by aceton and the structure is seen. Now the sample can be used for further steps, for example etching or evaporation of metal contacts or dielectric films.

2.3 Characterization techniques

2.3.1 X-ray Diffraction

Due to the use of a short wavelength, high resolution X-ray diffraction (HRXRD) is a very powerful technique for the investigation of structural properties on an atomic scale [23]. In this work, a Phillips XPert materials research diffractometer was used with a copper anode emitting the $K_{\alpha 1}$ radiation with a wavelength of $\lambda = 1.54 \AA$. The tube is equipped with a line focus and a hybrid monochromator, which guarantees a beam divergence of 47arcsec. The monochromator consists of a graded parabolic mirror in connection with a (220) channel cut Germanium crystal. The mirror parallelizes the beam and the Germanium crystal removes the $K_{\alpha 2}$ line. The samples are mounted onto a Euler cradle which allows the independent changes of angle of incidence ω, the

diffraction angle 2Θ, the rotation around the surface normal ϕ and the incident axis Ψ, as well as a linear motion in the three directions x, y, and z. The measurements were performed in double axis configuration using a $\frac{1}{16}^{\circ}$ slit in front of the detector resulting in a resolution of 1.8arcmin, as well as in the triple axis mode with a second (220) Germanium crystal in front of the detector with a resolution of 0.084arcmin. A schematic drawing of the diffractometer can be seen in Fig. 2.4. For a single crystal the

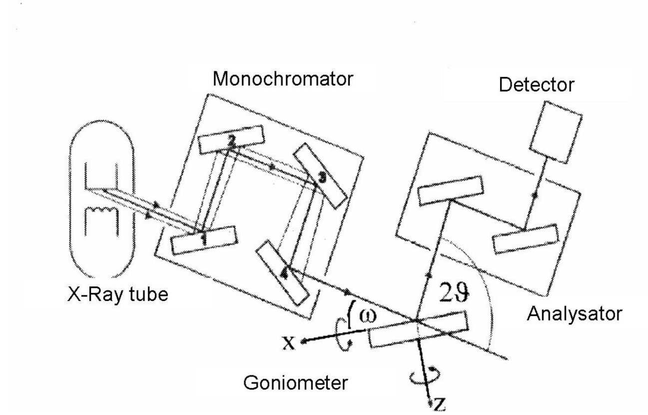

Figure 2.4: Schematic drawing of the materials research diffractometer system.

diffraction of X-Rays can be described by the Bragg condition:

$$\lambda = 2d_{hkl}sin(\Theta) \tag{2.4}$$

The triplet (hkl) denotes the Miller indices, and d_{hkl} the spacing of the lattice planes. For a cubic crystal symmetry and a given lattice constant a_0 the spacing d_{hkl} is given by

$$d_{hkl} = \frac{a_0}{\sqrt{h^2 + k^2 + l^2}} \tag{2.5}$$

Three different types of scans were performed to investigate the properties of the layers.

- $\omega - 2\Theta$-scan
  This kind of scan allows measurements where the angular rotation speed of the detector is twice as that of the incident angle. In case of scanning symmetrical lattice points, this is equal to reflection from lattice planes parallel to the sample surface. We get information with respect to vertically aligned properties, like the composition of ternary alloys.

- ω-scan
  The so called rocking curve is a scan with the detector angle in a fixed position,

while only the angle of incidence is changed. From the width of the reflex perpendicular to the surface the density of defects can be evaluated.

- Reciprocal Space Map (RSM)
  The combination of both types of scans gives a two-dimensional distribution of the intensity. In case of scanning around an asymmetric lattice point, information about the strain status of the layers are observed.

2.3.2 Luminescence spectroscopy

In general, luminescence refers to the emission of visible radiation. In the present context, this will also include the emission of near UV and IR light. The luminescence is caused by the radiative recombination of excess carriers. In common use, different types of luminescence are distinguished with respect to the kind of carrier excitation:

- Photoluminescence (PL)
  excitation of carriers by means of light irradiation
- Cathodoluminescence (CL)
  cathode rays (electrons) as a source of carrier excitation
- Electroluminescence (EL)
  carrier injection through an externally applied electric field

In general luminescence allows the observation of the optical properties [24],[25],[26]. In bulk semiconductors different kind of optical transitions are present. In films of high purity, i. e. intrinsic semiconductors band to band (e, h) and free exciton (X) transitions are typically dominating.
Band to band transitions are described by the difference of the conduction and the valence band edge:

$$E = \hbar\omega = E_C - E_V + \frac{\hbar^2 k^2}{2}(\frac{1}{m_e^*} + \frac{1}{m_h^*}) \tag{2.6}$$

in which E_C, E_V are the energy of the conduction and valence band, and m_e^*, m_h^* are the effective masses.
The excitons are formed through Coulomb interaction between an electron and a hole. The intensity and width of the excitonic transition gives a quick estimate of the relative sample quality. The physics of excitons is described by a model similar to the hydrogen atom:

$$E = \hbar\omega = E_C - E_V - \frac{13,6eV}{m_0\epsilon_s^2}(\frac{1}{m_e^*} + \frac{1}{m_h^*})^{-1} \tag{2.7}$$

in which ϵ represents the dielectric constant of the semiconductor.
In semiconductors with a high impurity concentration (defects or doping), these impurity levels offer a further possibility for radiative recombination. These levels, typically

separated from the conduction (valence) band by their ionization energy, are calculated in a similar way to the excitons:

$$E_D = \frac{13,6eV}{m_0 \epsilon_s^2} \frac{1}{m_e^*} \text{ and } E_A = \frac{13,6eV}{m_0 \epsilon_s^2} \frac{1}{m_h^*} \tag{2.8}$$

for the donor states E_D and analog for the acceptor states E_A. The total transition energy is then given by:

$$E = \hbar\omega = E_g - (E_D + E_A) + \frac{1}{2} k_B T \tag{2.9}$$

The factor $\frac{1}{2} k_B T$ bases on the thermal distribution of the carriers.
For an excact determination of the transition energy, the Coulomb interaction of the ionized donors and acceptors has to be taken into account. In that case equation 2.9 has to be extended by a term which describes the Coulomb interaction. The transition energy is then determined by the following relation [18]:

$$E = \hbar\omega = E_g - (E_D + E_A) + \frac{1}{2} k_B T + \frac{e^2}{4\pi\epsilon R} \tag{2.10}$$

The last term in the equation describes the Coulomb interaction of the donors and acceptors. In this term R is the distance of the impurities calculated with $R = \frac{1}{2} \frac{1}{\sqrt{N_I}}$, where N_I is the density of the impurities. Therefore from the transition energy the doping density can be estimated. In contradiction to the bulk materials, low dimensional layers show further transitions, but the nature and behaviour will be discussed later.
A schematic sketch of the PL system used in this work is given in Fig. 2.5. A cw

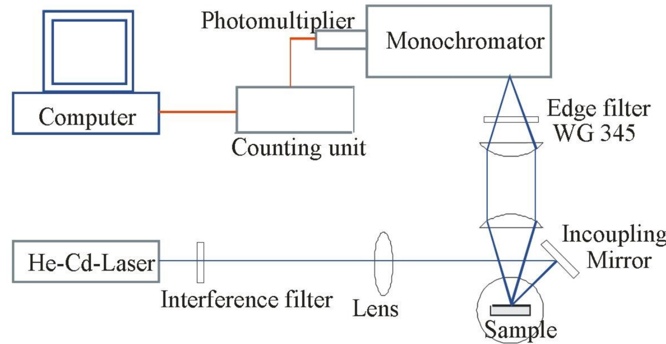

Figure 2.5: Schematic drawing of the Photoluminescence spectroscopy system.

HeCd laser from the company Kimmon is used as the coherent light source emitting a wavelength of $\lambda = 325nm \equiv 3.81eV$. The line is singled out from the plasma lines by a Fabry-Perot interference filter. The output power after the filter is about 5mW,

with the possibility to variate the power by four orders of magnitude by using neutral density filters. The light is then focussed onto a spot with a diameter of $100\mu m$, yielding a power density of $20W cm^{-2}$. The luminescent light is collected with an exit lens and dispersed in a Spex 270M monochromator by a 1200 line grating and 270mm focal length. The detection system consists of a photomultiplier tube and a photon counting system (Hamamatsu C3866 photocounting unit + Hewlett-Packard HP 53131A Universal counter), controlled by a personal computer (PC). The spectral resolution of the system is $\delta\lambda = 0.2nm \equiv 1.5meV$ at $\lambda = 400nm \equiv 3.1eV$.
The samples were mounted into a customer-designed liquid Helium bath-flow cryostat that allows measurements at temperatures between 2 and 350K. A Lake Shore 300 Auto tuning temperature controller with an AlGaAs temperature diode and a heating transistor are used to adjust the sample temperature during measurement. In addition the system is equipped with the possibility to apply an electric field on the mounted sample.

2.3.3 Electrical measurements

In the field of device research, electrical characterization is the most important technique for the investigation of device performance. A general introduction in the electric properties of semiconductor can be found in [27],[28]. Details of electrical measurements will be given in the chapters 4-6.
The most common analyzing methods are current-voltage characteristics (I-V), capacitance-

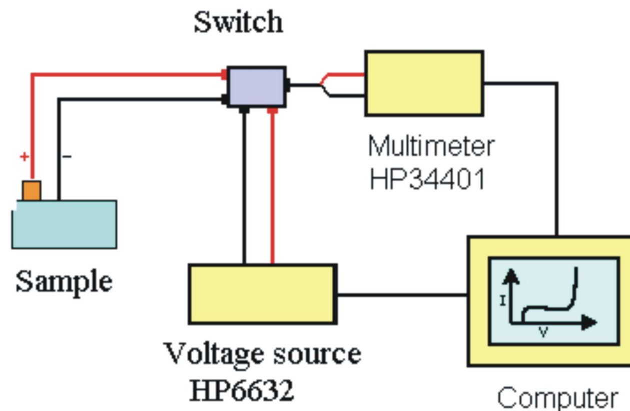

Figure 2.6: Schematic drawing of the I-V measurement setup.

voltage characteristics (C-V) and Hall-effect analysis. A detailed description of these methods can be found in [29].
The I-V measurements are done with a four tip prober from Süss Microtec. An optical microscope is used for positioning the probe onto the contact with a resolution less than $10\mu m$. The probes consist of tungstencarbide having a diameter of $7\mu m$. The Fig. 2.6 illustrates the arrangement and the principle of operation for the I-V setup.

A Hewlett-Packard HP6632 was used as voltage source applying an electric field in the range of -9V. . +9V. The current is measured with a multimeter model HP34401, also from Hewlett-Packard, for a current > 2mA, whereas for a current < 2mA a Keithley Picoamperemeter is connected to the current circuit. The applying of the voltage and the readout of the current is controlled by a PC using a self written Pascal program. The program allows the variation of the step width in the applied voltage, the time difference between applying the voltage and the readout of the current. A limiting of voltage and current is also avaiable. Voltages below -20V or above +20V are applied manually using an Electroautomatik EA 6056 voltage source.
A further method for the investigation of electrical properties is the C-V analysis. The method allows the determination of a carrier concentration profile vs. the depth by measuring the capacitance vs. voltage. A detailed description can be found in [35] and will also be discussed later.
For the determination of the CV characteristics a setup, which is described in Fig. 2.7, is used. The HP6632 is also used as the voltage source for CV measurements. The

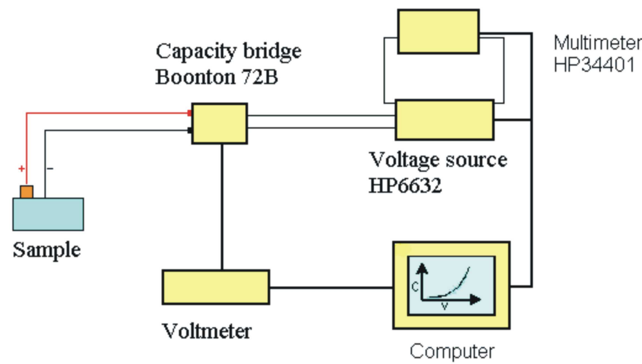

Figure 2.7: Schematic drawing of the C-V measurement setup.

capacitance is measured by a Boonton 72B capacitance bridge (1MHz, V_{AC}=100mV). The capacitance is put out as a DC voltage signal, which is proportional to the capacitance. From the voltage, the knowledge of the measurement range and the contact size, a Pascal based computer program is able to calculate the capacitance in units of pF.
A real diode normally consists of a superposition of a ideal diode and a resistance. If the resistance is small enough, it has to be take into account for the calculation of the capacity. Therefore a so-called Q-factor is defined as:

$$Q = \frac{R_L}{X_C} \tag{2.11}$$

with

$$X_C = \frac{1}{\omega C} \tag{2.12}$$

in which X_C is the capacitive reactance and R_L is the ohmic part of the resistance. For a measuring frequency of 1MHz, which is used for the Boonton 72B, and a capacitance of

100pF, X_C is equal to 10kΩ. With the known ohmic resistance the Q-factor is determined and the real capacity is calculated using the relation:

$$C_{real} = \frac{Q^2}{Q^2+1} C_{mess} \tag{2.13}$$

The system contains a phase-sensitive detector, which allows the precise measurement of capacitance down to a Q-factor of 1, if the leakage resistance is higher than the serial resistance, which is the case in all the samples.
Hall-effect measurements allow the determination of the carrier concentrations in semiconductors, as well as the carrier type. Additionally the mobility can be measured. Details are given in Ref. [29]. The Hall voltage U_H given by

$$U_H = -\frac{1}{ne}\frac{IB}{d} \tag{2.14}$$

where n carriers of charge e flow with an external current I under the influence of

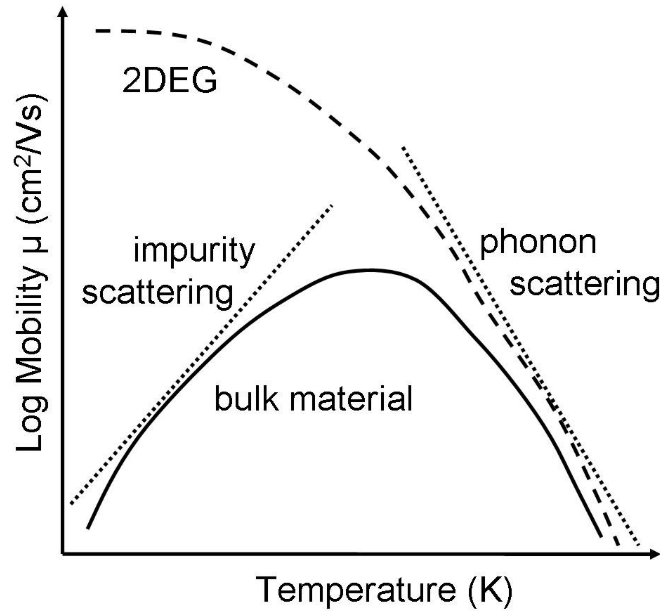

Figure 2.8: Schematic drawing of the temperature dependence of carrier mobility for bulk material (solid line) and a two-dimensional electron gas (2DEG) (dashed line).

a magnetic field B through a semiconductor layer of thickness d. Defining the Hall constant R_H the equation can be written as:

$$R_H = \frac{U_H d}{IB} \tag{2.15}$$

Conventionally a negative sign of R_H means n-type and a positive sign means p-type conductivity. For the measurements a magnetic field of 0.8T is used. For the determination of the carrier mobility μ, the knowledge of the resistivity of the film is essential. The resistivity ρ is calculated by:

$$\rho = \frac{\pi d}{2ln2}\frac{U}{I}f \tag{2.16}$$

in which the formfactor f describes the ratio of the resistance parallel to the edges of the sample. Then the mobility μ is given by:

$$\mu = \frac{R_H}{\rho} \tag{2.17}$$

From the variation of the mobility with temperature, one can distinguish between electrons in the bulk and electrons located in the channel of a heterojunction field effect transistor (HFET) structure. Figure 2.8 depicts the differences in a semilogarithimic scale. For a carrier with a mobility in three dimensions μ shows an increasing value with increasing temperature up to 100K due to the reduction of ionized impurity scattering. After reaching a maximum at T=100K, the values decreases with increasing temperature, because of the influence of phonon scattering, which is the dominant mechanism for temperature above 100K. In the case of a spatial separation of carriers and their ionized impurities a different temperature dependence is observed. At lower temperatures there is no freeze out of carriers at the impurities and impurity scattering do not occur due to the spatial separation. This results in a further increase of the carrier mobility with deceasing temperature.

For that reason and in addition also for the investigation of temperature dependent measurement of the IV and CV curves, the samples are mounted in Cryovac flow cryostat model 3-06-4251C. The system allows a temperature variation in the range from 5K to 350K, controlled by cryovac temperature controller model MK4, equipped with two AlGaAs temperature diodes, one directly mounted on the sample holder, the other in the cryostat.

The four-point probe technique is one of the most common methods for measuring the semiconductor resistivity [30].Two probes carry the current and the other two probes are used for voltage sensing. A schematic drawing of the contact arrangement and the way of current flow is given in Fig. 2.9. The probes are generally arranged in-line with equal probe spacing. The use of four probes has an important advantage over two probes. Although the two current-carrying probes still have contact and spreading resistance associated with them, that is not true for the two voltage probes because the voltage is measured either with a potentiometer which draws no current at all or with a high impedance voltmeter which draws very little current. The contact resistance and the spreading resistance are negligible in either case because the voltage drops across them are negligibly small due to the very small current that flows through them. Under the assumption of a infinite sample and that the current I flows between contact 1 and 4 the electric field $E_1(r)$ around contact 1 in a distance r is given by:

$$E_1(r) = \rho \cdot j(r) = \rho \cdot \frac{2I}{4\pi r^2} \tag{2.18}$$

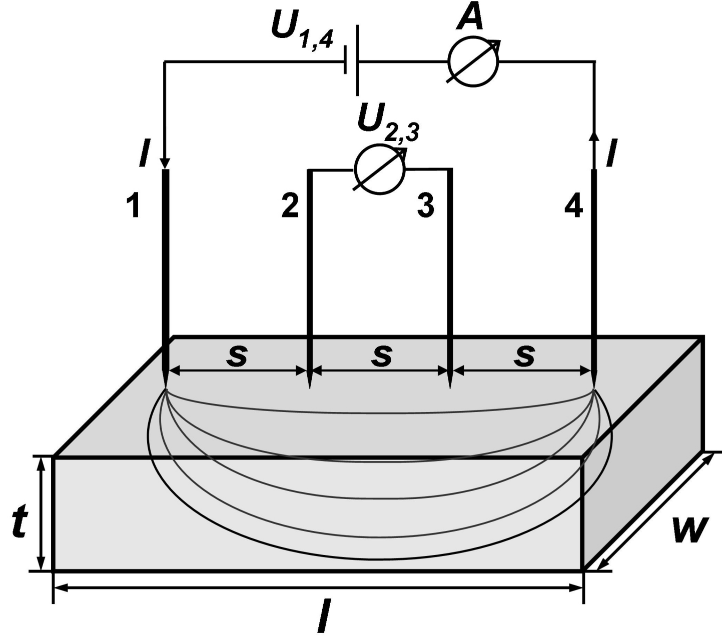

Figure 2.9: Schematic drawing of the contact arrangement and the current flow during a four-point probe measurement.

in which j is the current density and ρ the resistivity. If the probes are arranged in the same distance s, the potential ϕ_1, which is generated by the contact 1 between probe 2 and 3, is equal to:

$$\phi_1 = \int_{2s}^{s} E_1 dr = \rho \cdot \frac{I}{4\pi s} \tag{2.19}$$

On the other hand, the contact 4 generates also a electric potential between probe 2 and 3. The potentials ϕ_1 and ϕ_2 are equal. Therefore the voltage $U_{2,3}$ between probe 2 and 3 is given by the sum of both:

$$U_{2,3} = \phi_1 + \phi_2 = \rho \cdot \frac{I}{2\pi s} \tag{2.20}$$

So the resistivity ρ of an infinite sample is equal to:

$$\rho = 2\pi s \cdot \frac{U_{2,3}}{I} \tag{2.21}$$

For real samples with a finite lateral extension and a finite thickness equation 2. has to be modified. Therefore three correction factors F_1,F_2 and F_3 have to be take into account. The factor F_1 considers the finite thickness t [32]. If $t < \frac{s}{2}$ the factor is given by:

$$F_1 = \frac{t/s}{2\ln(2)} \tag{2.22}$$

The finite lateral extension of the samples is compensated by the factor F_2. In case of radial symmetric samples with a diameter d the correction factor is calculated by [?] [33]

$$F_2 = \frac{\ln(2)}{\ln(2) + \ln\{[(d/s)^2 + 3]/[(d/s)^2 - 3]\}} \tag{2.23}$$

The position of the probes in relation to the edges of the sample influences also the determination of the resistivity. This is take into account by the factor F_3 [34]. If the contacts are located at the distance l_1 perpendicular to one edge, F_{31} is given by

$$F_{31} = \frac{1}{1 + \frac{1}{1+2l_1/s} - \frac{1}{2+2l_1/s} - \frac{1}{4+2l_1/s} + \frac{1}{5+2l_1/s}} \tag{2.24}$$

For the second edge of the sample with a parallel arrangement we have to consider a second correction:

$$F_{32} = \frac{1}{1 + \frac{2}{\sqrt{1+(2l_2/s)^2}} - \frac{1}{\sqrt{1+(l_2/s)^2}}} \tag{2.25}$$

Both factors have to be used two times, because the contacts are arranged perpendicular and parallel to two edges. Therefore the resistivity is given by:

$$\rho = F_1 F_2 F_{31}^2 F_{32}^2 \cdot 2\pi s \frac{U_{2,3}}{I} \tag{2.26}$$

3 Growth of GaN and AlGaN

3.1 Growth of GaN

The growth of phase-pure cubic GaN with a low defect density ($< 10^9 cm^{-2}$) and a smooth surface is the basic feature for the realization of high quality electronic devices. The optimum conditions for the epitaxial growth of c-GaN are mainly determined by two parameters, the surface stoichiometry and the substrate temperature [8]. Both parameters are interrelated; therefore an in-situ control of both substrate temperature and surface stoichiometry is highly desirable. This has been achieved by monitoring the MBE growth process by RHEED. The study of the surface reconstruction behaviour was one of the key issues in understanding the c-III nitride growth. First principle calculations by Neugebauer et. al. [36] showed that all energetically favored surface modifications of the nonpolar (001) c-GaN surface are Ga-stabilized and therefore optimum growth conditions were expected under slightly Ga-rich conditions.

The c-GaN films, which are schematically drawn in Fig. 3.1 are grown on freestanding

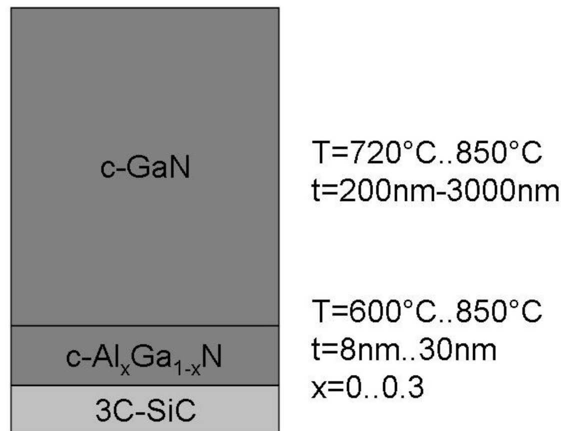

Figure 3.1: Schematic drawing of the structure of the investigated c-GaN layers.

3C-SiC (001) substrates backcoated with silicon for efficient radiative heating. Prior to growth, the substrates are subjected to an Al deoxidation process at $T_{Subs} = 800°C$ using an Al beam equivalent pressure of $8.2 * 10^{-8}$mbar [37] in order to remove native oxide.

Then an $Al_xGa_{1-x}N$ buffer is deposited, having an Al mole fraction between x=0 and x=1 and a thickness ranging from 8nm to 30nm. The temperature for the deposition of the buffer varies from $T_{Buffer} = 600°C$ to $T_{Buffer} = 850°C$. Following this step, a 200nm-3000nm thick GaN layer is grown at temperatures ranging from $T_{Subs} = 720°C$ to $T_{Subs} = 850°C$. During the growth of all these films, the nitrogen plasma conditions were kept constant at 260W rf power and 0.4sccm nitrogen flow equal to an active nitrogen flux of $F_N = 2.2 * 10^{14} cm^{-2}s^{-1}$. The growth was continously monitored in situ by RHEED at 16kV energy and an incidence angle of 1.3°. The intensity of the main streak and other regions of interest along the [-110] azimuth of c-GaN (001) are recorded using a digital RHEED analysis system. The arrival rate of the group-III atoms was determined by measuring the beam equivalent pressures (BEP) prior to growth, using a nude ionization gauge placed at the substrate position. The impinging flux F_i^{imp} of the i species (in $cm^{-2}s^{-1}$), is given by [38]:

$$F_i^{imp} = C_i \frac{P_i}{\sqrt{m_i k_B T_i}} \tag{3.1}$$

where P_i is the measured BEP, m_i is the atomic mass, and T_i is the vapor temperature,

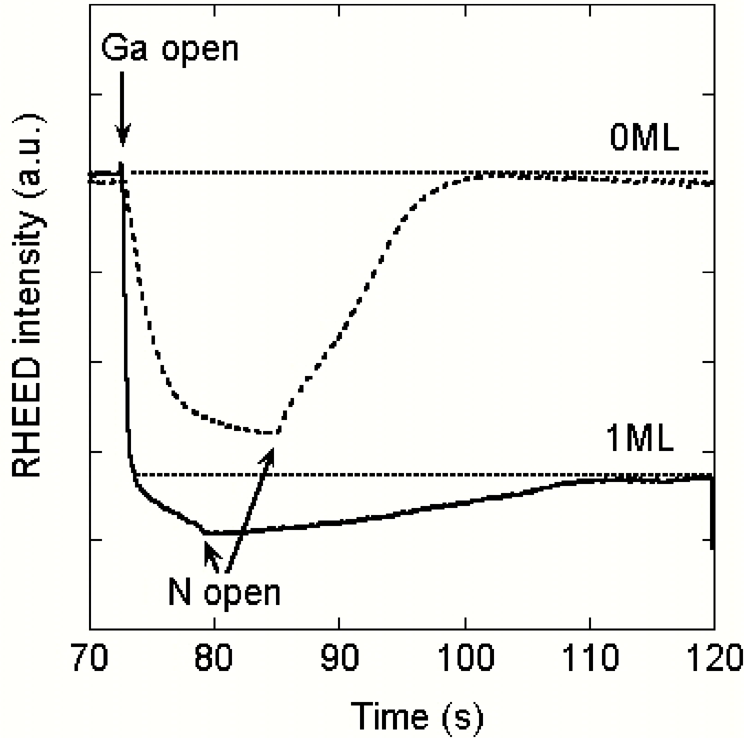

Figure 3.2: Measured RHEED intensity during the initial growth of c-GaN. The RHEED intensity after opening the N shutter yields the amount of excess Ga on the c-GaN surface.

which is taken to be approximately equal to the corresponding effusion cell absolute

temperature. The constant C_i reflects the ionization gauge sensitivity factors for gallium as well as geometrical factors related to placing the ion gauge in the exact position of the substrate.
The Ga coverage of c-GaN was obtained by measuring the intensity of the reflected electron beam ((0,0)-streak RHEED intensity) [39]. During growth interruption the adsorption and desorption of gallium on a c-GaN (001) surface was measured employing the intensity of a reflected high energy electron beam (RHEED intensity) as a probe. After opening the Ga shutter we observed a decrease of the RHEED intensity to a saturation value, which was related to the impinging Ga flux. Using the known value of the Ga-flux and the transient time of the RHEED intensity we were able to estimate the amount of adsorbed gallium. After closing the Ga shutter the RHEED intensity reached the starting value indicating a total desorption of excess Ga. A similar procedure was used to measure the Ga coverage during c-GaN growth. Figure 3.2 shows the RHEED intensity measured after opening the N shutter with the Ga flux on. From the decrease of the RHEED intensity after the nitrogen shutter was opened we were able to measure the Ga-coverage during growth with an accuracy of 0.1ML. The stoichiometric growth of c-GaN without Ga coverage was realized, if after opening the N shutter no drop in the RHEED intensity (dotted line) was observed, whereas c-GaN growth with 1ML coverage was defined by a certain drop in the intensity (solid line). The total impinging Ga flux for the growth of GaN is given by:

$$F_{Ga,1ML}^{imp}(GaN) = F_{Ga,0ML}^{imp}(GaN) + F_{Ga}^{1ML,cov} = \frac{F_{Ga}^{inc}(GaN)}{s_{Ga}} + F_{Ga}^{1ML,cov}(GaN) \quad (3.2)$$

where $F_{Ga,1ML}^{imp}$ was the impinging Ga flux for Ga growth with 1ML coverage, $F_{Ga,0ML}^{imp}$ was the corresponding flux for stoichiometric growth, $F_{Ga}^{1ML,cov}$ was the Ga flux necessary for the coverage of 1 ML, and F_{Ga}^{inc} was the incorporated Ga flux and s_{Ga} the sticking coefficient, respectively. The difference in the Ga flux necessary for 1ML coverage and 0ML coverage is about 25% of $F_{Ga,1ML}^{imp}$. This recipe is used as the standard process for the growth of the samples which a described in this work.
The RHEED is also used to determine the properties of the GaN surface during growth, i. e. the terrace width. This parameter will have a strong influence on the mobility of carriers in a 2DEG. Therefore we measure RHEED linescans parallel to the shadow edge. From Lent at al. [40] it was known that the lineshape of these scans can be approximated by a Voigt function. A Voigt function is the superposition of a Gauss and a Lorentz function. And from the theory the terrace width Λ is given by:

$$\Lambda = C * \frac{\pi}{FWHM_{Gauss}} \quad (3.3)$$

Fig. 3.3 depicts the result of this calculation. For a GaN film grown at $720°C$ a constant terrace width of about 3.5nm is observed for GaN for thicknesses up to 480nm. The most important parameters for the investigation of the quality of the c-GaN are the dislocation density, given by the FWHM of the X-ray rocking curve [18], the phase purity and the surface roughness. These parameters influence the device performance of

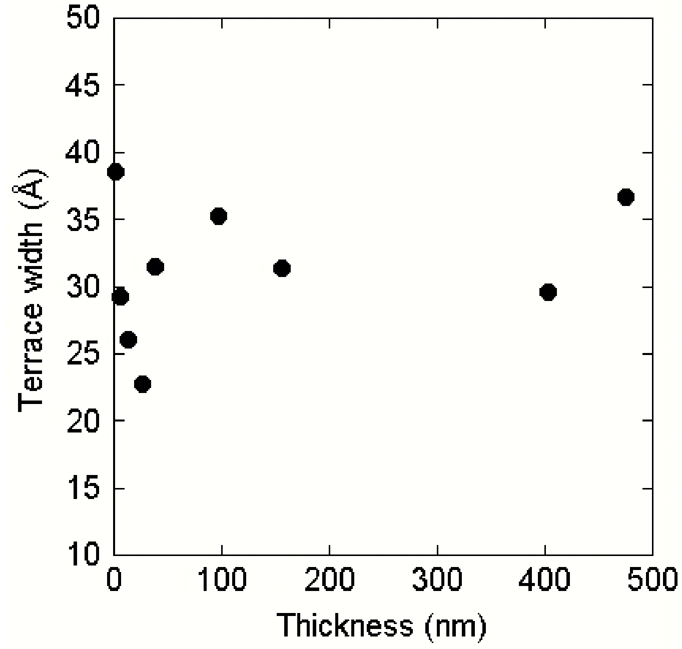

Figure 3.3: Terrace width of a c-GaN film.

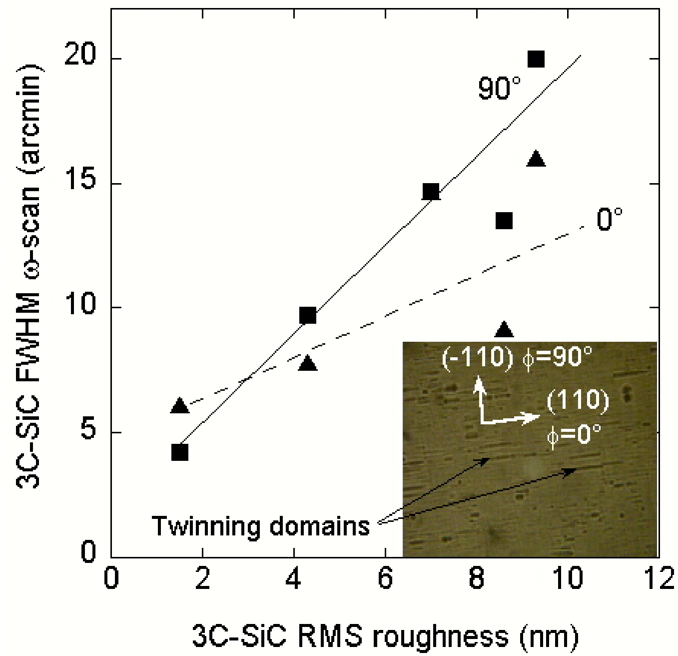

Figure 3.4: RMS roughness on a $5x5\mu m^2$ scan range as function of the FWHM of the X-ray rocking curve for $\phi = 0°$ (triangles) and $\phi = 90°$ (squares) of the freestanding 3C-SiC substrates.

c-AlGaN/GaN based FETs by scattering of carriers and therefore reducing mobility. In order to check how these paramters can be influenced by the substrate quality or by the growth process, the structural properties of the substrate as well as that of the GaN growth process were studied.
The 3C-SiC substrate can influence the quality of the c-GaN buffer in two ways, first by the amount of dislocation density generated and second by the surface RMS roughness. Therefore we determine the FWHM of the rocking curve and the RMS roughness on a $5x5\mu m^2$ scan range of our substrate and check their dependency on each other. The Fig. 3.4 depicts the results of these measurements. The FWHM of the rocking curve is plotted as function of the RMS roughness FWHM for a substrate angle of $\phi = 0°$ (triangles) and $\phi = 90°$ (square). The angle ϕ represents the angle between the incident X-ray beam and the (110) direction of the crystal. The dashed and the solid line are a guide for the eye. An increase of the FWHM with increasing RMS roughness is observed for both substrate orientation angles. At a half width of the rocking curve of 5arcmin, the RMS roughness is typically in the order of 1.5nm, whereas with an increase of the width up to 20arcmin the roughness is approximately 10nm. The increase in roughness with increasing dislocation density is caused by the fact that the typical defects in 3C-SiC are so called twinning domains [41]. These twinning domains originate from

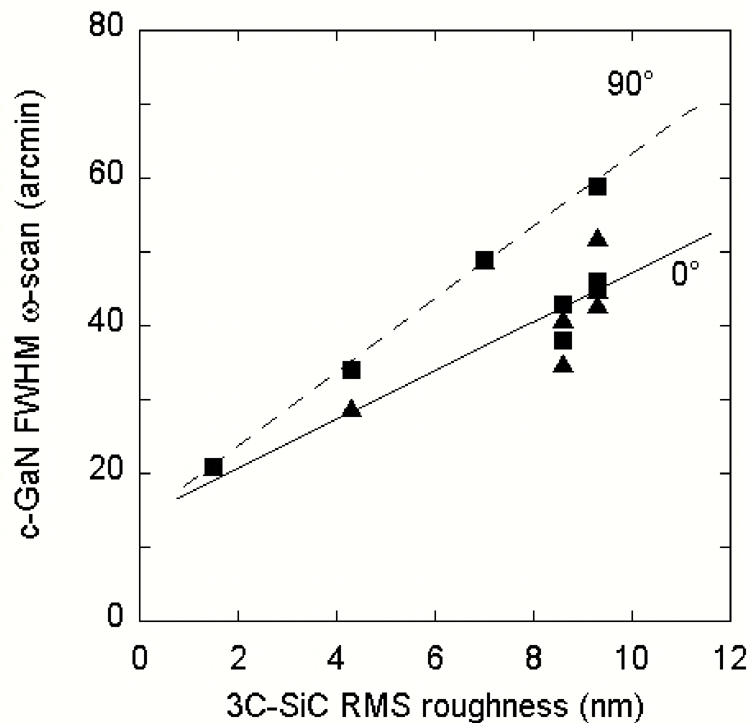

Figure 3.5: The FWHM of the X-ray rocking curve of c-GaN as function of the SiC RMS roughness on a $5x5\mu m^2$ scan range for $\phi = 0°$ (triangles) and $\phi = 90°$ (squares).

the growth process of the SiC and the incorporation of stacking faults [42]. These do-

mains causes then a groove in the substrate surface, such that the measured roughness increases with increasing groove number. The dependence between the defect density and the roughness allows one to investigate the properties of GaN only as function of surface roughness.
Figure Fig. 3.5 shows the influence of the substrate roughness on the structural prop-

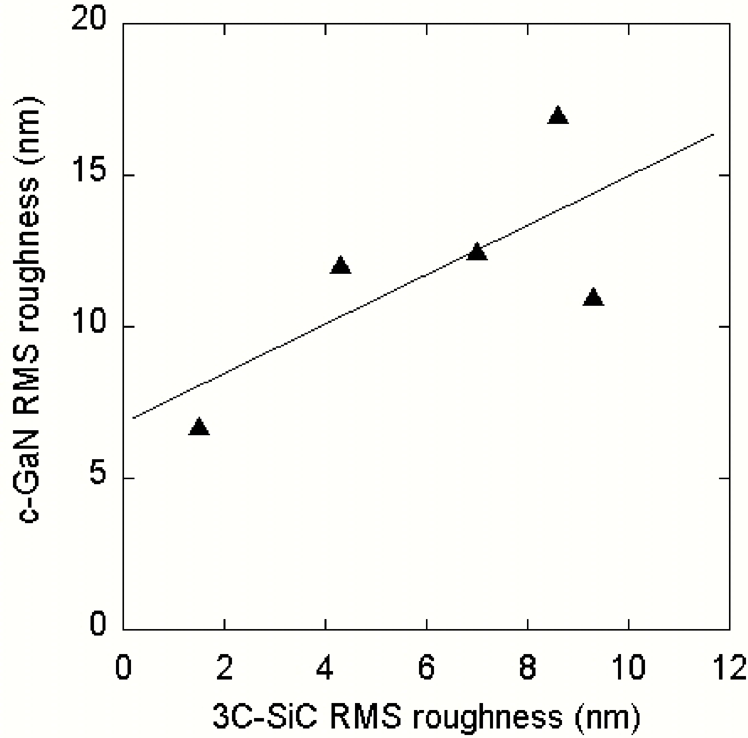

Figure 3.6: The RMS roughness of c-GaN as function of the SiC RMS roughness on a $5x5\mu m^2$ scan range.

erties of cubic GaN. The rocking curve half width of the c-GaN with a thickness of t=600nm is plotted as function of the substrate roughness. The measurements of the rocking curve are performed in the substrate orientation of $\phi = 0°$ (triangles) and $\phi = 90°$ (squares). For both orientation an increase of the GaN half width with increasing roughness of the substrate is observed. The increase originates from the increasing number of twinning domains, which causes several grooves in the substrate surface. During the initial growth of the GaN buffer, these grooves act as nucleus for the incorporation of threading dislocations in the GaN. Thus with increasing number of grooves the defect density of the c-GaN increases.
A further parameter, which has to be investigated, is the influence of the substrate roughness on the roughness of the GaN film. The results are depicted in Fig. 3.6. The plot shows the RMS roughness of 600nm thick c-GaN films on a $5x5\mu m^2$ scan range versus the RMS of the 3C-SiC substrate. An increase of the GaN roughness with increasing substrate RMS is revealed. The values range from 6.7nm for the GaN on a 1.5nm rough

SiC substrate to 17nm for GaN on SiC with a RMS of 8.6nm. The solid line is a guide for the eye. from this observed dependence, it can be surmise, that grooves present in the SiC surface transferred to the GaN layer, thereby, contributing to surface roughness as well. The standard values for the delivered substrates are 3.5arcmin for the rocking curve half width and a RMS roughness of 1nm, which gives the best results for the growth of GaN.

Following the investigation of the substrate properties the influence of the GaN growth

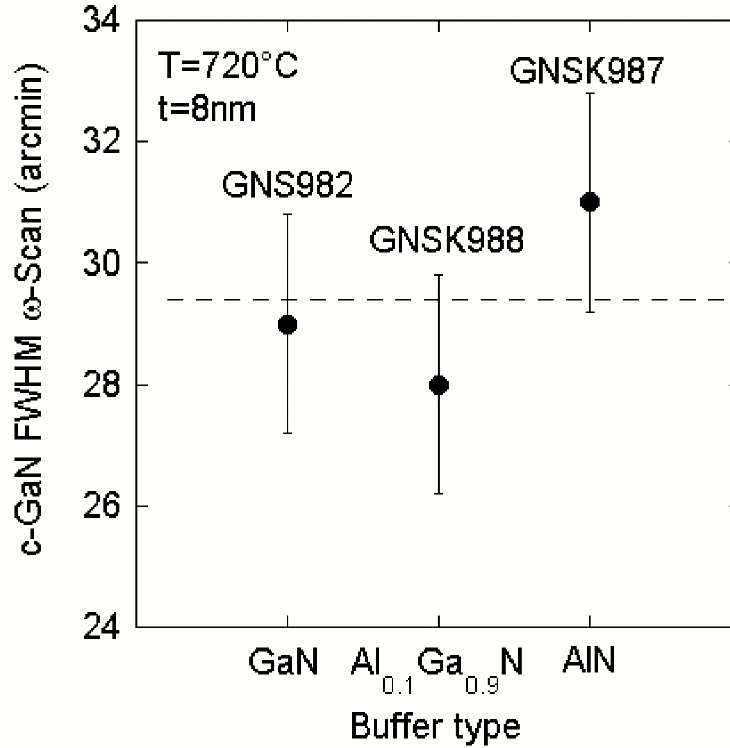

Figure 3.7: The FWHM of the X-ray rocking curve of c-GaN as function of the buffer type.

process itself on the structural properties of GaN is studied. The initial point of this investigation is to study the influence of the buffer type on the quality of the GaN. Therefore a series of 600nm thick GaN films was grown at $T_{Subs} = 720°C$ on top of a GaN, $Al_{0.1}Ga_{0.9}N$ and AlN buffer with a thickness of 8nm and at $T_{Subs} = 720°C$. The results of these experiments are shown in Fig. 3.7 and 3.8. Figure 3.7 depicts the influence of the buffer type on the rocking curve half width of our GaN layers. The FWHM is nearly constant at a value of 29arcmin, and therefore independent on the buffer type. This effect is caused by lattice mismatch between the different epitaxial layers. In case of a GaN buffer the buffer relaxes after a few nm due to the lattice mismatch between the SiC and GaN. The mismatch causes then the incorporation of dislocations. For a $Al_{0.1}Ga_{0.9}N$ buffer the situation is not that different to the GaN buffer, because of the low Al content. Therefore the relaxation process is the same and the incorporation of

dislocations also. If we look to the AlN buffer, it was found that this buffer is strained on the SiC, due to the small lattice mismatch of 0.7%. But if we continue the growth of GaN, the layer relaxes on the AlN, due to the mismatch of AlN to GaN, which is comparable to that of SiC to GaN. In the end, the relaxation process is shifted from the SiC/GaN interface to the AlN/GaN interface.

As described previously, the roughness and the phase purity of the GaN are also im-

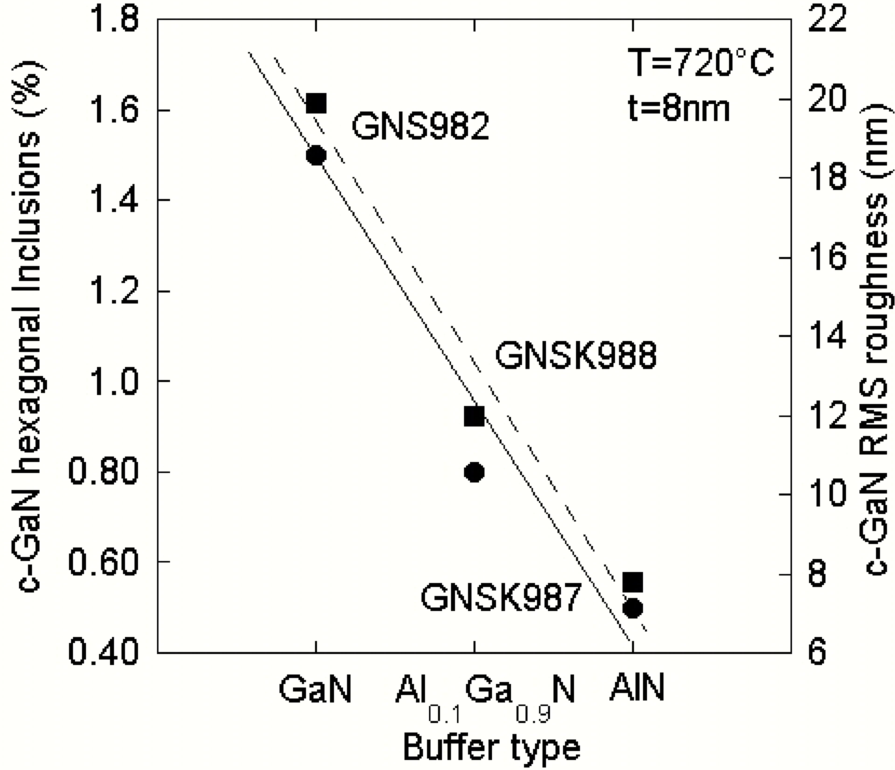

Figure 3.8: The RMS roughness (circles) and the amount of hexagonal phase inclusion (squares) of c-GaN as function of the buffer type.

portant for device performance. Figure 3.8 shows the values for the phase purity and roughness for the different buffer types. We observe a clear reduction of the GaN roughness (circles) with increasing amount of Al in the buffer layer. For the GaN a RMS roughness of 19.9nm was measured on a $5x5\mu m^2$ scan range and for the AlN buffer a value of 7.8nm. The result indicates, that the Al may act as a surfactant. The amount of hexagonal inclusions (squares)are also plotted in the figure, they decrease from 1.5% for the GaN buffer to 0.5% for the AlN buffer. If both dependences are compared, one can see, that the roughness of the buffer may influence the amount of hexagonal inclusions in the layer. A higher roughness (or differences in height) forces the formation of (111) planes in the cubic phase, which then act as a nucleus for the hexagonal (001) planes. On these (111) planes the growth of h-GaN is favoured, due to its higher thermodynamic stability and growth rate.

The second point of discussion is the influence of the growth temperature on the struc-

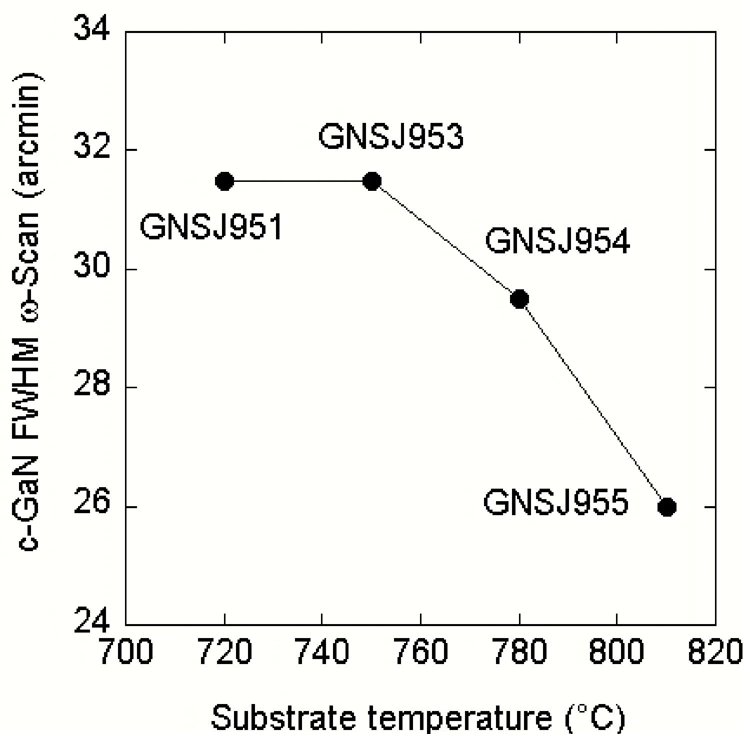

Figure 3.9: The FWHM of the X-ray rocking curve of c-GaN as function of substrate temperature.

tural properties of c-GaN. Figure 3.9 shows the rocking curve half width of 600nm thick c-GaN films grown on a GaN buffer as function of growth temperature in the range from $T_{Subs} = 720°C$ to $T_{Subs} = 810°C$. In this range a decrease of the half width from 31arcmin to 26arcmin by increasing the substrate temperature from $T_{Subs} = 720°C$ to $T_{Subs} = 810°C$ is observed. The decrease of the FWHM of the GaN is caused by the higher surface mobility of the Ga and N atoms on the surface at higher temperatures. The higher mobility of the atoms allows a more perfect arrangement in the crystal lattice. Therefore we have less dislocation in the crystal and the width of the rocking curve decreases.

In Fig. 3.10 the results for the influence of the temperature on the roughness and on the phase purity is depicted. The data reveal an increase of the roughness (circles) from 12nm on a $5x5\mu m^2$ scan range for $T_{Subs} = 720°C$ to 22nm for $T_{Subs} = 810°C$. The increase of the roughness originates from the same reason like the decrease of FWHM. The higher mobility at higher growth temperatures causes the formation of structures on the surface, which are mainly confined by (111) planes. As mentioned above, these planes are also responsible for the formation of hexagonal inclusions and a look on the phase purity (squares) shows an increase of hexagonal phase with increasing temperature. The data show 0.5% for a temperature of $T_{Subs} = 720°C$ and 4.3% for $T_{Subs} = 750°C$. This

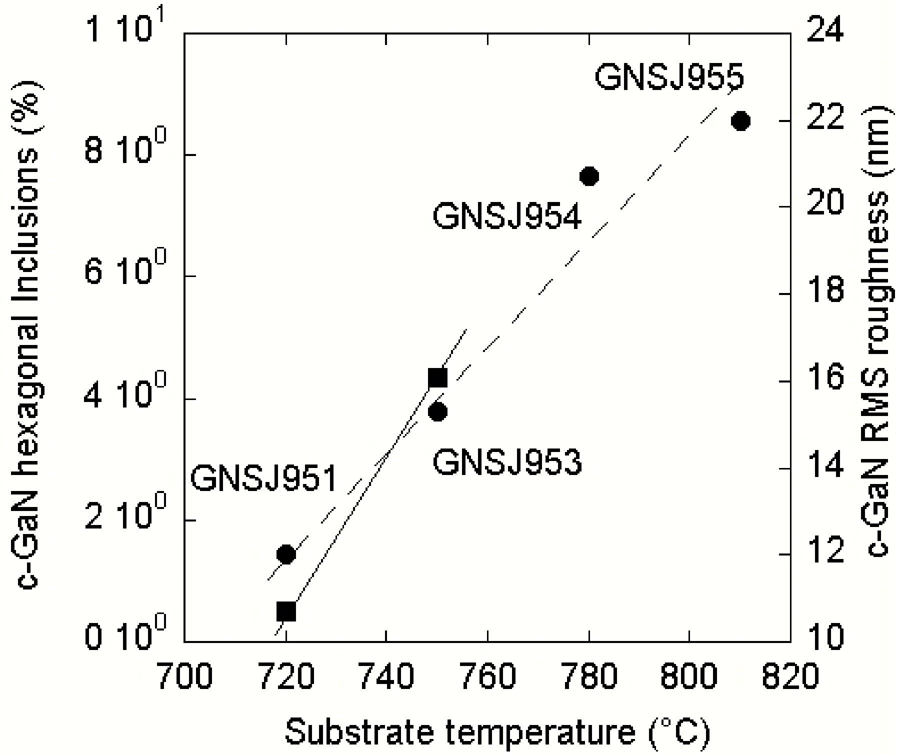

Figure 3.10: The RMS roughness (circles) and the amount of hexagonal phase inclusion (squares) of c-GaN as function of the substrate temperature.

is a further hint for a correlation between surface roughness and phase purity.
In summary a GaN buffer grown at $T_{Subs} = 720°C$ was choosen together with the deposition of the GaN bulk also at $T_{Subs} = 720°C$. This set of parameter is a good compromise between disclocation density, surface roughness and phase purity and is used for all further experiments.

3.2 Growth of AlGaN

On top of the GaN cubic $Al_xGa_{1-x}N$ films, about 50nm to 600nm thick, are grown at a temperature of $T_{Subs} = 720°C$. Two series of $Al_xGa_{1-x}N$ epilayers were realized, one with a coverage of 1 monolayer (ML) Ga on the growing surface, a second one having a Ga coverage >>1ML. After the determination of the fluxes $F_{Ga,0ML}^{imp}$ and $F_{Ga}^{1ML,cov}$ by the experiment described above (see chapter 3.1), the impinging Al and Ga fluxes for the growth of a $c-Al_xGa_{1-x}N$ alloy with 1 ML coverage were easily adjusted using the

relations:

$$F_{Al}^{imp}(AlGaN) = \frac{xF_{Ga}^{inc}(GaN)}{s_{Al}} \qquad \text{and} \tag{3.4}$$

$$F_{Ga,1ML}^{imp}(AlGaN) = \frac{(1-x)F_{Ga}^{inc}(GaN)}{s_{Ga}} + F_{Ga}^{1ML,cov} \tag{3.5}$$

In the next step the procedure was transferred to the growth of $c-Al_xGa_{1-x}N$ films. Figure 3.11 shows the variation in the RHEED intensity during the initial growth of a

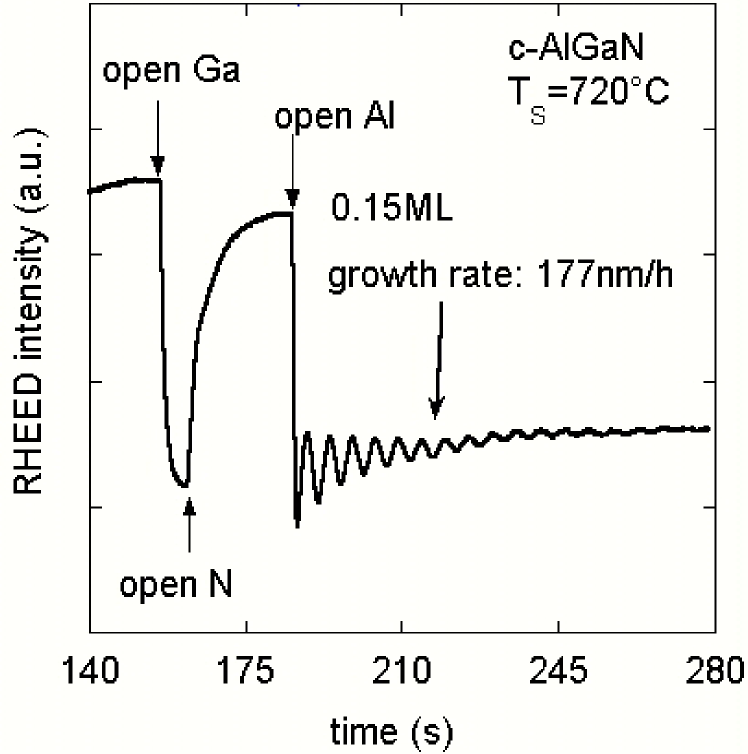

Figure 3.11: Measured RHEED intensity during the initial growth of $c-Al_{0.25}Ga_{0.75}N$. The RHEED intensity after opening the N shutter yields the amount of excess Ga on the c-GaN surface. After opening the Al shutter the excess of Ga increases and RHEED oscillations are observed indicating a two-dimensional growth mode with a rate of 177nm/h.

$c-Al_{0.25}Ga_{0.75}N$ layer. When the nitrogen shutter was opened with Ga on, an increase of the RHEED intensity was observed, indicating a Ga coverage of about 0.15ML due to the reduced Ga flux in comparison to the pure GaN growth. When the Al shutter was opened the intensity dropped down revealing an increase in the surface coverage to 1ML. The increase of the coverage is given by the additional metal flux and contains an exchange process in which the Ga incorporation in the layer is depleted by the Al due to the higher bond energy of Al-N of E_{AlN}=2.88eV [43] in comparision to Ga-N with

E_{GaN}=2.24eV [43]. Further clearly, weakly damped RHEED oscillations were observed, indicating a two-dimensional $Al_{0.25}Ga_{0.75}N$ growth mode at substrate temperatures of $720°C$ with a growth rate of 177nm/h. The surface diffusion length of aluminium is smaller than that of gallium, therefore one would expect RHEED oscillations with the growth of GaN rather then with AlGaN. However, our experiments show the opposite behavior. The reason for that is not clear, it may be due to a kind of surfactant effect of Ga on the (001) surface, similar to what has been reported for In on hexagonal GaN [44].

The relation between the flux ratio of the Al flux to the total metal flux and the Al

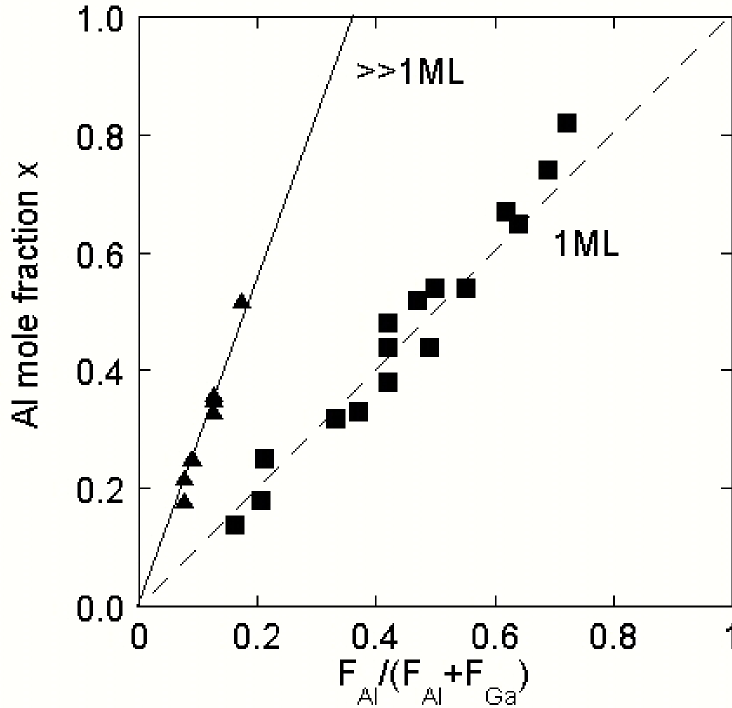

Figure 3.12: Relation between the Al mole fraction x of all $Al_xGa_{1-x}N$ and the flux ratio of Al to the total metal flux in the vapor phase for films grown under 1ML and >>1ML Ga coverage. The mole fraction was determined by HRXRD.

mole fraction x of the epilayer is drawn in Fig. 3.12. It was found that the Al content x was nearly linear proportional to the Al mole ratio of the vapor phase for the samples grown with 1ML and >>1ML Ga coverage. The linear increase indicate, that the Al was preferently incorporated. For the films deposited with 1ML coverage a 1:1 relation between the flux ratio and the Al content was observed, whereas for the Ga coverage much greater than 1ML the slope was >1 due to the higher amount of Aluminum in relation to the total metal flux.

In case of $In_yGa_{1-y}N$ growth, the growth rate depends on the In flux [45]. In order to verify similar behaviour during the growth of $Al_xGa_{1-x}N$, the growth rate of $Al_xGa_{1-x}N$ alloys was determined in a wide range of the Al mole fraction x. The data are summa-

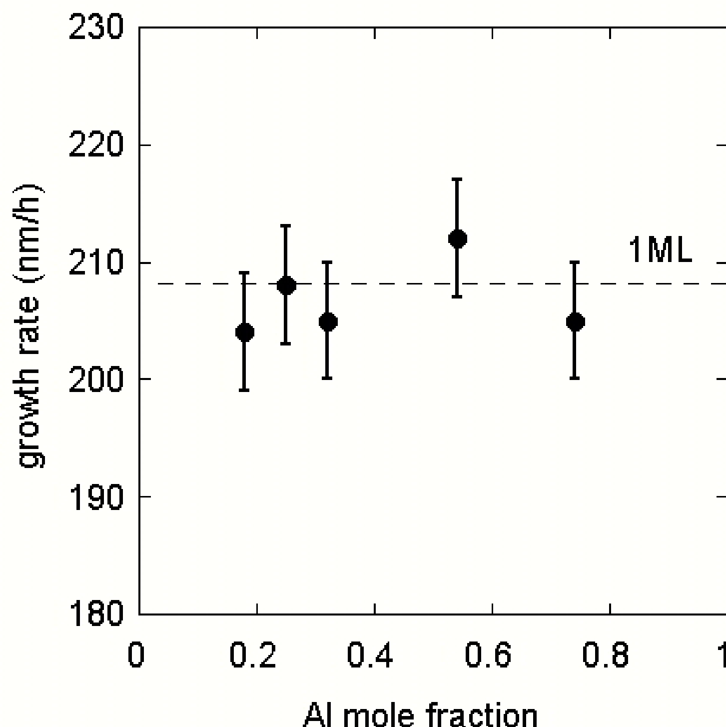

Figure 3.13: $Al_xGa_{1-x}N$ growth rate derived by RHEED oscillation and optical measurements for Al mole fraction between x=0 and x=0.74 at a constant nitrogen flux of $F_N = 2.2 * 10^{14} cm^{-2} s^{-1}$. The data reveal a constant growth rate for all AlxGa1-xN alloys independent on the Al flux.

rized in Fig. 3.13. The growth rate shows no markable change with varying Al mole fraction between x=0 and x=0.74. The observed variations are within the experimental error. So in contradiction to the $In_yGa_{1-y}N$ growth the Ga adlayer does not influence the nitrogen flow to the growing surface. The presence of a surfactant effect of Ga during the growth of $Al_xGa_{1-x}N$ is very useful for the optimization of the surface morphology.
The influence of the Al flux (i. e. the Al mole fraction) on the roughness of c-$Al_xGa_{1-x}N$ layers is depicted in Fig. 3.14. The RMS-roughness measured on a 5x5μm^2 area was constant with a value of 5nm over the whole Al range, if the films were grown under a Ga coverage of 1ML (circles). With increasing coverage (>>1ML) a strong dependence of the RMS roughness on the Al content was observed (triangles). The values increased from 2.5nm (GaN) to 22.5nm ($Al_{0.44}Ga_{0.56}N$) due to the formation of Ga droplets on the surface. The presence of droplets is investigated by optical microscopy.
The strain status is a further parameter, which influences the dislocation density. With increasing relaxation in the layer, the defect density increases (s ee chapter 2.1). The Fig. 3.15 shows a reciprocal space map (RSM) arround the (-1-13) reflex. In the RSM the reflex of the GaN buffer is observed at $q_{\|} = -1.97 \mathring{A}^{-1}$ and $q_{\perp} = 4.16 \mathring{A}^{-1}$ as well as the $Al_{0.25}Ga_{0.75}N$ film with $q_{\|} = -1.97 \mathring{A}^{-1}$ and $q_{\perp} = 4.23 \mathring{A}^{-1}$. The position of the AlGaN

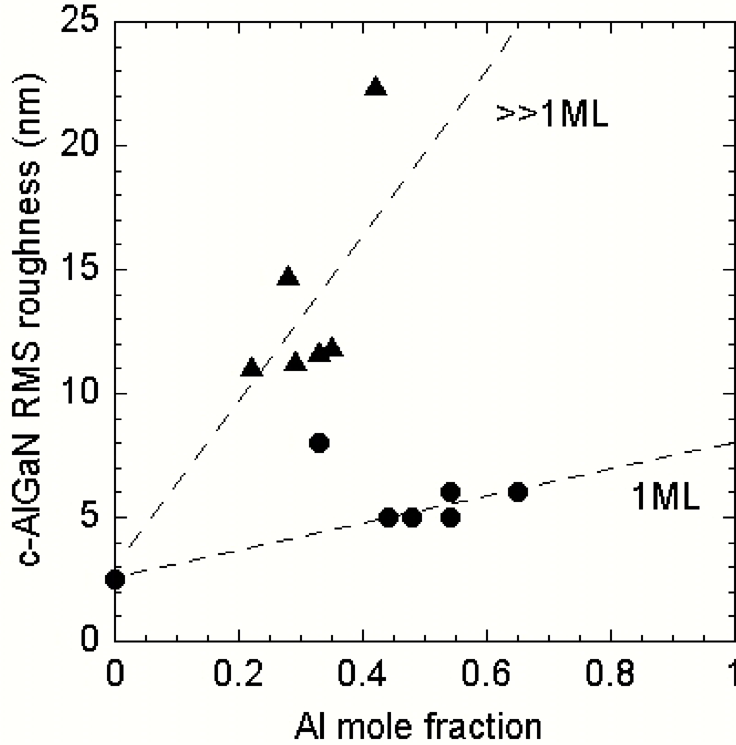

Figure 3.14: RMS roughness on a 5x5μm^2 area for $Al_xGa_{1-x}N$ alloys with an Al mole fraction between x=0 and x=0.74 grown under the coverage of 1ML (circles) and >>1ML (triangles) at 720°C. The lines are a guide for the eyes.

reflex relative to the GaN reflex indicates, that the AlGaN is pseudomorphic strained on the GaN (see chapter 2.1). This is confirmed by the observation that the relaxed AlN is located at $q_{\|} = -2.03\mathring{A}^{-1}$ and $q_{\perp} = 4.30\mathring{A}^{-1}$. The strain status as function of the film thickness for c-$Al_{0.25}Ga_{0.75}N$ layers is plotted in Fig. 3.16. The plot shows, that only for a thickness of 20nm the AlGaN layer is totally strained. With increasing thickness from 50nm to 450nm the strain is reduced from 0.8 to 0.3. The data are fitted using a 1/d dependence of the strain status on the thickness (dashed line). It is an interesting observation, that the films are still partially strained, because after Sherwin et al. is the critical thickness for an Al mole fraction of x=0.25 in the range of t=10nm [16]. The reason for deviation from theory is the high dislocation density. The high density forces the partial reduction of the strain energy at the dislocation lines, and therefore the layer relaxes at higher thickness than predicted by the model. But Sherwin et al. take only the screw dislocation into account. If other types of defect will also included in the calculation, the critical thickness will increase.

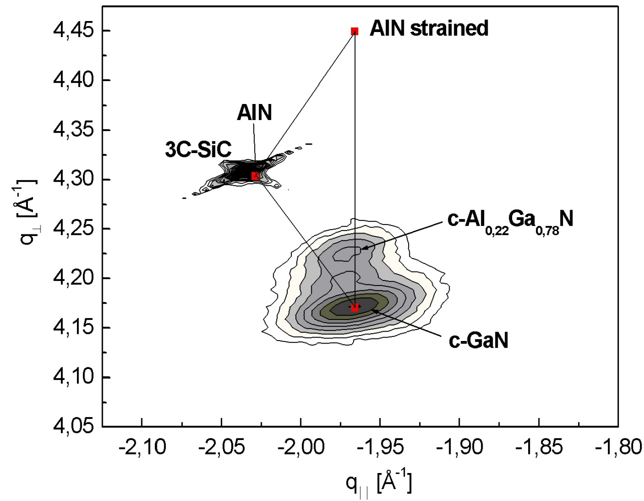

Figure 3.15: Reciprocal Space Map arround the (-1-13) reflex of an $Al_{0.25}Ga_{0.75}N$ film.

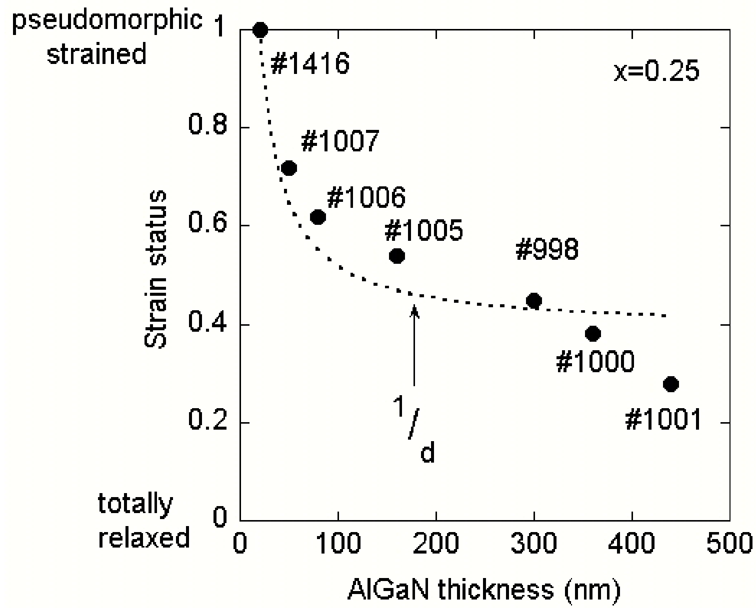

Figure 3.16: Strain status of $Al_{0.25}Ga_{0.75}N$ films as function of the layer thickness.

3.3 Electrical properties of GaN and AlGaN

A further important parameter are the electrical properties of our GaN and AlGaN layers, especially the unintentional doping level and the resistivity. The doping of the GaN and AlGaN determines for example the band diagram of the heterostructure and

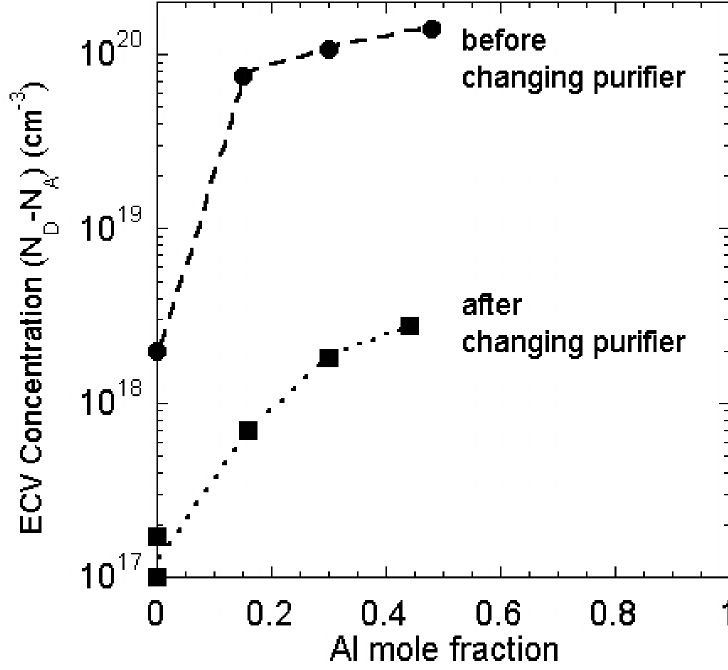

Figure 3.17: Unintentional doping level of $Al_xGa_{1-x}N$ films as function of the Al content x before (circles) and after (squares) change of the purifier.

therefore the density of the 2DEG (see chapter 6.1). On the other hand the resistivity, which includes the doping concentration, determines the suitability of a film as insulation layer in order to prevent parallel conductivity to the 2DEG.
In order to measure the background doping concentration some samples with a Al mole fraction between x=0 and x=0.48 are analyzed by electrochemical CV (ECV) [35]. The results of the measurements are depicted in Fig. 3.17. Two series of samples have been grown, one before changing the purifier and one series after changing the purifier. Before the change of the purifier in our nitrogen gas line (circles) the unintentional doping concentration of the c-GaN is about $N_D = 2 * 10^{18} cm^{-3}$ and increases to $N_D = 1.4 * 10^{20} cm^{-3}$ for an $Al_{0.48}Ga_{0.52}N$ layer. The increase of the concentration is caused by the high affinity of Al to oxygen. The aluminum forces the incorporation of oxygen into the AlGaN film. Oxygen acts as a shallow donor in the group-III nitrides if it occupies a N site, which is then responsible for the unintentional n-type doping. After changing the purifier (squares), which prevents oxygen contamination of the nitrogen gas, the doping of the GaN is reduced by two orders of magnitude down to $N_D = 1 * 10^{17} cm^{-3}$ and for the $Al_{0.48}Ga_{0.52}N$ down to $N_D = 2 * 10^{18} cm^{-3}$,respectively. Fitting the experimental data with a power function, it was found that 1 Al atom getters 1.4 O atoms. These concentrations are used for the calculation of the band diagrams in chapter 6.1.

The investigation of the resistivity of the AlGaN films are performed by a four point probe measurement [30](see also chapter 2.3.3). Due to the conducting nature of the substrate it is not suitable to perform Hall-effect measurements. The In contacts on the

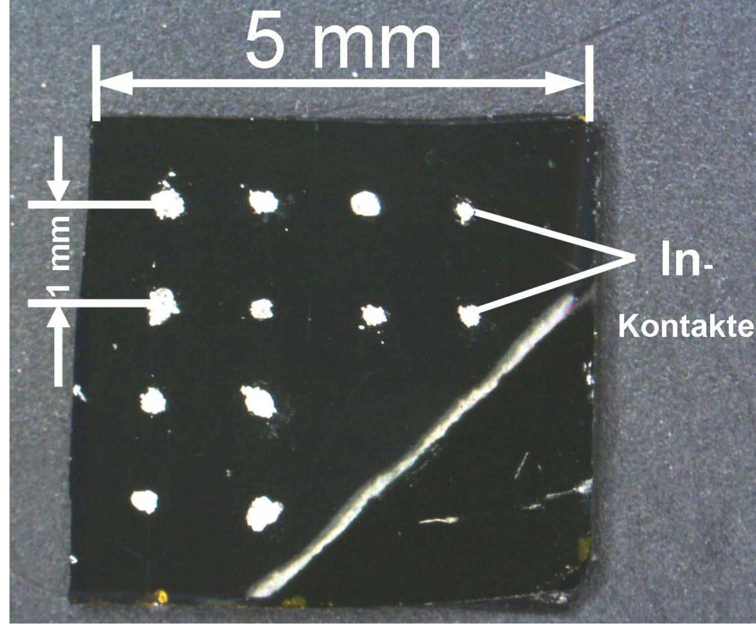

Figure 3.18: Photograph of the investigated AlGaN/GaN samples.

semiconductor surface are realized by microsoldering. The contacts have a diameter of $500\mu m$ and a distance of 1mm. A photograph of the sample with the contacts is shown in Fig. 3.18. The Fig. 3.19 illustrates the current circuit, used for the measurements. The total resistance R_{tot} is given by the three times the resistance between the inner probes $R_{2,3}$ and the serial resistance R_S of the outer probes:

$$R_{tot} = R_S + 3R_{2,3} \tag{3.6}$$

The resistance R_S is measured by the resistance of the In/AlGaN interface $R_{In/AlGaN}$, the resistance of the AlGaN layer R_{AlGaN}, the resistance of the GaN/AlGaN interface $R_{GaN/AlGaN}$, the resistance of the GaN R_{GaN}, the resistance of the GaN/SiC interface $R_{GaN/SiC}$ and the resistance of the 3C-SiC substrate R_{SiC}:

$$R_S = R_{In/AlGaN} + R_{AlGaN} + R_{GaN/AlGaN} + R_{GaN} + R_{GaN/SiC} + R_{SiC} = R_{AlGaN} + R_{Rest} \tag{3.7}$$

In R_{Rest} all the resistances without R_{AlGaN} are summarized. The resistance of the contacts as well as the interface resistances can be neglegted. R_S is dominated by R_{AlGaN}, because if $R_{AlGaN} << R_{Rest}$, the current flow is located in the AlGaN layer, and if $R_{AlGaN} >> R_{Rest}$, the AlGaN prevents the current flow into the substrate. Therefore R_{AlGaN} is calculated from:

$$R_{AlGaN} = R_{tot} - R_{2,3} - R_{Rest} \tag{3.8}$$

R_{Rest} can not be directly determined, but all the samples are grown on GaN/SiC layer with comparable values for R_{Rest}, so it is set constant, and changes in the total resistance

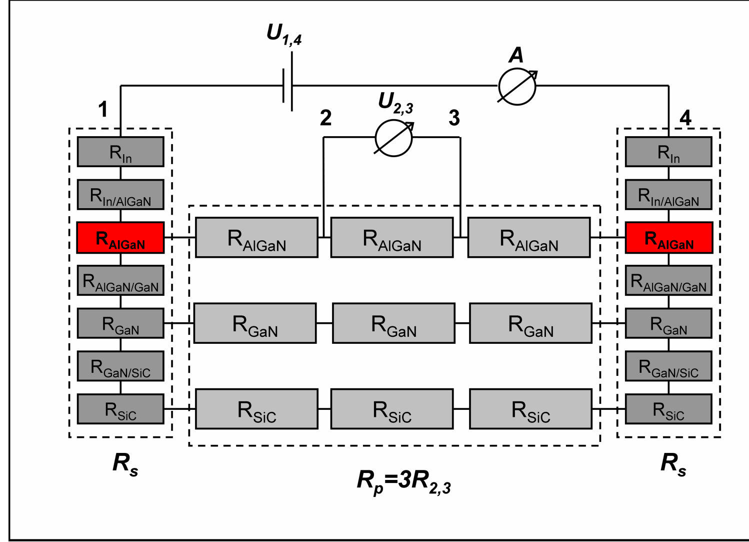

Figure 3.19: Equivalent current circle of the investigated AlGaN/GaN samples.

are caused by a change of R_{AlGaN}. From the calculated values for R_S of the AlGaN films, the resistivity is calculated using:

$$\rho_S(x) = \frac{R_S d_c}{t_{tot}} \tag{3.9}$$

where d_c is the diameter of the contacts and t_{tot} the total thickness of the sample including the substrate. For the determination of the resistivity the geometrical correction factors are taken into account [32]. The resistivity is then normalized to the resistivity of GaN and the ratio $\frac{\sigma(AlGaN)}{\sigma(GaN)}$ is plotted as a function of the Al content in Fig. 3.20 in a semilogarithmic scale. The lines are a guide for the eye. The plot shows an increase of the conductance by a factor of 3, if the Al content is increased up to x=0.4. With a further increase of the Al mole fraction, the relative conductance decreases to a value of 0.08 for a pure AlN layer.
In order to find an explanation for this behavior, some rough calculations were done. The conductance σ is given by:

$$\sigma = ne\mu \tag{3.10}$$

where n is the carrier concentration and μ the carrier mobility. The concentration is determined by:

$$n = \sqrt{\frac{N_C N_D}{2}} exp(-\frac{E_C - E_F}{2k_B T}) = \sqrt{\frac{N_C N_D}{2}} exp(-\frac{E_D}{2k_B T}) \tag{3.11}$$

where N_C is the effective density of states in the conduction band and E_D the ionization energy of the donor. N_C is given by:

$$N_C = 2(\frac{2\pi m_e^* k_B T}{h^2})^{3/2} \tag{3.12}$$

m_e^* is the effective electron mass given as function of the Al content [46]:

$$m_e^* = 0.15 + 0.15x \quad (3.13)$$

Knowing from Fig. 3.17, that the donor concentration increases with increasing Al content due to the incorporation of oxygen, the donor concentration as function of the Al mole fraction is approximated by:

$$N_D(x) \propto cx + 1 \quad (3.14)$$

From Ref. [47] the activation energy of the Si donor shows a strong dependence on the Al content. The binding energy varies from 20meV for GaN to 320meV for AlN and is linearly interpolated by

$$E_{act}(x) = 0.02 + 0.3x[eV] \quad (3.15)$$

Under the assumption that our residual donor behaves similar and using Equation 3.14 for the activation energy the carrier concentration can be approximated by:

$$n(x) \propto \sqrt{(cx+1)(0.15+0.15x)}exp(-\frac{(0.02+0.3x)}{2k_BT}) \quad (3.16)$$

The results of the calculation are depicted in the 3.20 and given by the curves. The

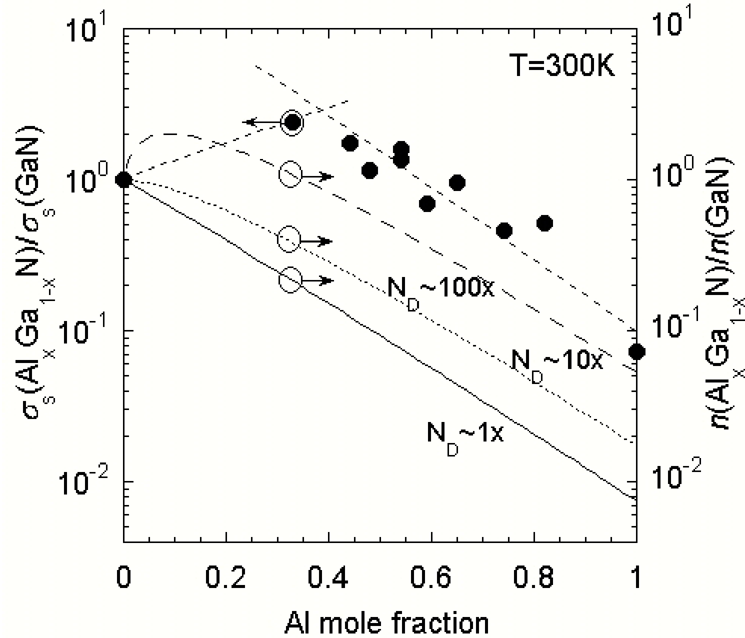

Figure 3.20: Relative conductance and carrier concentration as function of the Al mole fraction x.

values are also normalized to GaN. The curves represent different values for the constant c of 1, 10 and 100. The coefficient c takes into account the different affinity of O to Ga

and Al and is $c = \frac{N_{D,AlN}}{N_{D,GaN}}$. For example if c=100, the carrier concentration increases up to an mole fraction of 0.2, then the concentration starts to decrease again. Two points have to be taken in consideration. First, the residual donor will be with great probability O and the binding energy of O as a function of the Al content is unknown up to now. This may change Equation 3.14. The affinity of Al to O is quite different to the affiniity of Ga to O, this may change the value of c. Therefore the calculations have been performed for three different values of c, ranging from 1 to 100. In addition the mobility μ also enters the conductivity and the variation of μ is also unknown up to now. Nevertheless, with this simple model that with increasing Al content the depth of the donor binding energy increases and that Al has a higher affinity to O than Ga the tendency observed in Fig. 3.20 can well be explained. The not avaiable values for the mobility complicates the calculation of absolute values for the conductance of the AlGaN films, but our rough approximation describes the tendency in a good way.

4 GaN and AlGaN Schottky diodes

In this chapter the theory and physics of Schottky diodes based on cubic GaN and $Al_xGa_{1-x}N$ films will be described. Schottky diodes are the key elements for the realization of c-GaN based electronic devices such as high power high electron mobility transistors, high power metal semiconductor field effect transistors and UV photodectors. A short introduction in the general principle of the Schottky diode with the characteristic barrrier and the current-voltage (IV) behaviour will be given below.
In principle a metal-semiconductor structure can be designed in two ways: the first is the configuration as a Schottky contact in which the electron affinity of the semiconductor and the metal work function form a barrier and a depletion zone at the metal semiconductor interface, thus that termionic emission dominates the current flow. And second, in special cases, depending on the material parameter of the metal and the doping of the semiconductor, the depletion layer is so thin, that tunneling through the barrier dominates the current flow, leading to an ohmic behaviour.

4.1 Thermionic Emission Theory

The physics of a Schottky diode can very well be described by the thermionic emission theory. Due to the condition of thermal equilibrium (constant Fermi level) a potential barrier is formed at the metal-semiconductor interface. This barrier causes the formation of the depletion zone [28]. In case of Schottky diodes, the height and shape of the potential barrier can be influenced by an external magnetic or electric field. The barrier is normally located at or near the interface of a two-layer system like in pn-junctions or heterojunctions.
Figure 4.1 shows the energy band diagram of a separated metal and semiconductor. The work function of the metal is defined as:

$$W_A = q\phi_M \tag{4.1}$$

which is the energy, electrons need, to escape from the Fermi level to the vacuum level. In the semiconductor the work function is defined similar as $W_S = q\phi_S$. But with respect to the fact that in this case the Fermi level is located in a forbidden band, it is more useful to define a so called electron affinity $q\chi_S$. It is the difference between the vacuum level E_0 and the conduction band edge E_C:

$$q\chi_S = E_0 - E_C \tag{4.2}$$

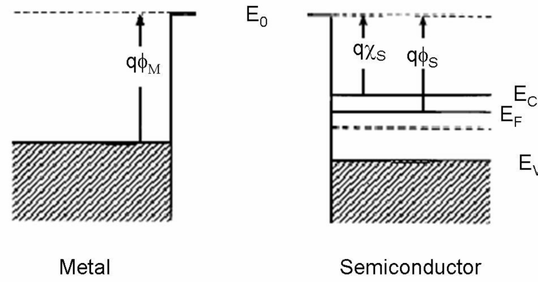

Figure 4.1: Schematic drawing of the energy bands of a metal and a semiconductor before contact.

The electron affinity for cubic GaN can be calculated from the known value for hexagonal GaN with $q\chi_S$=4.11eV [48]. Using the approximation that E_0-E_V is the same for both materials, we get for c-GaN $q\chi_S$=4.31eV, because $E_{g,c-GaN}$=$E_{g,h-GaN}$-0.2eV [49]. For the calculation the assumption of an n-type doped semiconductor is used and that the work funktion of the metal is larger than that of the semiconductor. Connecting both

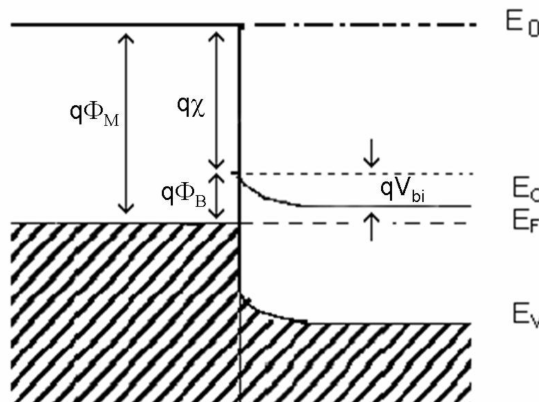

Figure 4.2: Schematic drawing of the energy bands of a metal and a semiconductor in contact.

materials, like plotted in Fig. 4.2, the formation of a potential barrier at the metal-semiconductor interface is observed. The height of the barrier is the difference between the metal work function and the electron affinity of the semiconductor:

$$q\phi_B = q(\phi_M - \chi_S) \tag{4.3}$$

We see also the relation between the built-in voltage V_{bi} and the barrier height:

$$q\phi_B = qV_{bi} + (E_C - E_F) \tag{4.4}$$

The Joyce-dixon approximation [50] is used to determine the difference of E_C and E_F:

$$E_F - E_C = k_B T[ln(\frac{n}{N_C}) + \frac{1}{\sqrt{8}}\frac{n}{N_C}] \tag{4.5}$$

in which n is the background carrier concentration and N_C the effective density of states, which is given by

$$N_C = 2(\frac{m_e^* k_B T}{2\pi\hbar^2})^{3/2} \tag{4.6}$$

With an effective electron mass of $m_e^* = 0.15m_0$ we get for the effective density of states $N_C = 1.7 * 10^{18} cm^{-3}$. This results in a difference of $E_F - E_C$=0.05eV using equation (4.5) and a background concentration of c-GaN n=$1 * 10^{17} cm^{-3}$.
The connecting of the metal and the semiconductor takes the Fermi levels in thermal equlibrium and causes a transport of carriers until the vacuum level becomes continuous at the interface. In the semiconductor a positive charge is present, whereas the metal will have a negative charge in order to guarantee electrical neutrality. The result of the charge transport is the formation of the band bending. In order to describe the transport of carriers under an external bias the thermionic emission theory by Bethe [51] is used. This theory is derived from the assumptions that the barrier height is much larger than $k_B T$, thermal equilibrium is established at the plane that determines emission and the existence of a net current flow does not affect this equilibrium. The current density $J_{S \to M}$ from the semiconductor to the metal is given by the concentration of electrons with energies sufficient to overcome the potential barrier and transversing in the z direction:

$$J_{S \to M} = \int_{E_F + \phi_B}^{\infty} q v_z N(E) F(E) dE \tag{4.7}$$

where $E_F + \phi_B$ is the minimum energy required for thermionic emission into the metal, v_z is the carrier velocity in the direction of transport and N(E) and F(E) are the density of states and the distribution function, respectively. If we postulate that all the energy of electrons in the conduction band is kinetic energy and V_{bi} is the built-in potential for zero bias we get for the current density:

$$J_{S \to M} = A^* T^2 exp(-\frac{q\phi_B}{k_B T}) exp(\frac{qV_{ext}}{k_B T}) \tag{4.8}$$

where

$$A^* = \frac{4\pi q m^* k^2}{h^3} \tag{4.9}$$

is the effective Richardson constant for thermionic emission, neglecting diffusion and V_{ext} the external applied voltage. For free electrons the Richardson constant is $120A^2cm^{-2}K^{-2}$. Since the barrier height for electrons moving from the metal into the semiconductor remains the same, the current flowing into the semiconductor is thus unaffected by the applied voltage. Therefore it must be equal to the current flowing from the semiconductor into the metal when thermal equilibrium prevails (i. e. when V_{ext}=0). The corresponding current density is obtained from equation (4.08) by setting V_{ext}=0,

$$J_{M\rightarrow S} = -A^*T^2exp(-\frac{q\phi_B}{k_BT}) \tag{4.10}$$

The total current density is given by the sum of equations (4.08) and (4.10):

$$J_n = [A^*T^2exp(-\frac{q\phi_B}{k_BT})][exp(\frac{qV_{ext}}{k_BT}) - 1] = J_S[exp(\frac{qV_{ext}}{k_BT}) - 1] \tag{4.11}$$

where J_S is called the saturation current density. The equation is similar to the transport equation for pn junctions and also known as Schottky-Mott-Model. However, the expression for the saturation current density is quite different.

If the height of the Schottky barrier is known, the width, the capacitance of the depletion layer and the built-in voltage can be calculated. In Fig. 4.3 the distribution of the ionized donors, the electric field and the electric potential is plotted. In case of a homogeneous doped semiconductor (first picture) using the assumption that we have an abrupt metal-semiconductor interface and no free carriers within the depletion zone, the following distribution of carriers is established:

$$\rho(z) = \begin{cases} qN_D & : \quad 0 < z < w \\ 0 & : \quad z > w \end{cases} \tag{4.12}$$

We get the bending of the potential by integrating the one-dimensional Poisson equation:

$$\frac{d^2V}{dz^2} = -\frac{\rho}{\epsilon\epsilon_0} \tag{4.13}$$

by

$$V(z) = \frac{qN_D}{\epsilon\epsilon_0}(z-w)^2 \qquad V(\infty) = 0 \tag{4.14}$$

where ϵ is the dielectric constant of the semiconductor, ϵ_0 the dielectric constant for the vacuum, N_D the donor concentration and w is the width of the depletion zone. The built-in voltage V_{bi} can be determined by the potential difference between the left and right side of the depletion zone

$$V_{bi} = V(0) - V(w) = \frac{eN_D}{2\epsilon\epsilon_0}w^2 \tag{4.15}$$

where the width of the depletion zone is equal to

$$w = \sqrt{\frac{2\epsilon\epsilon_0}{eN_D}V_{bi}} \tag{4.16}$$

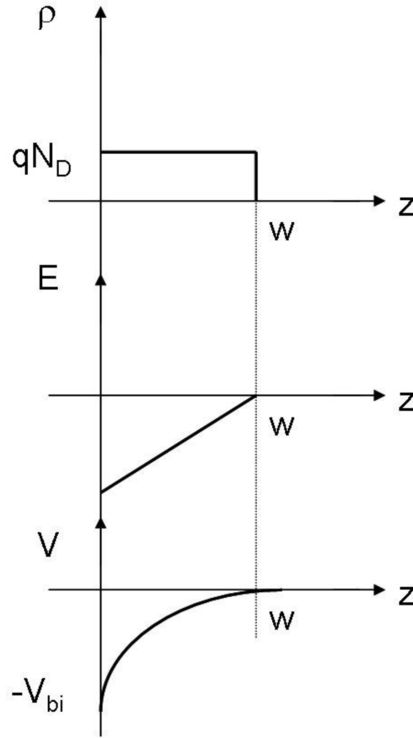

Figure 4.3: Schematic draw of the carrier distribution, the electric field strength and the potential (from upside to downside).

and in case of an externally applied field

$$w = \sqrt{\frac{2\epsilon\epsilon_0}{eN_D}(V_{bi} - V_{ext})} \tag{4.17}$$

The area near the edge of the depletion zone is conductive, but the zone itself is depleted and therefore an insulator. Therefore the structure is similar to a plate condensator, which includes a dielectric material with the width w and the dielectric constant ϵ of the material and the area A given by the size of the contact. The capacitance of the structure is then

$$C = \frac{\epsilon\epsilon_0 A}{w} = A\sqrt{\frac{\epsilon\epsilon_0 eN_D}{2(V_{bi} - V_{ext})}} \tag{4.18}$$

With the variation of the external voltage, the width of the depletion zone is changed, e. g. we have a charge transfer into the shallow impurities. If the capacitance is measured as the function of external voltage we get information about the concentration of shallow

impurities in the semiconductor. If equation (4.18) is written in the differential form, like

$$\frac{d(1/C^2)}{dV_{ext}}|_w = -\frac{2}{A^2\epsilon\epsilon_0 e N_D(w) V_{ext}}|_w \tag{4.19}$$

equal to

$$N_D(w) = -\frac{2}{A^2\epsilon\epsilon_0 \frac{d(1/C^2)}{dV_{ext}} e V_{ext}} \text{ and } w = \frac{\epsilon\epsilon_0 A}{C} \tag{4.20}$$

we are able to design a carrier concentration profile in connection with the width w of the depletion zone which is equal to the distance from the semiconductor surface.

For the investigation of the Schottky characteristics of c-GaN and c-AlGaN, samples

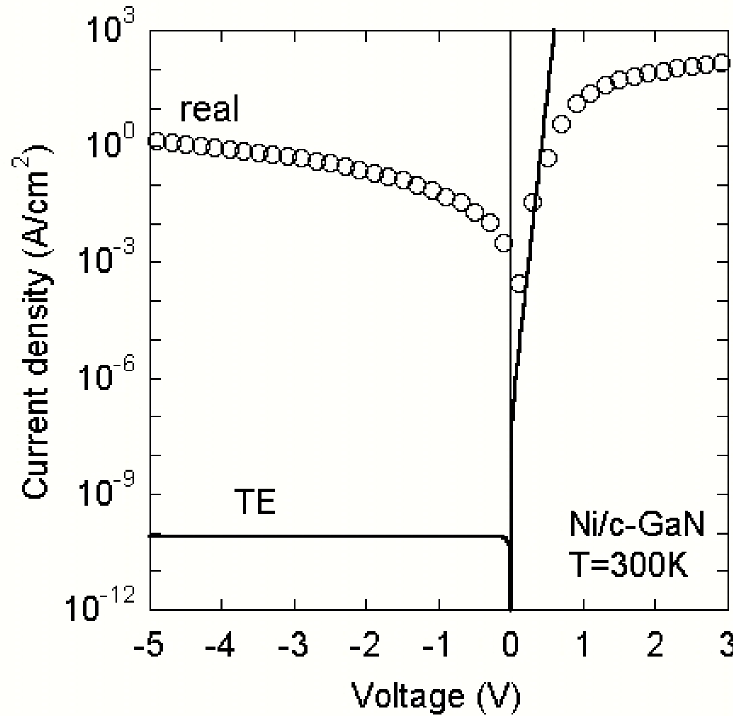

Figure 4.4: Comparison of the IV curve of a real Ni/c-GaN Schottky diode (GNJ1204) (open circles) and an ideal diode using the Schotty-Mott equation (solid line).

with the following structures are used: the GaN Schottky diodes consist of a 800nm-1000nm thick c-GaN layer deposited on 3C-SiC substrate at a temperature of $720°C$. The AlGaN diodes are grown on top of a c-GaN buffer with a thickness of 800nm with an AlGaN film thickness between 40nm and 100nm and an Al mole fraction varied between x=0.15 and x=0.35. The samples are cut into pieces of 5x5mm^2. Then Ni/In or Pd/In Schottky contacts with a thickness of 50nm/150nm are produced by thermal evaporation. The geometry of the contacts is defined by contact lithography having a diameter of 300μm. The ohmic contact is realized by pure In using the micro soldering technique. Details for the choice of the contact material and the thickness are given in

[52][53].
Figure 4.4 shows the semilogarithmic room temperature I-V curve of one of our Ni/c-GaN Schottky diodes (GNJ1204), which is measured in the voltage range between -5V and +3V(open circles). A clear nonlinear behaviour is observed, the current density in forward direction is about $160 Acm^{-2}$ at a voltage of 3V; whereas in reverse direction the current density is about $1.5 Acm^{-2}$ at a voltage of -5V. The solid line in the figure represents the current density across the Schottky diode, calculated by the model of Schottky and Mott, that assumes the current flow is dominated by thermionic emission. In the Schottky-Mott equation a saturation current density of $J_S = 7.6 * 10^{-11} Acm^{-2}$ is used. The saturation current density is calculated by using equation (4.11). We clearly observe a strong deviation between the theory and the experimental results. In forward direction the experimental values follow the theoretical prediction up to a voltage of 0.5V, for higher voltage the current flow is orders of magnitude less than given by the Schottky-Mott equation. In reverse direction also a discrepancy is observed. The measured current is ten orders of magnitude higher than the calculated saturation current of $J_S = 7.6 * 10^{-11} Acm^{-2}$ and in addition we see an exponential increase of the current density as function of the applied voltage instead of a constant reverse current. In order to find an explanation for these deviations, at first one has to look on the sample structure and how it can influence the electrical properties.
The schematic sketch of the contact arrangement, which is used for our c-GaN Schottky

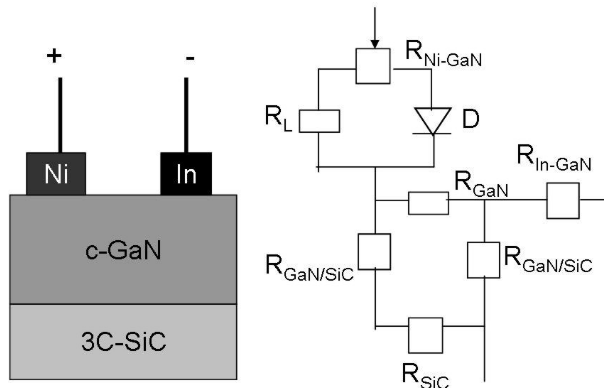

Figure 4.5: Arrangement of the metal contact used for the c-GaN Schottky diodes (left side) and the equivalent circuit (right side).

diodes is drawn in the left side of Fig. 4.5, as well as the equivalent circuit in the right side of the figure. The Schottky (Ni) contact and the ohmic (In) contact are deposited with a distance of 3mm on the GaN film. This arrangement is known as coplanar contact arrangement and offers some advantages in the electrical characterization especially in case of different types of substrates [52]. The right side of the figure illustrates the flow

of the current through the device. Starting with the Nickel contact the current has to pass the metal semiconductor interface, which is characterized by a transition resistance R_{Ni-GaN} and the Schottky diode. After this the current can flow by the GaN layer R_{GaN} as well as through the 3C-SiC substrate R_{SiC} and in the end it has to pass a second metal semiconductor interface, that of the ohmic (In) contact, which is characterized by a transition resistance R_{In-GaN}. At last one has to take into account that the GaN posses a lot of defects, which cause current transport, so that the diode itself has to be described by a diode in parallel arrangement with a leakage resistance R_L, which represents the influence of defects. All the resistances, which are not parallel to the diode can be summed as the series resistance R_S:

$$R_S = R_{Ni-GaN} + (\frac{1}{R_{GaN}} + \frac{1}{R_{SiC}})^{-1} + R_{In-GaN} \tag{4.21}$$

Using the assumption, that $R_{SiC} >> R_{GaN}$, we get for the serial resistance

$$R_S = R_{Ni-GaN} + R_{GaN} + R_{In-GaN} \tag{4.22}$$

The circuit of our Schottky diode can now drastically simplified: It consists only of the

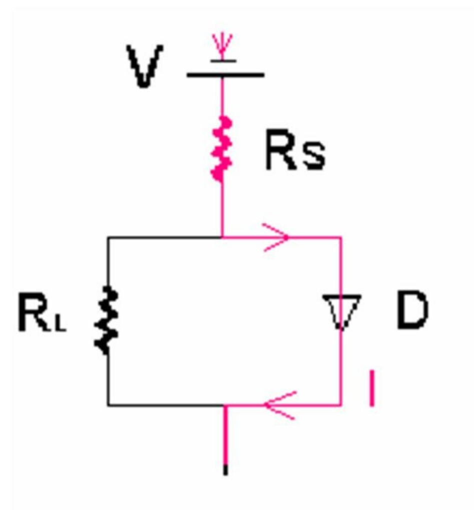

Figure 4.6: Sketch of the circuit for a real Schottky diode under forward bias.

ideal diode itself in parallel arrangement with the leakage resistance R_L and in serial arrangement with the serial resistance R_S, like it is drawn in Fig. 4.6. If a forward bias is applied to the structure, the current passes the serial resistance and flows through the diode, because its internal resistance can be neglected in comparison to the leakage

resistance. The voltage V_{ext}, which is measured, is the voltage over the serial resistance R_S plus the voltage over the ideal diode V_{diode}:

$$V_{ext} = JAR_S + V_{diode} \qquad \text{or} \qquad V_{diode} = V_{ext} - JAR_S \tag{4.23}$$

Using the thermionic emission theory [51] we assume that the current flow is dominated by thermionic emission of carriers over the Schottky barrier, taking into account that the barrier height is much larger than the thermal energy of the carriers, the current density in forward direction is given by

$$J = J_S exp(\frac{qV_{ext}}{nk_BT}) \tag{4.24}$$

The deviation from the ideal behaviour, due to recombination within the depletion zone or the dependence of the barrier height on the voltage is described by the ideality factor n. The serial resistance affects the I-V curve for voltages above V_{bi} [54]. First the forward direction will be discussed. Figure 4.7 shows the measured I-V curve (full circles) for

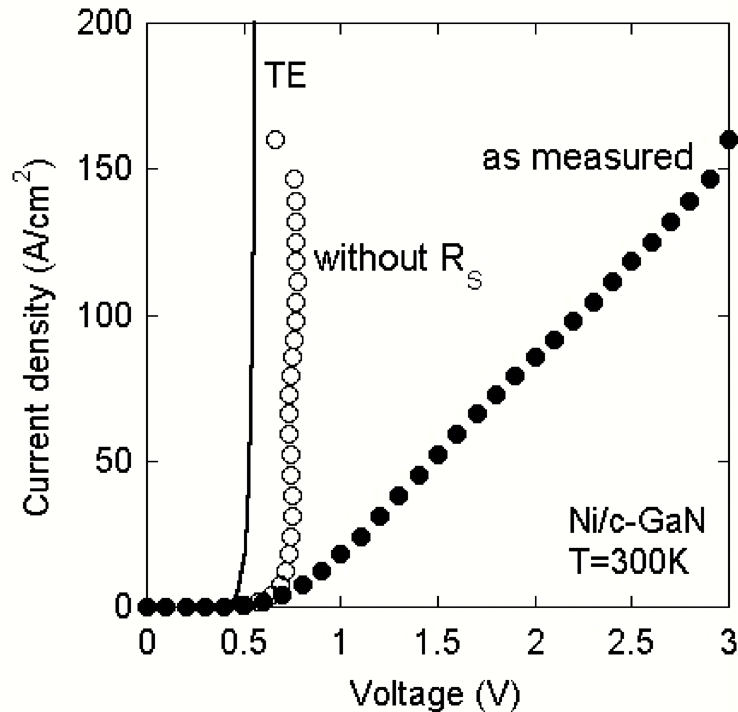

Figure 4.7: Comparision of the measured IV curve (full circles), without the limitation by the serial resistance (open circles) and the Schottky-Mott equation (solid line) in forward direction for GNJ1204.

sample GNJ1204 in a linear scale for voltages between 0V and +3V. A linear increase of the current density is observed as function of the forward bias for voltages above V_{bi}=0.7V. Using Ref. [54] one can evaluate a series resistance of R_S=21Ω. With this

value the voltage over the diode V_{diode} can be calculated using equation (4.22). The result of the calculation are plotted in the figure as open symbols. An exponential increase of the current density as function of the voltage is observed for voltages above V_{bi}=0.7eV, which is in good agreement with the prediction of the thermionic emission theory (solid line).
Neglecting the influence of the serial resistance equation (4.24)can be used in order to calculate the saturation current density as well as the ideality factor n. For J_S we get $J_S = 1 * 10^{-5} Acm^{-2}$ and for n=2.3. In comparision to h-GaN based Schottky diodes values of $J_S = 1 * 10^{-8} Acm^{-2}$ and for n=1.05, respectively are published in Ref. [55]. From that observation we conclude, that in our structures some mechanisms exist, which reduce extremely the performance of our diodes. In summary we think, that the forward current at room temperature is dominated by thermionic emission and can be described by thermionic emission theory.
However, if we focus on the reverse direction of the I-V charcteristics the behaviour is totally different. Using the same arrangement as in Fig. 4.6, only adapted for the reverse direction (see Fig. 4.8), the following is happened The current flows through the serial

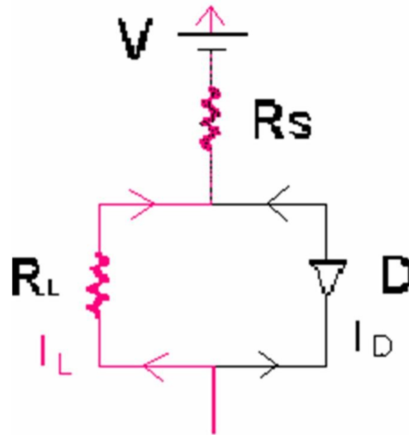

Figure 4.8: Sketch of the circuit for a real Schottky diode under reverse bias.

resistance and then parallel through the diode as well as through the leakage resistance. The total current density is then given by

$$J = J_S + \frac{V_{ext}}{AR_L} \tag{4.25}$$

The reverse current density is given by $J_S = 1 * 10^{-5} Acm^{-2}$ determined from the forward current characteristics. With the approximation that $J_S << J$, the leakage current

density J_L can be determined by

$$R_L = \frac{J_L A}{V} \tag{4.26}$$

So the leakage resistance is the inverse slope of the reverse I-V characteristic for voltages, which full fill the condition $eV >> k_B T$ [54]. This condition is fullfilled for voltages larger than 0.3V at room temperature. Figure 4.9 illustrates the comparison of the measured (full circles), the fitted (open circles) and the theoretical (solid line) saturation current density in reverse direction between -5V and 0V at room temperature. The

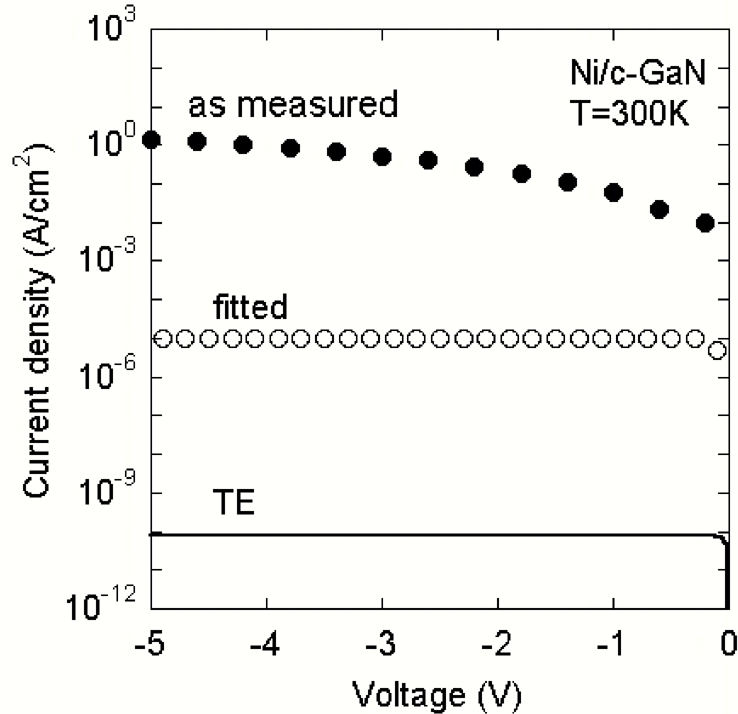

Figure 4.9: Comparison of the measured I-V curve (full circles), eliminating the influence of R_S (open circles) and the calculation using the Schottky-Mott equation (solid line) in reverse direction for GNJ1204.

inverse slope of the measured I-V curve reveals two things. First, that the magnitude of the reverse current is generally larger than the current density given by the fit and the thermionic emission model. Additionally, a nearly exponential increase of the reverse current is observed with increasing reverse voltage. Similar effects have also been measured with Schottky diodes on h-GaN [56] [57] [58]. They are explained by strong contribution of tunneling currents to the reverse current [59].

To identify the mechanism responsible for the large leakage current, we measured the IV curves of c-GaN and c-AlGaN Schottky diodes at temperatures between 50K and 300K. In Fig. 4.10 the results of the I-V measurements of a c-GaN Schottky diode are plotted in a double logarithmic scale in the voltage range of 0.01V to 1.5V for sample GNJ1204.

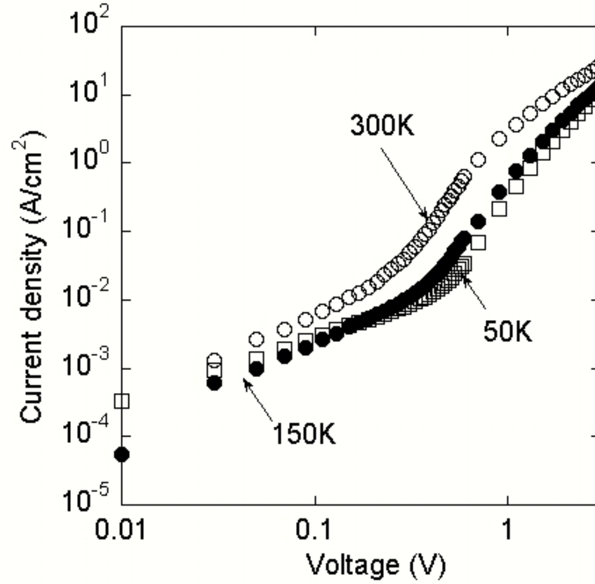

Figure 4.10: IV curves in forward direction measured at different temperatures of 300K (open circles), 150K (full circles) and 50K (open squares) of sample GNJ1204.

With increasing temperature an increase of the forward current density at a constant voltage is observed. The decrease of the serial resistance is due to an increase of the ionisation of impurities. We also see an increase of the current density with increasing voltage at a fixed temperature. The curvature is quite different for different temperature for voltages less than V_{ext}=0.7V. If one looks on the I-V curve measured at T=50K, the formation of a current plateau, which means a nearly constant current density, in the voltage range of 0.3V to 0.6V is observed. This was also found in h-GaN based Schottky diodes [60]. The plateau cannot be explained by thermionic emission. The current plateau still exists at a temperature of 150K, but it disappears at a temperature of 300K.

A pronounced deviation from thermionic emission transport across the barrier is evident from the reverse bias characteristics, which is plotted in Fig. 4.11 for temperatures of 50K (open squares), 150K (full circles) and 300K (open circles), respectively, for the sample GNJ1204. The magnitude of the reverse current density, plotted in a semilogarithmic scale in the voltage range from -5V to 0V shows a reduction of less than one order by decreasing the temperature from 300K to 50K. It is nearly independent on temperature and more than eight orders of magnitude higher than predicted by the thermionic emission model, especially at low temperatures. Further the current density shows a dependence on the reverse bias voltage and increases exponentially with increasing voltage.

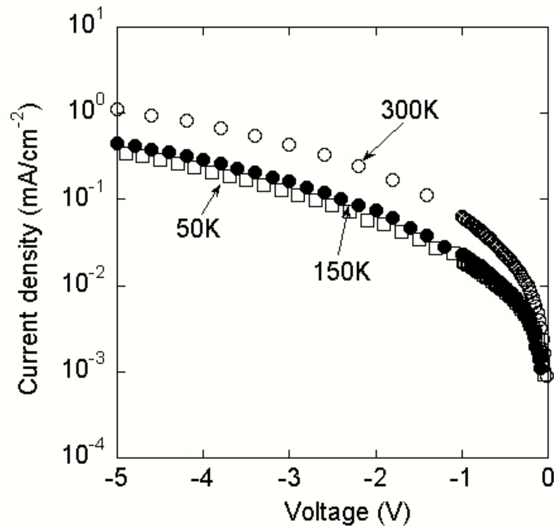

Figure 4.11: IV curves in reverse direction measured at different temperatures of 300K (open circles), 150K (full circles) and 50K (open squares) of GaN film (GNJ1204).

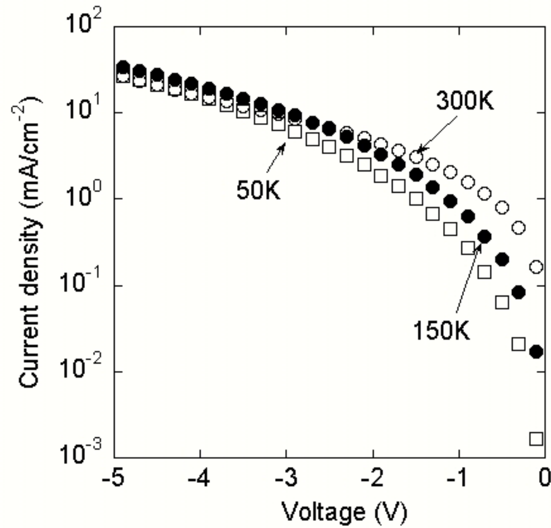

Figure 4.12: IV curves in reverse direction measured at different temperatures of 300K (open circles), 150K (full circles) and 50K (open squares) of a $GaN/Al_{0.35}Ga_{0.65}N/GaN$ heterostructure (GANS1352).

Similar effects were also observed in Pd/GaN/AlGaN/GaN based Schottky diodes. The Fig. 4.12 shows the reverse I-V characteristic of an GaN/AlGaN/GaN heterostructure with a GaN cap layer of 20nm and an AlGaN thickness of 40nm and an Al content of x=0.35 in the voltage range between -5V to 0V for different temperatures of 50K (open squares), 150K (full circles) and 300K (open circles). Here the current density for a fixed bias voltage is really independent on the temperature in the measured range, and further, that in comparision to GaN based diodes the current density for the GaN/AlGaN/GaN diodes is now one order of magnitude higher.

A further deviation from the thermionic emission theory is observed by the determina-

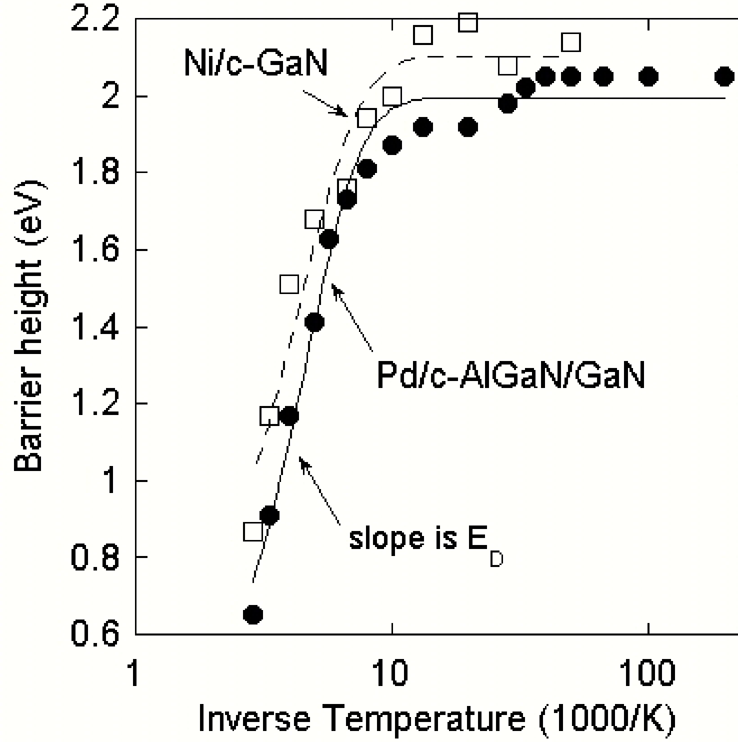

Figure 4.13: Temperature dependence of the Schottky barrier height calculated from the built-in voltage at different temperatures between 5K and 300K of a Ni/GaN (open squares)(GNJ1204) and a Pd/GaN/AlGaN/GaN (full circles) (GANS1352) Schottky diode.

tion of the Schottky barrier height using equation 4.4 and 4.5 at various temperatures. The barrier height $q\phi_B$ is calculated from the measured built-in voltage V_{bi} using

$$q\phi_B = qV_{bi} - k_BT[ln\frac{n}{N_C} + \frac{1}{\sqrt{8}}\frac{n}{N_C}] \tag{4.27}$$

Figure 4.13 illustrates the Schottky barrier height for a Ni/GaN (open squares) and Pd/GaN/AlGaN/GaN (full circles) Schottky diode in the temperature range from 5K to 350K as Arrhenius plot. The Schottky barrier height of the Ni/GaN diode increases

from 0.87eV at 350K to 2.14eV at 50K and in case of the Pd/GaN/AlGaN/GaN from 0.65eV at 350K to 2.05eV at 5K.
In case of the AlGaAs/GaAs system the changes in the barrier height can not be explained by thermionic emission, it is caused of the pinning of the Fermi level due to the presence of ionizied defects near the semiconductor metal interface [61][62]. In this case, the temperature change of the barrier would reflects the temperature motion of the defect relative to the appropriate band edge,i. e. their ionization energy. The Fermi level is pinned at an occupied localized defect state, whose wavefunction is mainly of a bonding type. Thermal ionization of such a state involves the release of free carriers. The change in concentration of free carrier induces the temperature dependence of the barrier height [63]. In other words from the Arrhenius plot in Fig. 4.13 we can estimate the ionization energy of these defects. We get for the Ni/GaN diode a value of $E_A = 51meV$. In the Pd/AlGaN/GaN diode the same ionization process occures, because it can be fitted to a value of $E_A = 56meV$. These results indicate that in the case of GaN and AlGaN the same type of defects are present near the semiconductor surface. The experimental value fits very well to the ionization energy of oxygen in GaN [49].

4.2 Thin Surface Barrier Model

For the hexagonal group-III nitrides a simple model is developed by Hasegawa et. al [60]. The so called Thin Surface Barrier (TSB) model postulates a high densitity of unintentional defect donors near the semiconductor surface (in agreement with the AlGaAs/GaAs system) which reduces the width of the barrier (in contrast to the AlGaAs/GaAs) in such a way that the tunneling probability for electrons through the barrier is increased. If we look to the temperature dependence of the barrier height in the hexagonal nitrides, an opposite behaviour is found in comparison to the GaAs and c-GaN systems, here a decrease of the barrier height with decreasing temperature is observed, caused by the Schottky effect. Both models use the same reason in order to explain the anomalous current transport by thermionic field induced electron tunneling. But only the model of Hasegawa can explain the current flow and the formation of the current plateau in the forward direction. The model is characterized by the presence of donor states within a thin layer at the surface below the Schottky barrier, having a thickness d, a density N_{SD} and an effective barrier height ϕ_B. The current through the region with the surface states is dominated by thermionic field emission (TFE).
Figure 4.14 shows the influence of the TSB regions on the band diagram of our Schottky diodes. For a quantitative description, we assume, that lateral extension of each region is much larger than the value of d, so that the one-dimensional treatment of the current transport is possible using the band diagram in Fig. 4.14. It is formed on a surface of an n-type semiconductor with a bulk doping of N_D. In Fig. 4.14, the potential at the boundary x=D is defined as ϕ_D. If V_0 is defined as the bias voltage at which $\phi_0 = \phi_D$

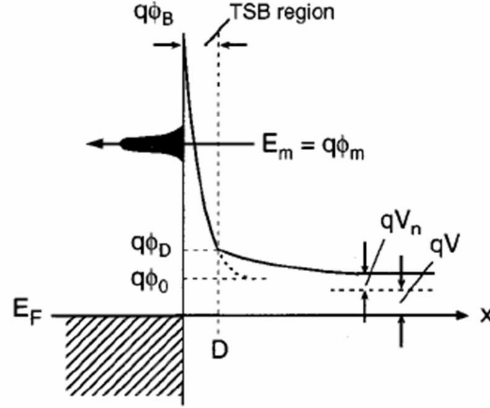

Figure 4.14: Schematic sketch of the Thin Surface Barrier (TSB) model.

holds, then V_0 and ϕ_0 are given by the following equations:

$$V_0 = \phi_B - \frac{eN_{DS}}{2\epsilon\epsilon_0}D^2 - V_n \tag{4.28}$$

in which V_n is given by

$$V_n = k_B T log(\frac{N_C}{N_D}) \tag{4.29}$$

If $V_{ext} < V_0$ the height $q\phi_0$ is given by

$$\phi_0 = \frac{eN_D}{2\epsilon\epsilon_0}(1 - \frac{N_D}{N_{DS}})(\sqrt{\frac{2\epsilon\epsilon_0}{eN_D}(V_0 - V_{ext}) + D^2} - D)^2 + V_{ext} + V_n \tag{4.30}$$

and if $V_{ext} > V_0$ the height $q\phi_0$ is given by

$$\phi_0 = V_{ext} + V_n \tag{4.31}$$

Following similar steps by Padvani and Stratton [64] one can calculate currents by the TFE/TE process. The value of ϕ_0 is an important parameter for the thermionic field emission and determines the amount of current caused by tunneling. The energy position of the maximum of the tunneling current is then

$$\frac{\phi_m - \phi_0}{\phi_B - \phi_0} = \frac{1}{cosh^2(E_{00}/k_B T)} \tag{4.32}$$

where $E_{00} = \frac{\hbar}{2}\sqrt{\frac{N_D}{m^*\epsilon\epsilon_0}}$ is the so called tunneling Parameter. So the density of surface donors and the background carrier concentration determines the amount of current

caused by thermionic emission or by tunneling through the TSB regions as function of the external voltage. This dependence is responsible for the formation of the current plateau in forward direction as shown in Fig. 4.15. If the thickness of the TSB regions

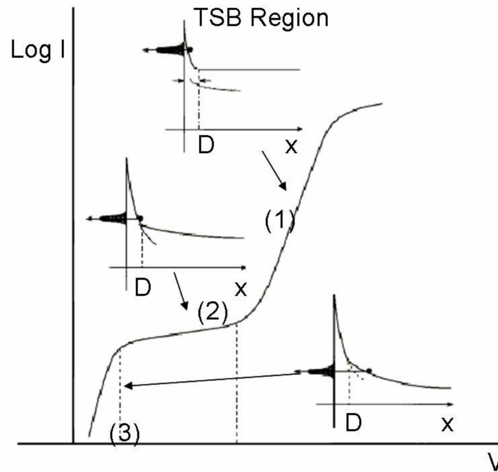

Figure 4.15: Schematic sketch of the formation of the current plateau in the forward direction of a Schottky diode.

becomes small (a few nm), V_0 becomes large and at low temperatures three different ranges in the I-V characteristics occur:

- The first region given by $V_{ext} > V_0$ is determined by localization of the depletion zone within the TSB region, and the thermionic field emission process through the TSB is direct proportional to the external voltage.
- In the second region, given by $V_0 < V_{ext} < V_D$ in which V_D is the voltage when $\phi_D = \phi_m$, meaning that the energy maximum of the TFE is equal to the minimum of the parabola. So we have TFE process through the barrier, but the current dependence on the voltage is compensated by the decrease of the voltage in the bulk, which ends in the formation of the plateau.
- In region three, for voltage above V_D the TFE enters the bulk material and the TFE decreases, because the influence of the barrier thickness disappears.

The relevant donor like defects may be nitrogen vacancies [60], other possible candidates are oxygen impurities, their density is expected to be high in AlGaN films due to the increased affinity of Al to O, which is supported by the fact, that the leakage current in the AlGaN/GaN Schottky diodes is even higher than that of GaN based diodes (see

Fig. 4.19).

A very useful method to determine the carrier type and concentration of the defects

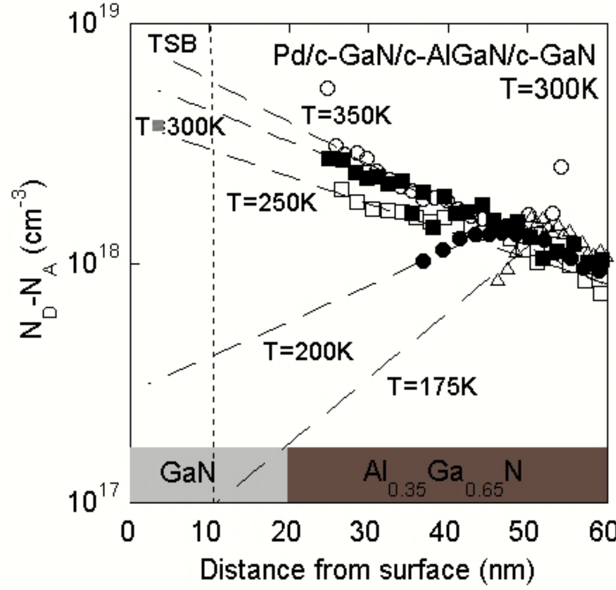

Figure 4.16: Carrier concentration profile of a Pd/c-GaN/c-AlGaN/c-GaN Schottky diode (GANS1352) measured at temperatures between 175K and 350K.

is the measurement of the Hall effect. But in our case it is not possible due to the conducting nature of the 3C-SiC substrate. The second is, the carrier concentration is needed near the semiconductor surface and not in the bulk material. In our case the best way is to use the Schottky diode itself as a probe and measure C-V. This allows us to measure a concentration profile as from the surface using equation (4.19). In Fig. 4.16 a calculated concentration profile is plotted in a semilogarithmic scale versus distance from the surface of a Pd/c-GaN/c-AlGaN/c-GaN Schottky diode (GANS1352) for temperatures between 175K and 350K. The plot shows an exponential decrease of the carrier concentration from $n = 3 * 10^{18} cm^{-3}$ at a depth of 20nm to $n = 1 * 10^{18} cm^{-3}$ at 60nm, which means a very high concentration of donors near the semiconductor surface. In order to determine the amount of donor states near the surface, we extrapolate the concentration profile exponential to a depth of 10nm, which is a reasonable value for the thickness of the TSB. For a temperature of 350K a concentration of $n = 5.6 * 10^{18} cm^{-3}$ is calculated. This value decreases with decreasing temperature, for T=200K it is only $n = 4.1 * 10^{17} cm^{-3}$. The reduction in the donor concentration is caused by the freeze-out of the carriers at their impurities. However, we have shown, that c-GaN and c-AlGaN/GaN based Schottky diodes suffer from abnormal large leakage current under reverse bias, which strongly degrade gate control characteristics and increase power consumption. This anormalous high current is caused by a high density of surface donor states with a density of $N_D - N_A = 4.2 * 10^{19} cm^{-3}$ at room temperature. A promising

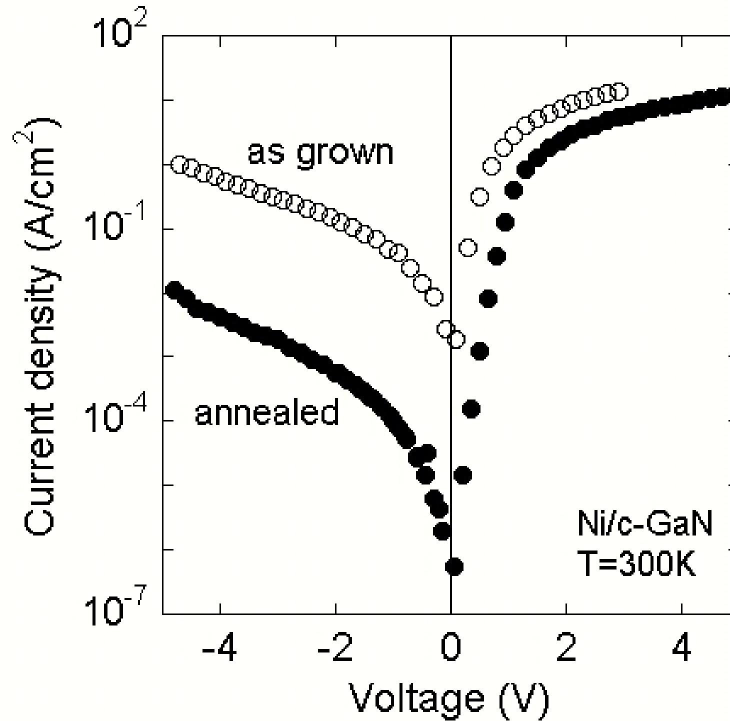

Figure 4.17: Room temperature current voltage characteristics of a Ni/c-GaN Schottky diode (GNS1285) before annealing (open circles) and after annealing in air at 200C (full circles).

canditate for the donor states is oxygen owning an activation energy of 51meV, which is in good aggrement with the values given in the literature [49].
For an improvement of the performance of our Schottky devices the density of surface donors have to be reduced. In our case there are two possibilities for the reduction. First the reduction of the oxygen background during growth. This can be achieved by the use of high purity nitrogen or mounting chemical purifiers in front of the plasma source. The second possibility is a post growth process. One promising process is the thermal annealing of the structure in air. This is done for a Ni/c-GaN Schottky diode on a hot plate located on a lab bench in open room air for 10min at 200C. The Fig. 4.17 shows the I-V curves before and after the annealing. In the figure the IV characteristics of the Ni/c-GaN Schottky diode before (open circles) and after (full circles)annealing are plotted in a semilogarithmic scale as function of the bias voltage in the range from -5V to 5V measured at T=300K. In the as grown characteristics the typical I-V behaviour of our Schottky diodes is observed. If we now focus on the I-V curve after the annealing step we see a dramatic change. In the forward direction, the current density reveals a weak change, the serial resistance increases from 230Ω to 310Ω. On the other hand, the barrier height increases from 0.6eV to 1.2eV using equation 4.27. Further observations could be seen in the reverse direction. If the current density before and after the an-

nealing step is compared, a decrease of the current density by two orders of magnitude is measured, however the exponential increase with increasing voltage still exists. The results show that the density of surface donors can be reduced by the annealing due to the reduction of the current, but they are still present and dominating the reverse current. These donor like defects maybe compensated by Ga_4Ni_3; Ni_3N and Ni_4N clusters which are formed during the annealing at the Ni-GaN interface [65].

4.3 Breakdown Voltages of Schottky Diodes

A very important parameter in the field of device performance is the size of the breakdown voltage. The breakdown voltage V_{BD} is defined by the reverse voltage at which the avalanche breakdown of the carriers occurs. The result is a very high current in reverse direction, which destroys the diode. It would be an interesting point if thermal annealing can influence the density of surface donor states and the breakdown voltage. In Fig. 4.18 the I-V curves of an as grown (GNJ1204) and an annealed (GNS1285) Ni/c-

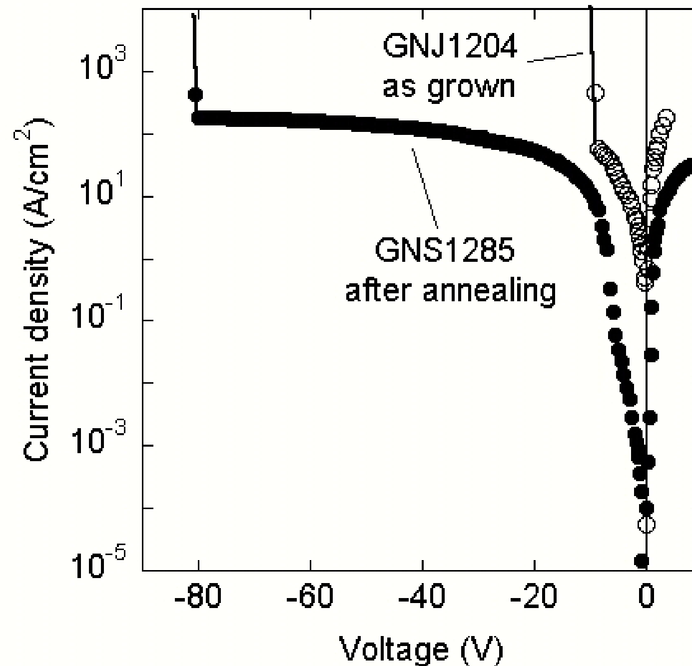

Figure 4.18: Breakdown voltage of Ni/c-GaN Schottky diode before annealing (GNJ1204) (open circles) and after annealing in air at $200C$ (GNS1285) (full circles).

GaN diode are plotted in a semilogarithmic scale for voltages between -90V and +10V. For both devices the breakdown is observed, due to the huge increase of the current density in reverse direction. In case of the as grown sample the breakdown occurs at

V_{BD}=-9V. For the annealed sample a saturation of the current density is measured at about $150 Acm^{-2}$ and the breakdown occurs at a voltage of -80V, which is nearly one order of magnitude higher than for the as grown sample.

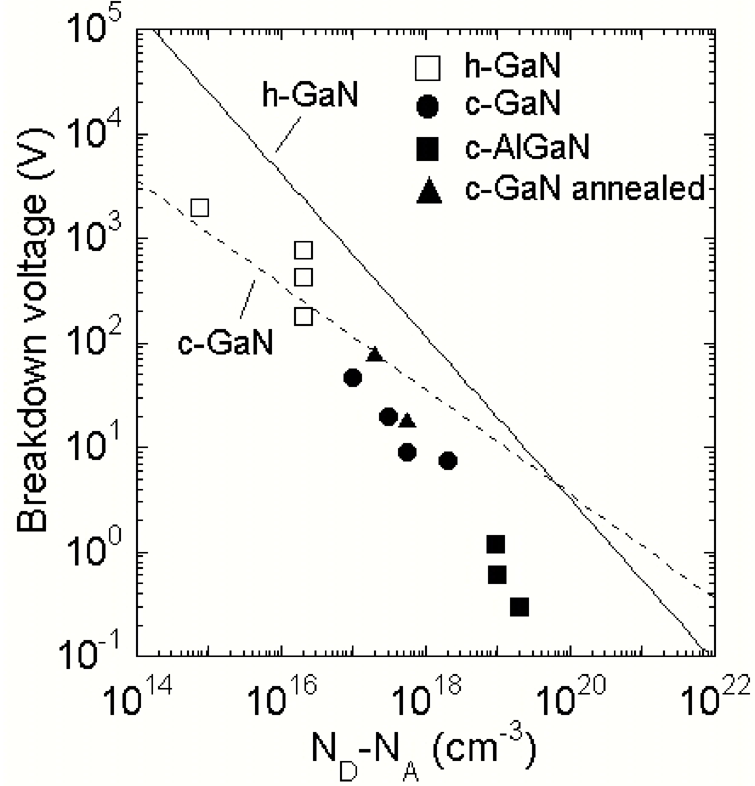

Figure 4.19: Breakdown voltages vs net donor concentration of Schottky diodes on c-GaN and c-AlGaN (full symbols) and h-GaN (open symbols).

Figure 4.19 shows the breakdown voltages V_{BD} of Schottky diodes on c-GaN and c-AlGaN plotted versus the net donor concentration of the semiconductor (full symbols). The donor density $(N_D - N_A)$ is measured either by CV or ECV. Also included in the figure are experimental data obtained from h-GaN [67][68]. The lines in Fig. 4.19 are calculated using a model for the relation between V_{BD} and the net donor concentration [66]. Using this model the breakdown voltage V_{BD} is given by

$$V_{BD}[V] = 3.5 * 10^{10}(\frac{cm^{1.5}}{V}) * N_D[cm^{-3}]^{-0.5} \tag{4.33}$$

Our experimental data clearly follow the trend of increasing V_{BD} with decreasing donor concentration. However, all experimental values of V_{BD} are one-third smaller than the calculated values. We suggest that the TSB leads to premature breakdown. Our interpretation is supported by experimental data obtained with c-AlGaN/GaN Schottky

diodes (full squares) where an even larger difference between experimental and calculated data is observed. We suppose that this difference is to a high oxygen concentration in the TSB region. In case of the annealed sample the breakdown voltage of 80V fits very well to the prediction by the theoretical calculation. We believe that the effect of compensation of the donors prevent the premature breakdown.

5 Photoconductivity in GaN based Schottky diodes

In order to investigate the suitability of c-GaN for photodetector applications, a 750nm thick c-GaN layer is deposited directly on freestanding 3C-SiC at a substrate temperature of $T_{subs} = 720°C$ (GNS1382). A schematic sketch of the sample structure is given

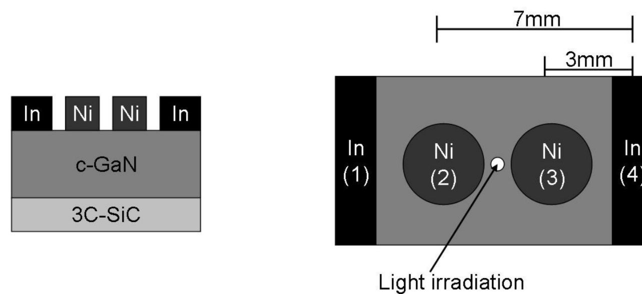

Figure 5.1: Experimental setup for the investigation of the photoconductivity: a) sample structure b) contact arrangement.

in Fig. 5.1a.
The sample is cut into a piece of 5x10mm^2 and the electrical contacts were formed. Firstly the Schottky contacts are generated. They are structured by photolithography using a hole mask with a diameter of 1mm. Then the Ni was deposited by thermal evaporation under UHV conditions using a thickness of t=12nm. The thickness is selected in that way that due to the optical absorption coefficient of Ni ($\alpha = 9.489 * 10^7 m^{-1}$),the thickness guarantees a high transmittivity (about 32%) as well as the high mechanical inertness and electrical conductivity. The ohmic contact for the test of the Schottky diodes are made of In pads with a size of 1x5mm^2 which are realized by soldering technique at the edges of the sample (see also Fig. 5.1b).
Before the sample is exposed with light in order to exhibit the generation of a photon induced current, it has to be proved that the contacts for the MSM show Schottky characteristics, so the sample is firstly mounted into the IV measurement setup. Both Ni contacts are connected to the positive potential and the In pads are connected to the negative potential. The Fig. 5.2 depicts the result of the measurement taken at room temperature for a voltage between -5 and +5V. The current density is plotted vs. the bias voltage in a linear scale. A clear rectifying characteristics under reverse bias was

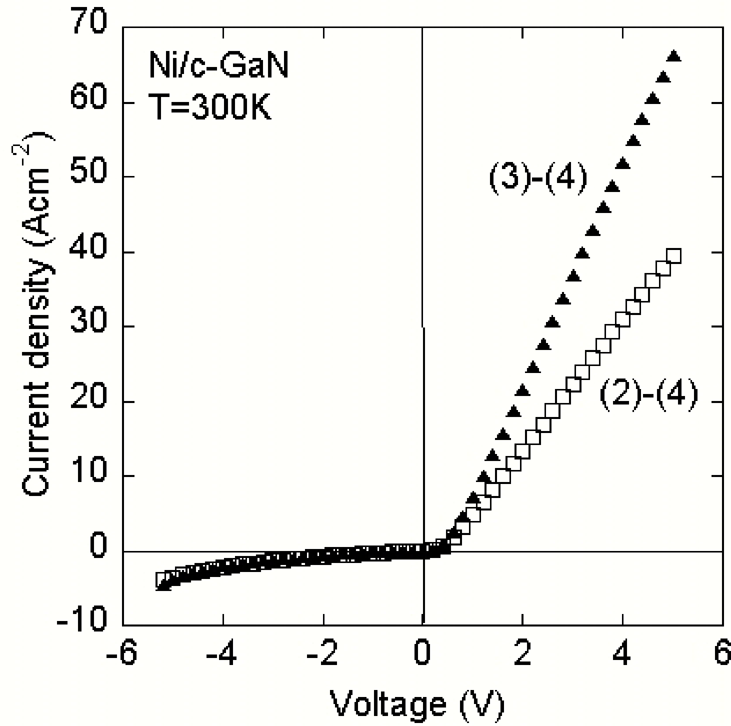

Figure 5.2: IV curves of the Schottky contacts on a 750nm c-GaN measured (GNS1382) at T=300K.

observed having a current of $4Acm^{-2}$ at a voltage of -5V for both contacts, whereas in forward direction the current reaches a value of $66Acm^{-2}$ for contact 3 and $40Acm^{-2}$ for contact 2 at a forward voltage of +5V. The differences in the forward characteristics have their origin in the additional series resistance (longer distance Ni(2)-In(4) contact than Ni(3)-In(4)) for the second diode. Additional a clear Schottky barrier of 0.5V is measured in both cases by the built-in voltage.
In the next step the IV characteristics between both Ni contacts is measured in order to investigate the dark current behaviour of the structure in the voltage range between -5V and +5V. So it was able to measure the reverse current of one of the Schottky diodes in every direction due to the symmetric arrangement. In Fig. 5.3 the IV curve between both Ni contacts (2)-(3) is plotted versus the bias voltage in the range of -5V to +5V. The curvature of the IV curve is symmetric. In the case of positive potential the current increases up to $4Acm^{-2}$ at a voltage of +5V and on the other side we have -$3Acm^{-2}$ at a negative potential of -5V. The measured current density fits very well to results of the reverse current of the Schottky diodes obtained from Fig. 5.2. So the principle operation of the structure is given due to the Schottky characteristics of the Ni contacts and the symmetry in their IV curve.
In order to investigate the properties of c-GaN as photodetector material, the sample has to be irradiated with light. The influence on the electrical properties of the c-GaN can be investigated using two different methods. This can be realized in to ways. The

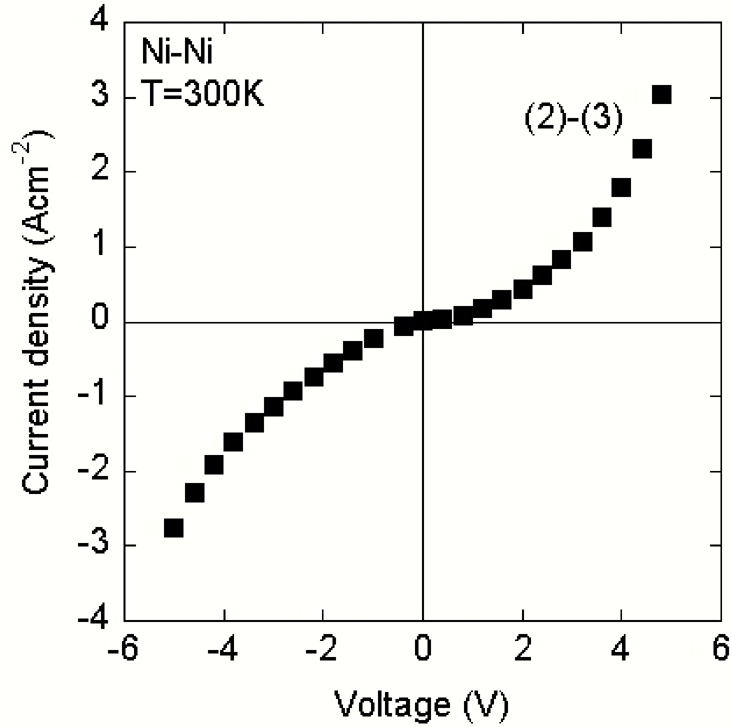

Figure 5.3: IV curve of the Ni Schottky contacts (2)-(3) on a 750nm c-GaN (GNS1382) measured at T=300K.

current can be measured as a function of the wavelength for a fixed bias voltage or as a function of the bias voltage for a fixed wavelength, which is the so-called photoresponse. The second possibility is easier to realize, because this can investigated using the PL setup. The measurement has to be done in the darkness and then repeated under the irradiation of light using a excitation energy which is above the bandgap of GaN in order to guarantee photon absorption. The effective photo current is calulated as the difference of the light and the dark IV curves.

The Fig. 5.4 illustrates the results of the two measurements. Here the current density is plotted as function of the bias voltage between -5 and +5V in a linear scale. The open circles represent the values for the measurement in the darkness, and the full squares show the values for the analysis under light illumination. Again a symmetric behaviour is observed in both cases for the IV curves and in case of irradiation the current is much higher than under dark conditions, caused by a reduction of the serial resistance under illumination. The change in the serial resistance is due to the influence of the photoinduced current. The serial resistance R_S is determined by the resistivity of the c-GaN. From equation 3.10 it is known, that the resistivity is proportional to the free carrier concentration n. So a decrease of R_S will lead to an increase of n, which are generated by the absorption of the laser light. At +4V the dark current is about $4Acm^{-2}$ and under illumination about $6Acm^{-2}$. In contradiction to the theory of Schottky diodes the dark current of the structure is much higher (see chapter 4.1). Normally it is given

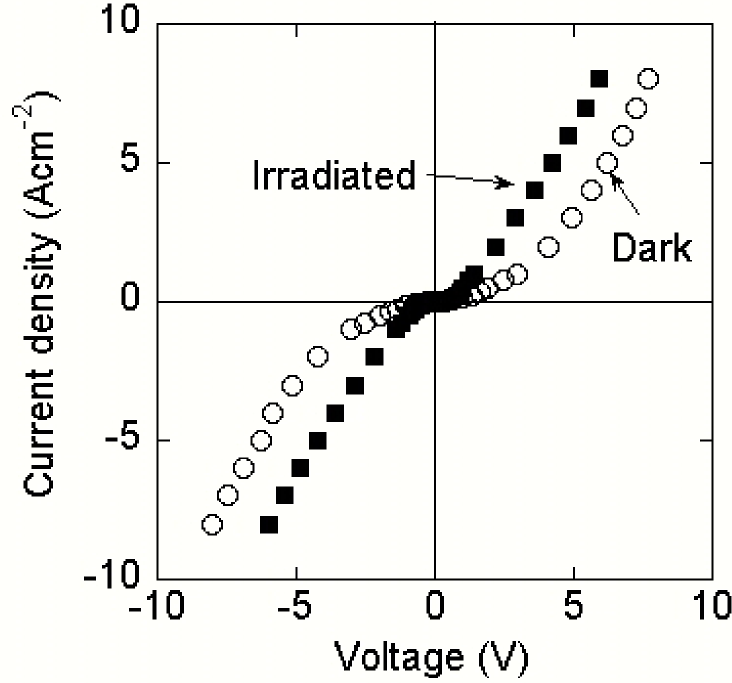

Figure 5.4: Comparison of the IV curve measured in the darkness (open circles) and under illumination (full squares) of the structure (GNS1382) excited with P=4.5mW at $\lambda = 325nm$.

by the reverse saturation current of a Schottky diode:

$$I_S = A_n^{\star} T^2 exp(-\frac{e\Phi_{bn}}{k_B T}) \tag{5.1}$$

For the given structure it should be in the order of $10^{-10} Acm^{-2}$ which is a deviation of eleven orders of magnitude lower than the experimental data. The strong deviation origins from the presence of defects in the structure which results in a high leakage current. Details of this mechanism and how it can be controlled are given in chapter 4.2. For a more quantitative analysis of the photo current the results of both measurements are subtracted and plotted in a semilogarithmic scale in Fig. 5.5. The effective photo current shows also a symmetric behaviour as function of the bias voltage. An interesting point is the saturation effect at a current of $2Acm^{-2}$. This saturation starts at a bias voltage of about 1.4V and it is limited due to the power of the light source. A further increase of the bias does not increase the photocurrent. This value is not comparable to the built-in potential of 0.5V. The further increase of the current at bias voltages above the built-in potential seems to be caused by the generation of electron-hole pairs in the metal contacts.
From the measured current and the known excitation power, a very rough calculation of the efficiency of the diode could be done.
The current of $2Acm^{-2}$ is equal to a carrier flow of $1.3 * 10^{16} s^{-1}$ and the excitation power

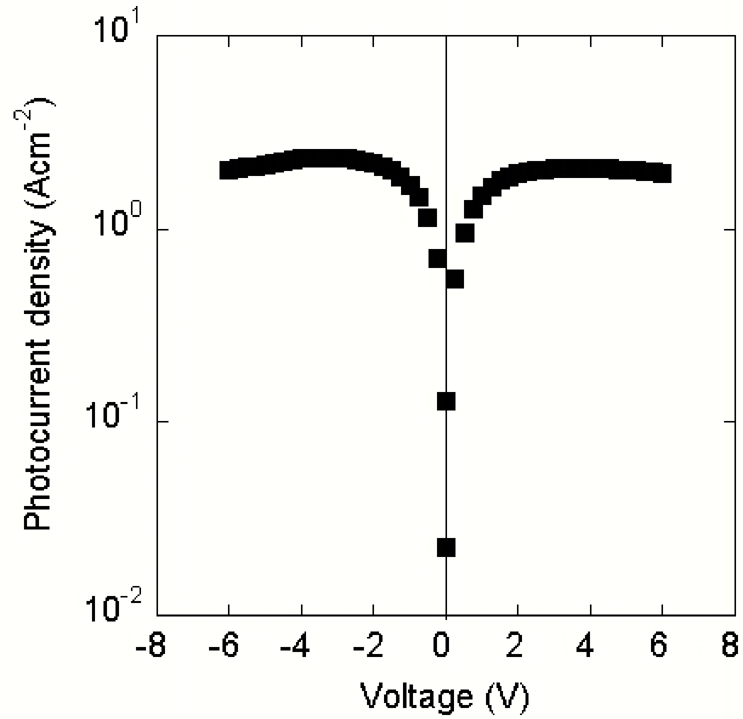

Figure 5.5: Effective photo current of the MSM structure measured at T=300K.

of 4.5mW from which 80% are coupled into the semiconductor due to the difference in the refractive indices are equal to $7.4 * 10^{15} s^{-1}$ of photons. Assuming that each photon generates one elctron-hole pair and both carrier types have the same amount on the photocurrent, the efficiency is nearly 100%. Thus the saturation of the photocurrent can be explained by the excitation of all carriers.

6 AlGaN/GaN based field effect transistors

6.1 Structure and band diagram

Transistor structures are the most important devices in modern computer and telecommunication systems. Typical bipolar transistors (npn) were used since their developement in 1947 by Bardeen et. al. . This transistors use the 3-dimensional mobility of both carrier types (electrons and holes) for the operation. Therefore their operation speed is limited by the carrier type, which has the lower mobility. Today they are more and more replaced by field effect (FET) transistors like a metal-insulator-semiconductor FET (MISFET) or metal-oxide-semiconductor FET (MOSFET). One of the advantage of the FETs is firstly, that they are unipolar devices. They use only one type of carrier for current transport, especially electrons due to their higher mobility. At second their current channel can easily be controlled by a gate bias and their realization is easier. In the channel a 3DEG or 2DEG is located. A disadvantage is that the operation speed suffers from the scattering of the electrons at surface defects of the semiconductor or at their ionzed donor states. An improvent of the FETs are the modulation doped FET (MODFET) or heterojunction field effect transistor (HFET), also called high electron mobility FET (HFET or HEMT). These structures use in genaral the mobility of a 2DEG, but it is shifted from the surface to the interface of a heterojunction, which prevents the scattering at the surface defects. But the most important feature is, that modulation doping allows the spatial separation of carriers and impurities, so that impurity scattering do not occur(see chapter 2.3.3). This results in much higher operation speed in comparison to all other transistors.
The basic feature of a HFET consists of a simple AlGaN/GaN heterostructure, in which the 2DEG is located at the AlGaN/GaN interface. In order to get a high performance of the device the two materials have to join perfectly in an ideal heterostructure. It is quiet difficult to realize this, but heterostructures offer the opportunity to manipulate their behaviour of carriers through bandgap engineering [71].
In general it means to control the band offsets of both materials at the heterointerface. In case of group-III nitrides the band offsets can be changed by the variation of the Al mole fraction in the AlGaN barrier. The total bandgap of $Al_xGa_{1-x}N$ is given by the linear interpolation of the c-GaN and c-AlN gap [72]:

$$E_{g,AlGaN} = (3.2 + 1.85x)[eV] \tag{6.1}$$

The band offsets of the conduction and valence band are calculated using an empirical equation which sets 65% of the total bandgap discontinuity to the conduction band and

35% to the valence band [50].
The operation of an HFET depends mainly on free carrier transport parallel to the heterojunction. The obvious way of introducing carriers, used in classical devices, is to dope the regions where the electrons or holes are desired. Unfortunately, charged donors or acceptors are left behind when electrons or holes are released, and scatter the carriers through their Coulomb interaction (ionized impurity scattering). The solution for the appearing problem is the remote or modulation doping, where the doping is grown in one region but the carriers subsequently migrate to another. In connection with the conduction band discontinuity two things occur: First the electrons from the modulation doped layer are trapped into a roughly triangular potential well, and prevents the electric field from returning the electrons to their donors. The dimension of the well is typically less than 10nm, and the levels for motion along the growth direction are quantized in a way similar to those in a square well. With propriate doping only the lowest level is occupied and all electrons are free in motion parallel to the interface. This is the two-dimensional electron gas and the basis for the majority of electronic devices in heterostructures. The separation of carriers and impurites allows higher mobility due to the reduction of scattering mechanism. For device operation the density of a 2DEG can be controlled, as in a MOSFET, applying a gate voltage by a Schottky contact. Adding ohmic source and drain contacts completes the FET. This is called a modulation doped FET (MODFET) or HEMT.
A simple structure for a high-speed device based on c-AlGaN/GaN is shown in Fig.

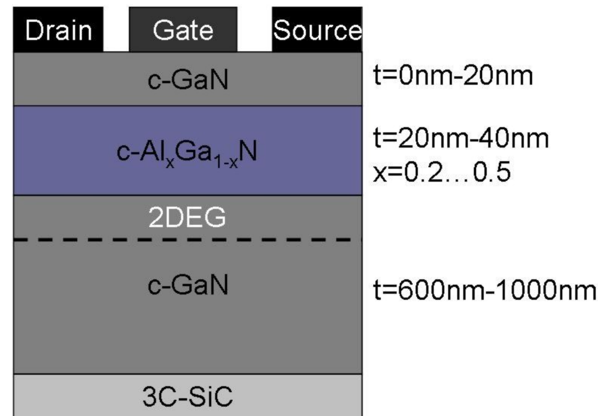

Figure 6.1: Schematic drawing of a AlGaN/GaN based HEMT device.

6.1. The structure is typically grown on freestanding 3C-SiC at a substrate temperature of T=720°C. A GaN buffer layer reduces the defect density and prevents the drift of carriers to the conducting substrate [73]. The thickness is typically in the order of 600nm-1000nm. The heterointerface is formed by depositing an AlGaN film with a thickness of 20nm-40nm on top of the GaN. The thickness of the barrier is choosen in

that way, that the residual doping level prevents parallel conductivity in the barrier. The Al mole fraction is varied between x=0.2 and 0.5 to study the dependence of the behaviour of the 2DEG on the shallow doping concentration and the depth of the potential well. The structure is capped by an GaN layer with a thickness between 0nm and 20nm in order to guarantee the formation of a Schottky barrier on the low doped GaN. No intentional doping is used in our structures. The unintentional doping levels are $n = 1 * 10^{17} cm^{-3}$ for the GaN and $n = 2 * 10^{18} cm^{-3}$ for the $Al_xGa_{1-x}N$ (see chapter 3.3). The gate contact is realized by thermal evaporation of Ni (see also chapter 4) and the source and drain consists of pure In (chapter 4)[6].

Considering a junction between n^+-AlGaN (material A) and n-GaN (material B), the

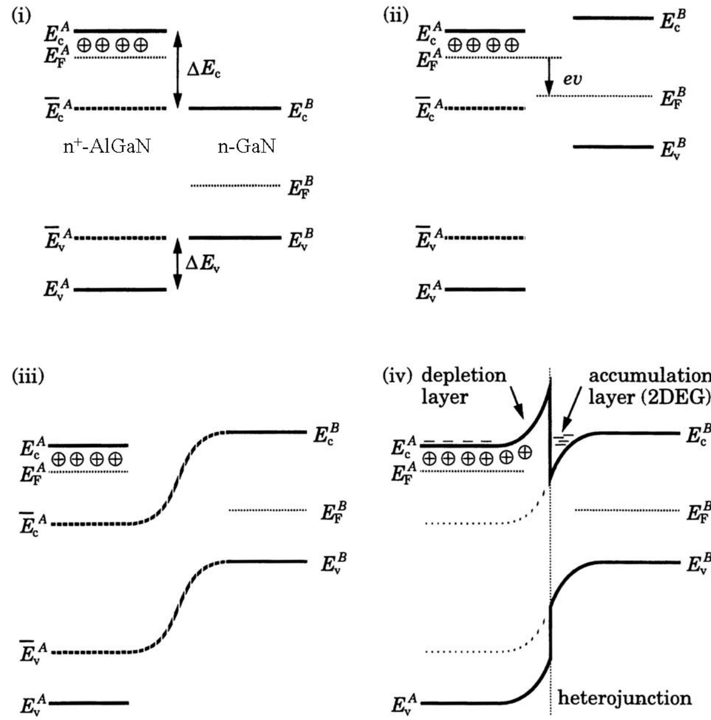

Figure 6.2: Steps in the construction of the band diagram for a doped AlGaN and GaN heterojunction.

Fig. 6.2 illustrates the principle for sketching the band diagram. An accurate treatment requires a self-consistent solution of Poisson equation for the electrostatic potential and Schrödinger equation for the wave function and the quantized states, with the Fermi-Dirac distribution describing the occupation of the levels.

- Starting with flat bands in each material, with the band in their natural alignment and the Fermi levels set by the doping on each side. This gives the position of the Fermi level far from the junction. To cancel out the effect of the discontinuities

temporarily, we draw lines on side A at $\bar{E}_C^A = E_C^A - \Delta E_C$ and $\bar{E}_V^A = E_V^A + \Delta E_V$. Note that $\bar{E}_C^A - \bar{E}_V^A = E_C^B - E_V^B$, so that the effective band gap is the same on both sides.

- The next step is the alignment of the Fermi levels. The difference far from the junction is set by any applied voltage. We assume that there is a positive bias V applied to side B, so that $E_F^A - E_F^B = eV$.
- Next one has to join $\bar{E}_C^A$ to E_C^B and $\bar{E}_V^A$ to E_V^B, with parallel curves due to the electrostatic potential, for a qualitative picture a S-shape curve whose curvature is set by the sign of the charge density is useful.
- At last E_C^A on side A as a line at $\bar{E}_C^A + \Delta E_C$ and E_V^A at $\bar{E}_V^A - \Delta E_V$ is restored, including the discontinuities in E_C and E_V at the junction.

The recipe creates a very rough picture for the band diagram of an heterojunction. For detailed and quantitative analysis it is necessary to solve the Poisson and Schrödinger equation in a self consistent way.

The numerical solution of both equations are generated by a commercial reliable com-

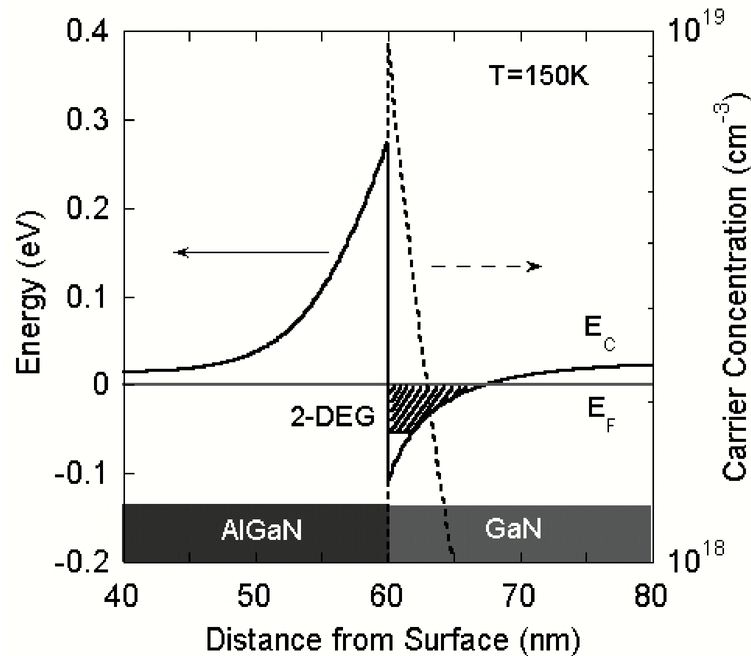

Figure 6.3: Band diagram of a AlGaN/GaN based HEMT device calculated with the 1D Poisson program for a temperature of 175K.

puter program called 1D-Poisson [74], which regards a set of material parameter like band gap energy, band offset, effective masses, doping,.... This program calculates the band diagram as well as the distribution of electrons and holes, the wave function and

also the energy level of the quantized states in the channel. Fig. 6.3 illustrates the result near the AlGaN/GaN interface calculated for the structure in Fig. 6.1 using a temperature of T=150K. This temperature of 150K is choosed in order to compare the calculation with experimental data. For the calculation the thicknesses given in the figure and the material constants given in chapter 2.1 are used. For the doping levels a value of $1 * 10^{17} cm^{-3}$ for the GaN and $2 * 10^{18} cm^{-3}$ for the AlGaN is assumed (see chapter 3.3). The Fermi level (grey line) is set to zero as a definition, the black solid line represents the curvature of the conduction band around the AlGaN/GaN interface in the depth of 60nm from the surface. A spike with a height of 300meV above E_F is formed on the AlGaN side. The channel at the GaN side is created by decreasing the band edge 110meV below the Fermi level for a depth between 60nm and 66nm. The band edge increases again above the Fermi level with a distance of a few meV for depths above 66nm. The distribution of the carrier concentration (dashed line) shows the opposite behaviour. Whenever the band edge increases, the carrier concentration decreases. The most remarkable point is the strong increase of the concentration at the position of the channel up to $1 * 10^{19} cm^{-3}$.
The possibility to calculate the properties of the heterostructures allows to design and optimize the structure prior to growth. The following diagrams illustrate the dependence of the 2DEG density and the parallel conductivity in the AlGaN barrier on the barrier height, doping concentration of the barrier and barrier thickness. For an optimized design the conductivity of the 2DEG is much higher than that of the AlGaN layer.

The Fig. 6.4 shows the calculated sheet carrier concentration of the 2DEG (circles) and

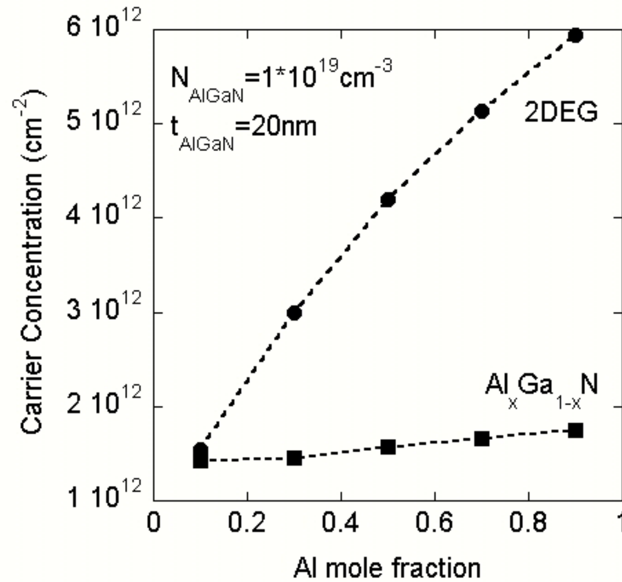

Figure 6.4: Sheet carrier concentration of the 2DEG and the residual carrier concentration of the AlGaN barrier as function of the Al mole fraction x for a temperature of 300K.

the residual sheet carrier concentration (squares) of the AlGaN barrier as function of the Al mole fraction x for a temperature of 300K. The barrier thickness is set to a value of t=20nm and the donor concentration in the AlGaN barrier is fixed at $N_D = 1*10^{19} cm^{-3}$. This value is above the typical background doping concentration of the AlGaN and simplifies the influence of the Al mole fraction on the carrier concentration (see chapter 3.3). For the GaN a constant background doping of $N_D = 1*10^{17} cm^{-3}$ is used. The Al mole fraction x is varied between 0 and 1. In case of x=0, we have a GaN/GaN structure, which can not form a 2DEG channel. For a AlN/GaN heterostructure the quantum confinement in the channel is so strong, that the energy of the ground state is above the Fermi level and therefore it is not occupied with carriers. If an Al content of x=0.1 is used, a flat channel with a sheet carrier density of $n_{2DEG} = 1.5*10^{12} cm^{-2}$ is formed, whereas the concentration in the barrier reaches nearly the same value with $N_{AlGaN} = 1.4*10^{12} cm^{-2}$. With increasing Al mole fraction the depth of the channel becomes deeper, and therefore the number of electrons in the channel increases linearly up to $n_{2DEG} = 6*10^{12} cm^{-2}$ for an Al content of x=0.9. On the other hand the residual concentration in the barrier is nearly independent on the Al content. A possible reason is the prevention of carrier diffusion into the channel due to the increasing electric field.

A further parameter which has a strong influence on the parallel conductivity in the

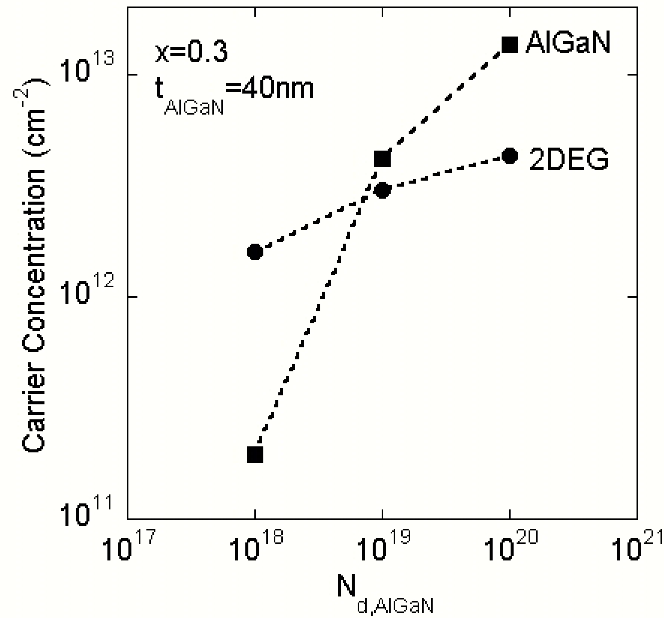

Figure 6.5: Sheet carrier concentration of the 2DEG and residual carrier concentration of the AlGaN barrier as a function of the AlGaN donor concentration for a temperature of 300K.

barrier, is the doping concentration of the barrier itself. Figure 6.5 shows the dependence of the carrier concentration in the channel (circles) and the barrier (squares) for a AlGaN doping level between $10^{18} cm^{-3}$ and $10^{20} cm^{-3}$. The other parameters are

set constant with x=0.3 for the Al content and t=40nm for the thickness of the barrier. In this case the density of the 2DEG increases from $n_{2DEG} = 1.5 * 10^{12} cm^{-2}$ to $n_{2DEG} = 4.3 * 10^{12} cm^{-2}$, but with a slope< 1. This is due to the maximum filling of the channel with carriers. It can be confirmed by the observation that the residual carrier concentration in the barrier increases more rapidly.

At last we want to study the influence of the variation of the barrier thickness on

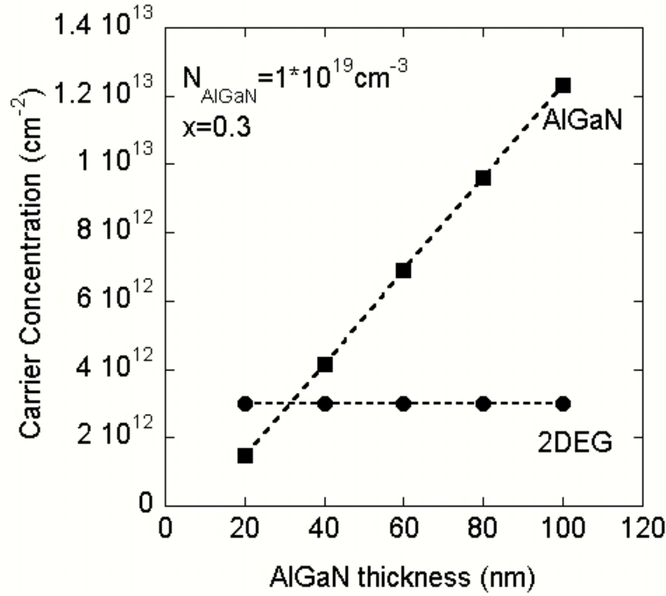

Figure 6.6: Sheet carrier concentration of the 2DEG and the residual carrier concentration of the AlGaN barrier as a function of the AlGaN barrier thickness for a temperature of 300K.

the parallel conductivity. The results are depicted in Fig. 6.6. For the calculation an AlGaN barrier with a mole fraction of x=0.3 and a doping of $N_D = 1 * 10^{19} cm^{-3}$ is used. The density of the 2DEG is independent on the barrier thickness and only determined by the complete filling of the channel, which is influenced by the Al content. However, the carrier concetration increases linear from $N_{AlGaN} = 3.6 * 10^{11} cm^{-2}$ to $N_{AlGaN} = 1.6 * 10^{13} cm^{-2}$ if the thickness is varied from 10nm to 100nm. The carrier concentration in the barrier is determined by the difference between the doping concentration and the number of carriers which diffuse into the channnel. Therefore at high thicknesses of the barrier the amount of diffused carriers is neglectable and the sheet carrier concentration is direct proportional to the thickness. Above a thickness of 50nm the carrier concentration in the barrier is significatly higher than in the channel.
In summary the optimal AlGaN/GaN heterostructure consists of an $Al_{0.3}Ga_{0.7}N$ layer with a thickness of t_{AlGaN}=20nm a doping of $N_{D,AlGaN} = 2 * 10^{18} cm^{-3}$.

6.2 Optical properties

Photoluminescence (PL) spectroscopy is a nondestroying and very sensitive methode to investigate the optical properties of semiconductor heterostructures. It offers the possibility to vary the temperature as well as the excitation intensity. Furthermore it can be used as a depth sensitive probe if the sample structure changes.
Due to the high absorption coefficient of $\alpha = 1.07 * 10^7 m^{-1}$ for the cubic group-III nitrides the penetration depth of our HeCd laser is about 300nm. If the thicknesses of the different layers are carefully adjusted, one can investigate the spatial origin of the optical transitions by performing PL measurements on different structures.
Therefore three different structures are grown and measured by PL at a temperature

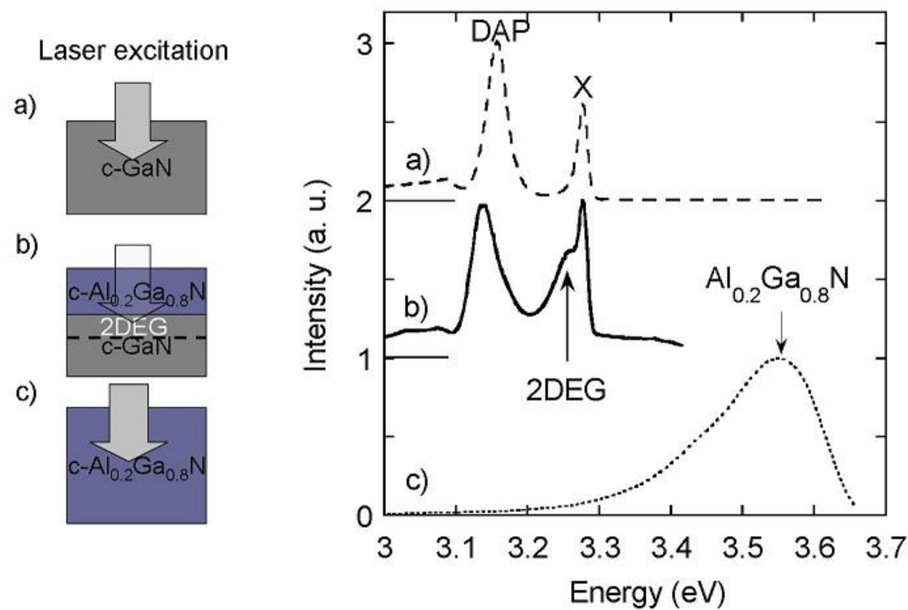

Figure 6.7: Photoluminescence spectra of different structures measured at T=2K. a) pure GaN-layer, b) $Al_{0.2}Ga_{0.8}N/GaN$ heterostructure, c) pure $Al_{0.2}Ga_{0.8}N$ layer.

of T=2K with an excitation power of $20Wcm^{-2}$. Figure 6.7 shows the structures of the samples on the left side. On the right side the corresponding PL spectra are plotted. The luminescence of the DAP is normalized to one and the spectra are linearly shifted for a better overview. Figure 6.7a exhibits schematically the penetration of the laser beam into a 1000nm thick unintentionally doped c-GaN layer. The corresponding PL spectrum shows the typical transitions of c-GaN [75]. The bound exciton transition at an energy of $E_X = 3.268eV$ and the donor acceptor pair recombination at $E_{DAP} = 3.134eV$ are clearly observed. In Fig. 6.7b the PL spectrum of an $Al_{0.2}Ga_{0.8}N/GaN$ heterostructure

with an AlGaN layer thickness of 100nm is shown. An important note is, that the AlGaN thickness is below the penetration depth of the laser. Therefore the two bulk c-GaN related transtions X and DAP are observed. However no AlGaN related transition is observed, which should be at $E_{AlGaN} = 3.570eV$. In this spectrum an additional peak at an energy of E=3.247eV is found. This belong neither to the bulk GaN comparing to Fig. 6.7a, nor to the AlGaN bulk material as shown in Fig. 6.7c. In Fig. 6.7c the excitation of an $Al_{0.2}Ga_{0.8}N$ layer with a thickness of 700nm (>>penetration depth) is drawn. The corresponding PL spectrum shows only a transition with an energy of E=3.552eV. Taking into account that $E_{g,AlGaN}$=3.2+1.85*x[eV] [72], the energy of the transition fits very well to the band gap of $Al_{0.2}Ga_{0.8}N$. In conclusion, an additional transition measured at 3.247eV that belongs to a 2DEG located at the interface between AlGaN and GaN.
In order to investigate the nature of the transition and to see if it could really origin from a 2DEG, the band diagram of the measured AlGaN/GaN heterostructure was calculated. The structure is similar to that drawn in Fig. 6.1. In detail two quantized states in the channel are formed, but only the first sub band is below the energy of the Fermi level. For the second one the energy is above the Fermi edge,and therefore unoccupied. The localization energy of the first subband is about 51meV, so that the transition energies of two possible transitions can be calculated as follows: For the optical transiton from the 2DEG state to the valence band $E_{2DEG} = E_{g,GaN} + E_{loc}$=3.302eV+0.051eV=3.353eV, and from the 2DEG state to the acceptor level its about $E_{2DEG} = E_{g,GaN} - E_A + E_{loc}$=3.302eV-0.110eV+0.051eV=3.243eV. These are the maximum and the minimum energy for the transition energy of the 2DEG. So the measured value of $E_{2DEG} = 3.247eV$ fits well to the calculated data. Transitions within this energy range are allowed. From the AlGaAs/GaAs system it is well known, that the so called H-band transition are not vertically in the k-space [76].
To confirm the attribution to the emission of an 2DEG, the dependence of the 2DEG on different parameters was investigated, like the depth of the channel (by the Al content x) or the background doping in the GaN, as well as the dependence on the temperature, excitation power or an electric field.
Figure 6.8 illustrates the influence of the Al content x of the barrier on the transition energy of the 2DEG measured at a temperature of T=2K with an excitation power of $20Wcm^{-2}$. The intensity of the excitonic transition is normalized to one and the spectra are shifted for a better overview. The excitonic transition of c-GaN was observed at an energy of $E_X = 3.268eV$ for each structure, as well as the donor-acceptor related transition located at E_{DAP}=3.134eV. This confirms the constant background doping in the GaN layer and excludes the influence of this parameter on the transition energy of the 2DEG. If the Al mole fraction is varied from x=0.25 (squares)(GANS1228), where the 2DEG transition is observed at an energy of E_{2DEG}=3.258eV, to x=0.30 (open circles)(GANS1239) the energy shifts downwards to E_{2DEG}=3.228eV. The shift of the 2DEG transition is 30meV, whereas the change in the band gap of AlGaN is about 92meV. The same behaviour is found for the increase of the Al content up to x=0.35 (full circles)(GANS1384). Here the transition energy changes

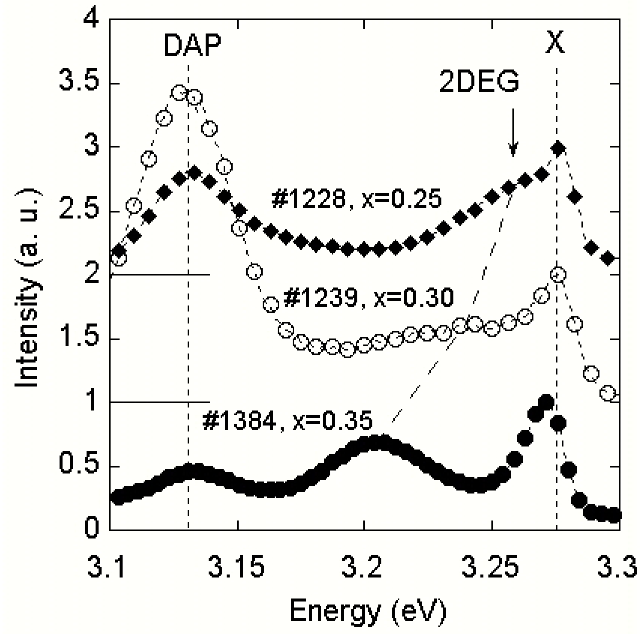

Figure 6.8: Photoluminescence spectra of $Al_xGa_{1-x}N/GaN$ heterostructures with Al mole fractions of 0.25, 0.30 and 0.35 measured at T=2K.

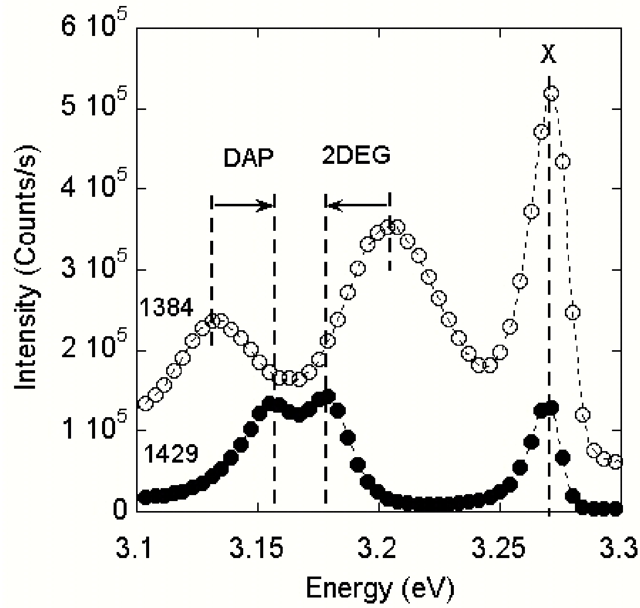

Figure 6.9: Photoluminescence spectra of $Al_{0.35}Ga_{0.65}N/GaN$ heterostructures with different background doping concentrations of $N_D = 1 * 10^{17} cm^{-3}$ (GANS1384) (open circles) and $N_D = 1 * 10^{18} cm^{-3}$(GNP1429) (full circles) measured at T=2K.

down to E_{2DEG}=3.200eV. The discrepancy occurs due to the quantum confinement of the electrons in the channel. If the depth of the channel is increased by 92meV, which should reduce the transition energy of the 2DEG in the same range, the ground state energy of the subband increases due to the increasing confinement. In summary the effective energy shift is smaller than the band edge variation. It is quite difficult to find a quantitative model for the dependence due to the indirect nature of the transition, and therefore it will not discussed here.
One of the important parameters is the background doping of c-GaN buffer. With running time the efficiency of the chemical purifiers degradates and the background doping increases due to the increasing contamination with oxygen (see chapter 4.2). Figure 6.9 shows the photoluminescence of two samples consisting of an $Al_{0.35}Ga_{0.65}N/GaN$ heterostructure. The excitonic transition from the c-GaN buffer at E=3.268eV can be as well observed as the donator acceptor pair recombination at 3.132eV for the low doped sample GANS1384 (open circles) and E=3.157eV for the higher doped GNP1429 (full circles). From the structural similarity of both samples one can conclude, that the measured shift of the DAP transition is due to the change in the background doping level. This shift is equal to a change in the unintentionally doping concentration from $n = 10^{17}cm^{-3}$ (GANS1384)(open circles) to $10^{18}cm^{-3}$ (GNP1429)(full circles). The effect of this higher doping level on the transition energies of the H-band (2DEG) is a shift to lower energies. For the low doped sample the transition is located at E_{2DEG}=3.204eV whereas for the higher doped one a energy of E_{2DEG}=3.178eV is measured. The shift of the 2DEG transition due to the change of the band bending at the AlGaN/GaN heterointerface. Figure 6.10 illustrates the principle. For a low doping level the difference

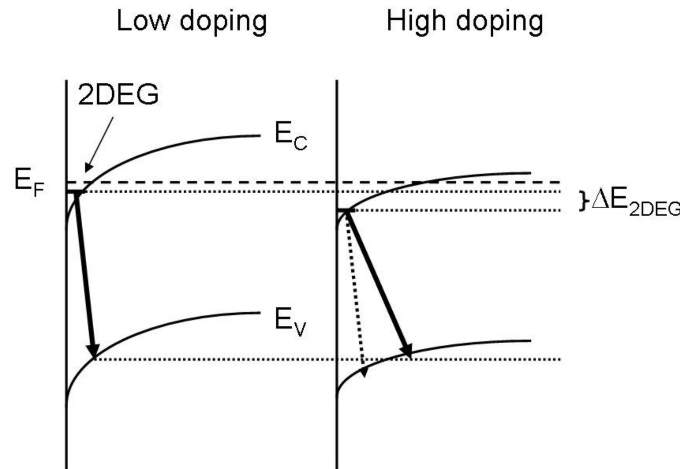

Figure 6.10: Principle of the change in the band bending at the heterointerface due to the change in the c-GaN background doping

between the conduction band E_C and the Fermi level E_F is relatively huge. This results

in a strong bending of the GaN conduction band at the interface and in a high ground state energy of the 2DEG level as shown in the left side of Fig. 6.10. If the doping level increases, the distance between E_C and E_F decreases. This leads to a reduction in the bending of the conduction band of GaN and a wider potential well with a lower ground state energy. This reduces in total the transition energy of the 2DEG.

Next the temperature and intensity dependence of the 2DEG transition is studied. The

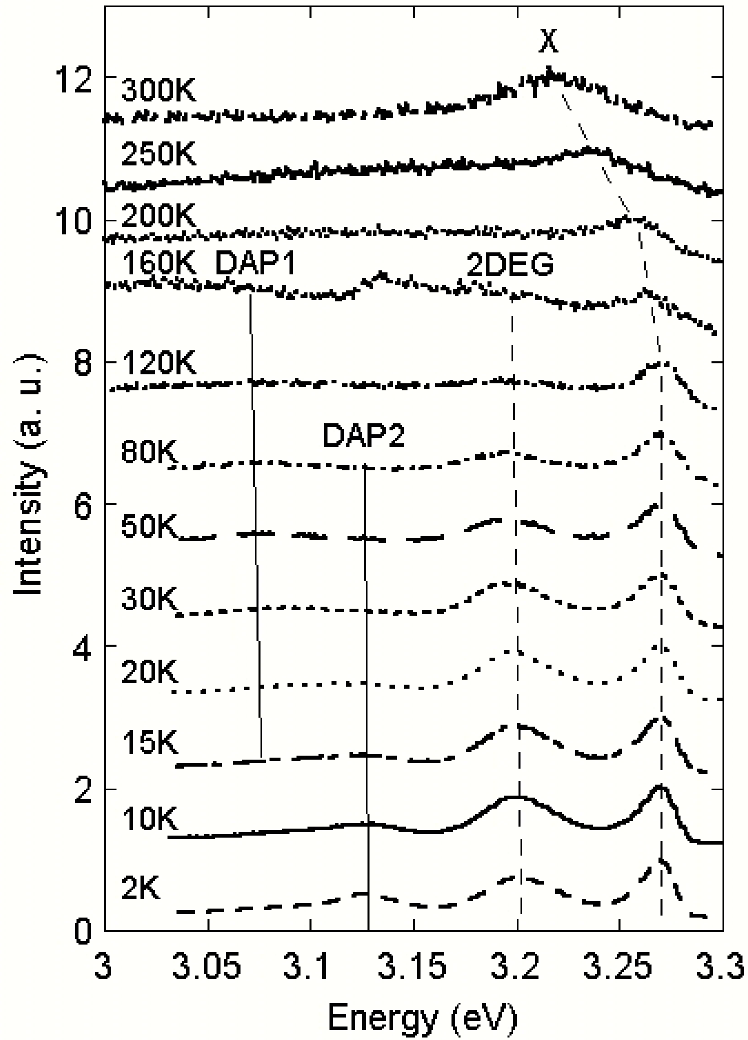

Figure 6.11: PL spectra of a $Al_{0.35}Ga_{0.65}N/GaN$ heterostructure (GANS1384) measured at different temperatures between 2K and 300K.

variation of temperature allows the determination of the activation energies of the levels which cause the transitions. For the analysis the temperature is varied between 2K and 300K using an excitation power of P=$20Wcm^{-2}$. Figure 6.11 shows the PL spectra of a $Al_{0.35}Ga_{0.65}N/GaN$ heterostructure (GANS1384) measured at different temperatures between 2K and 300K. The excitonic transition is normalized to one and the spectra

are shifted linearly for a better overview. The dotted line represent the measurement done at T=2K. Here one can clearly observe two DAP and X transitions as well as the 2DEG related one. The DAP1 transition is located at an energy of 3.076eV and the DAP2 at 3.127eV. With increasing temperature a suppression of the DAP2 is observed at a temperature of 80K due to the thermalization of the level, the DAP1 transition with the lower energy indicating a higher ionization energy shows the thermalization at temperatures of 200K. Additionally a suppression of the DAP2 and 2DEG intensity is found in comparision to the X transition, which is a hint for a thermalisation of these levels. But the reduction in intensity of the DAP2 and 2DEG continious. At room temperature only the X transition of GaN is observed.
The energy positions of the exciton, donor-acceptor-pair recombination and the 2DEG transition of a $Al_{0.35}Ga_{0.65}N/GaN$ heterostructure (GANS1384) are depicted in Fig. 6.12 for temperatures between 2K and 300K. The solid line describes the behaviour of

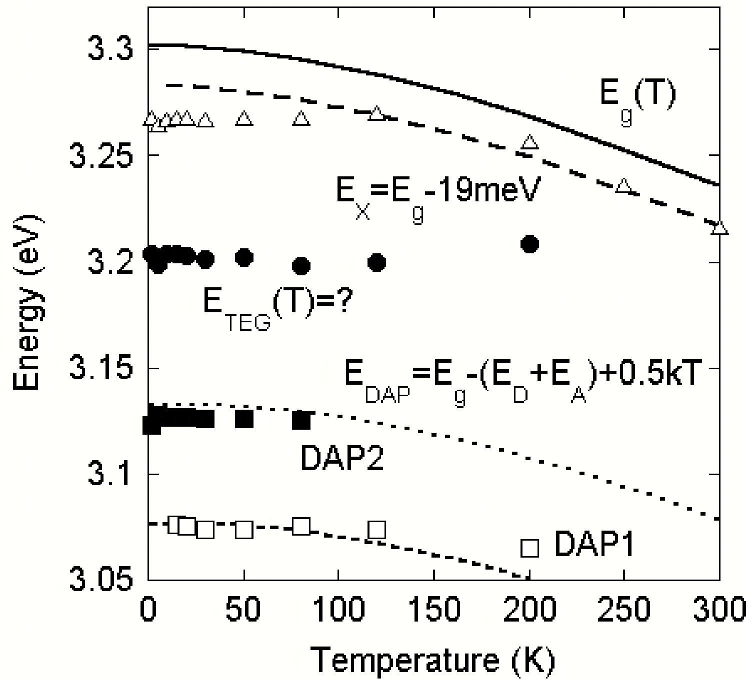

Figure 6.12: The peak position of the X, DAP1, DAP2 and the 2DEG correlated transition for temperatures between 2K and 300K for a $Al_{0.35}Ga_{0.65}N/GaN$ heterostructure (GANS1384).

the band gap energy as function of temperature using the equation of Varshni et al. [77]

$$E_g(T) = E_g(0) - \frac{\alpha T^2}{T + \beta} \tag{6.2}$$

where $E_g(0)$=3.302eV , $\alpha = 6.697 * 10^{-4} eVK^{-1}$ and β=600K. The dashed line is the gap energy minus the exciton binding energy of 19meV [18]. The behaviour of the DAP2

recombination is given by the difference of the gap energy and total activation energy of the donor and the acceptor. For the donor a value of 55meV (O_2) [49] and for the acceptor 110meV [18] was used. A temperature dependence of 0.5kT is added. The DAP1 transition is described by a donor activation energy of 20meV [18] and a acceptor energy of 210meV. The excitonic transition (full squares) shows a temperature independent transition energy up to 120K due to a strong localisation, may be related to an impurity. At values above 120K the position follows very well the gap like behaviour. In contradiction to the band gap energy, the 2DEG transition (open squares) shows no shift in the observed temperature range. This is influenced by two effects which act in a contradictional way. On the one hand the energy is lowered by the lowering of the GaN band gap and on the other hand the transition energy is increased due to the change of the Fermi level and the occupation of higher states with increasing temperature. The two DAP transition, which were observed in the spectra show both a bandgap-like behaviour. They have their origin in the incorporation of oxygen (DAP2) and carbon (DAP1). The presence of the carbon related transition is may caused by memory effect of carbon. An

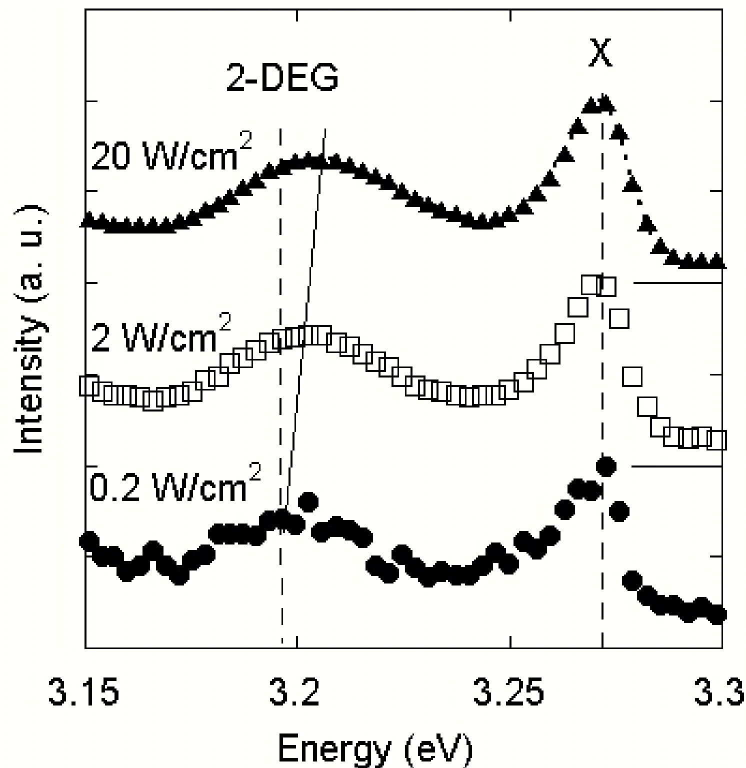

Figure 6.13: The normalized PL intensity of the X, DAP and the 2DEG correlated transition for excitation power between $0.2Wcm^{-2}$ and $20Wcm^{-2}$ of a $Al_{0.35}Ga_{0.65}N/GaN$ heterostructure (GANS1384).

additional hint for the existence of a 2DEG is the shift of the transition energy using different excitation power [76]. In Fig. 6.13 different PL spectra are plotted in the energy

range from 3.15eV to 3.3eV for the $Al_{0.35}Ga_{0.65}N/GaN$ heterostructure GANS1384. The excitation power of the laser is varied between $0.2Wcm^{-2}$ and $20Wcm^{-2}$ by inserting UV-neutral density filters into the excitation beam. The temperature is set to T=2K. The spectra are normalized to one and they are linearly shifted for a better overview. With increasing excitation power the 2DEG transition shows a clear blue shift, whereas the energy of the X transition is independent on the power. Fig. 6.14 depicts the energy

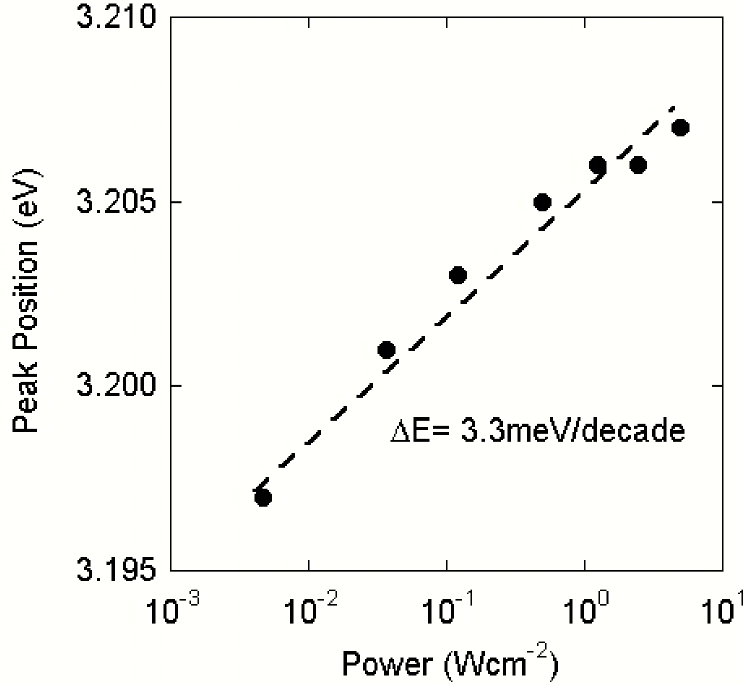

Figure 6.14: The peak position energy of the 2DEG related transition for excitation power between $0.2Wcm^{-2}$ and $20Wcm^{-2}$ for GANS1384

position of the 2DEG transition vs. the excitation power in the range from $0.2Wcm^{-2}$ to $20Wcm^{-2}$. A logarithmic increase of the peak position with increasing excitation power from a value of 3.197eV at a power of $0.2Wcm^{-2}$ to 3.207eV at $20Wcm^{-2}$ is observed. A logarithimic fit reveals a shift of 3.3meV/decade. This effect is attributed to the recombination of electrons trapped in the potential notch next to the interface caused by the band-bending with free holes in the valence band at some distance away from the heterointerface. The power dependence of the emission energy is explained as a result of photoexcited carrier screening of the built-in heterointerface field. This screening drives the band structure flat band and causes a blue-shift of the emission energy, which is proportional to the logarithm of the excitation power [76].
A direct experimental proof of this assignment to an H-band like transition is obtained by applying a weak electric field parallel to the growth direction. Such experiments were performed by applying an electric field parallel to the growth direction via a semitransparent Ni-Schottky contact at a temperature of T=2K. On top of a $Al_{0.27}Ga_{0.73}N/GaN$ heterostructure (GANS1228) layer a Ni contact with a thickness of 4.5nm is deposited,

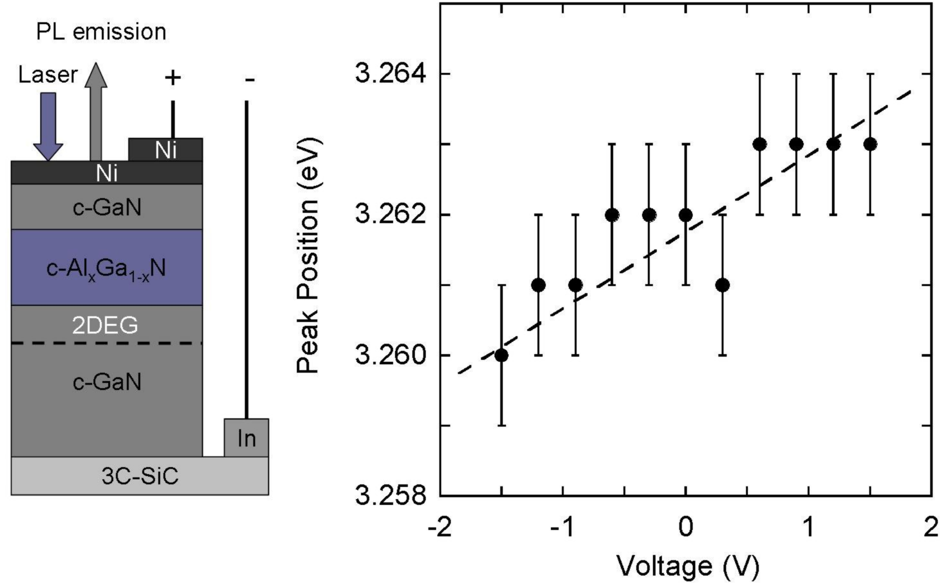

Figure 6.15: The peak position energy of the 2DEG related transition for applied voltages between -1.5V and +1.5V for GANS1228

using a contact size of 4x4mm^2. The thickness allows, that 70% of the laser light are coupled into the layer and 70% of generated luminescence is transmitted. In comparision to an ungated structure we loose $70\% * 70\% = 50\%$ of intensity. The contact size allows the lateral adjustment of the laser beam on the sample surface on a useful position. The Fig. 6.15 shows the energy position of the 2DEG as function of the applied electric field. The solid line in the figure is a guide for the eye. A clear blue shift in the energy position of 4 meV is observed by changing the bias voltage from -1.5V to 1.5V. The shift of the transition energy can be explained by the variation of the band structure due to different applied external voltages. The shape and the depth of the potential well will change, which results in a shift of the quantization energy of the 2DEG.

6.3 Electrical properties

The determination of the electrical properties is the main issue in the investigation of electronic devices. This chapter will focus on the electrical properties of our AlGaN/GaN heterostructures grown on free-standing 3C-SiC and on carbonized Si wafer. A scematic sketch of the samples, which were characterized, is drawn in Fig. 6.16. On top of a 3C-SiC layer a 1000nm thick c-GaN layer is deposited, followed by $c - Al_{0.35}Ga_{0.65}N$ layer with a thickness of 40nm. The structure is capped by GaN film using different thicknesses ranging from 0nm to 20nm. For the whole structure no intentional doping is used, resulting in a doping level of the GaN of about n=$1 * 10^{17} cm^{-3}$ and of the AlGaN n=$2 * 10^{18} cm^{-3}$, respectively. In order to apply an electric field, pure In is used as the

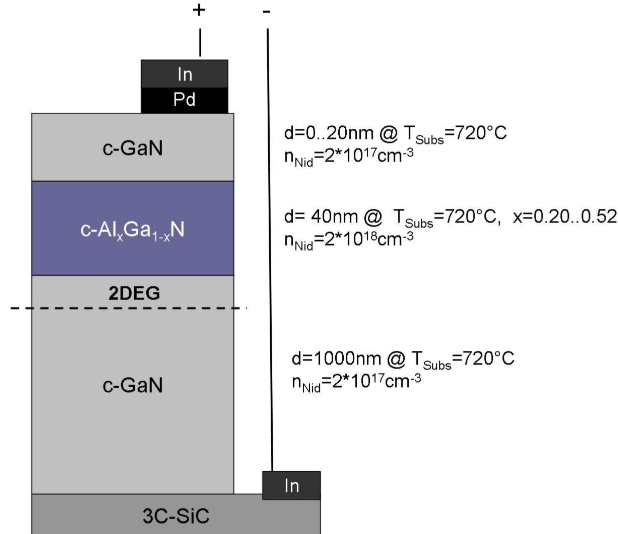

Figure 6.16: Schematic drawing of the AlGaN/GaN heterostructure.

ohmic contact on top of the SiC layer, fixed by micro soldering. The Schottky contact is realized by Ni/In contact with a diameter of $300\mu m$, consisting of a 50nm thick Ni layer and a 150nm thick In film.
A tip prober from Süss Microtech, Model PM5 is used for contacting the samples in order to perform I-V and C-V analysis at room temperature.

6.3.1 I-V and C-V analysis

Figure 6.17 shows the I-V curves for the $Al_{0.35}Ga_{0.65}N/GaN$ heterostructures with different cap layer thickness of 5nm (GANS1356)(triangles), 10nm (GANS1357)(squares) and 20nm (GANS1352)(circles). The samples are grown on carbonized Si substrates [79]. The measurements are performed at room temperature in the voltage range from -3V to +3V. Only for the sample GANS1352 with the cap thickness of 20nm we observe a nonlinear I-V curve. The curve indicates a barrier height of 1eV, which is nearly 0.3eV higher in comparison with pure GaN on freestanding SiC. This may be related to the higher band gap of the AlGaN layer, which forms a higher barrier. The samples with the thinner GaN cap layer reveal a linear dependence between the voltage and the current. This dependence can be explained by the surface RMS roughness. In Fig. 6.18 a scematic sketch of the interface region between the AlGaN and the GaN cap layer and the Pd Schottky contact is drawn. If the cap layer thickness is larger than the surface roughness, the highly doped AlGaN is fully covered by the GaN and the Pd covers the whole GaN surface. This results in a nonlinear I-V curve, comparable to the results on thick GaN (see chapter 4). But if the cap layer thickness is below the RMS roughness, there are still some areas of AlGaN, which are not covered by GaN, and for that the Pd is deposited directly on the AlGaN. The doping concentration of the AlGaN favours

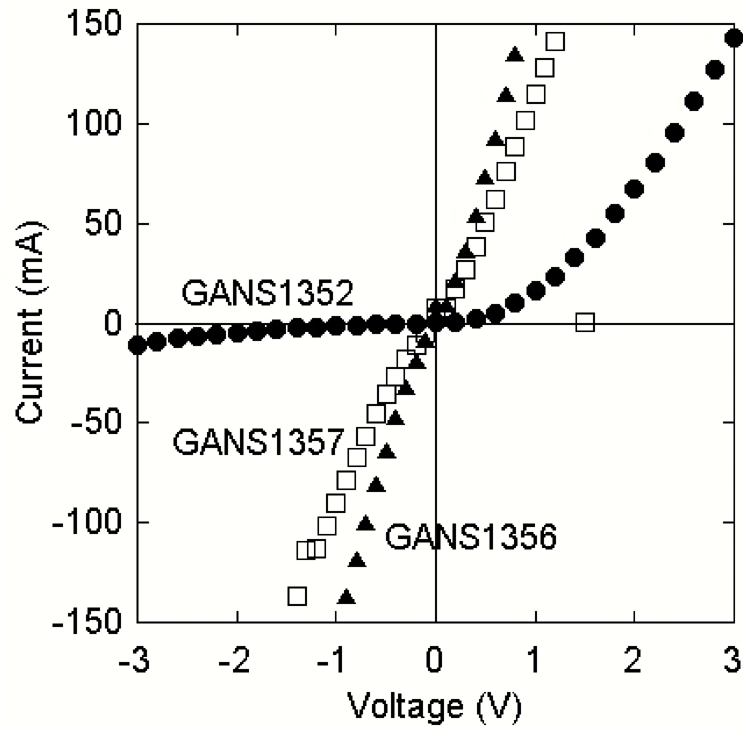

Figure 6.17: Current-Voltage characteristic of $Al_{0.35}Ga_{0.65}N/GaN$ heterostructures with different GaN cap layer thickness of 5nm (GANS1356)(triangles), 10nm (GANS1357)(squares) and 20nm (GANS1352)(circles).

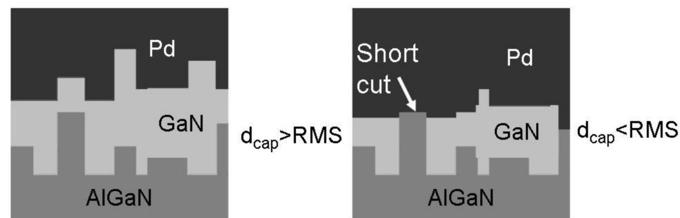

Figure 6.18: Influence of the RMS roughness on the electrical behaviour of heterostructures with different cap layer thicknesses.

the formation of a Schottky contact with a very thin barrier, which can be tunneled at nearly 0V, comparable to an ohmic contact. In case of this series of samples the doping in the AlGaN may slightly higher than in the case of the AlGaN/GaN Schottky diodes described in chapter 4.1. So the semiconductor is maybe degenrated, when the doping concentration is above the effective density of states. The AlGaN/GaN Schottky diodes are directly grown after the renewing of the nitrogen purifiers, whereas the structures with the cap layers are realized nearly one year later, equal to a degradation in the purifier efficiency.

A very simple method to investigate the doping concentration as function of the dis-

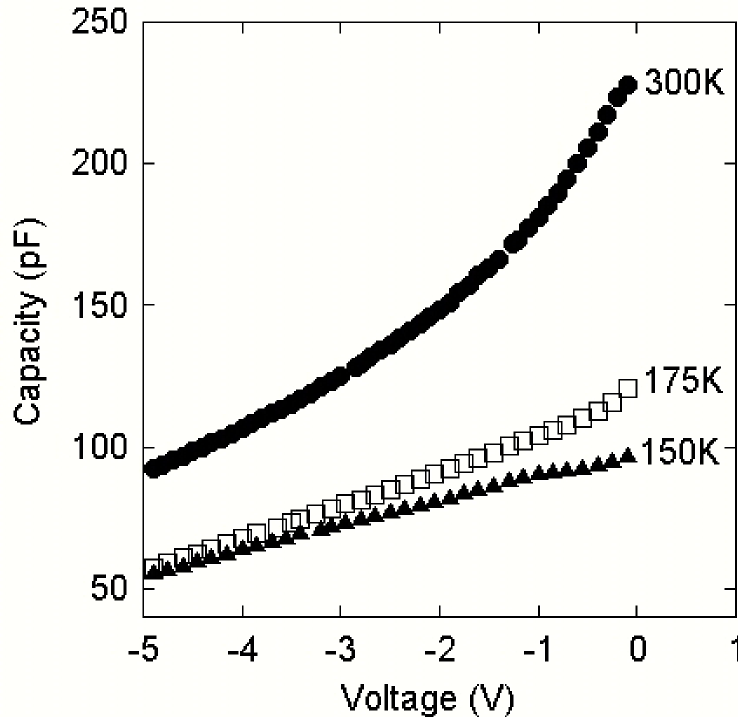

Figure 6.19: Capacity-Voltage characteristics of the $Al_{0.35}Ga_{0.65}N/GaN$ heterostructure (GANS1352) at temperatures of 300K, 175K and 150K.

tance from surface of Schottky diodes is the measurement of the capacitance voltage (C-V) dependence. In Fig. 6.19 the C-V characteristics of GANS1352 is plotted for different temperatures of 300K (circles), 175K (squares) and 150K (triangles). For the measurement at 300K the curve shows a three-dimensional dependence on the voltage, i. e. a parabolic shape with a decrease in the capacitance from 230pF at 0V to 90pF at -5V. For the lower temperature of 175K the behaviour changes dramatically. The capacitance decreases to 120pF at 0V and the slope is smaller than for room temperature. If the temperature is decreased again to a value of 150K, the change continues. Between a bias voltage 0V and -1V the capacitance is nearly constant at 95pF. Below -1V the capacitance decreases again with a linear curve shape to a value of 55pF at a voltage of -5V. The change in the slope of the capacitance at this temperature is a hint for a

change in the carrier concentration at a certain distance from the surface [78]. In order to investigate the carrier profile, the following assumptions are used:
The consideration of the depletion zone as a condensator with the size of the contact area and the distance as the depletion width allows the determination of the doping level versus the depth from the surface using the following relations:
The noncompensated impurity concentration can be calculated from:

$$N_D - N_A = \frac{-2}{e\epsilon A^2 \frac{d(1/C^2)}{dV}} \tag{6.3}$$

were A is the area of the contact and ϵ the dielectric constant of the semiconductor. The distance from the surface is derived by:

$$x = \frac{\epsilon A}{C} \tag{6.4}$$

where x is equal to the distance from the surface. From semiconductor theory it is known with respect to charge neutrality condition, that the width of the depletion zones in the different doped layer are inverse proportional to the doping level. So the total depletion zone is nearly equal to depletion zone in the semiconductor. Using both equations the

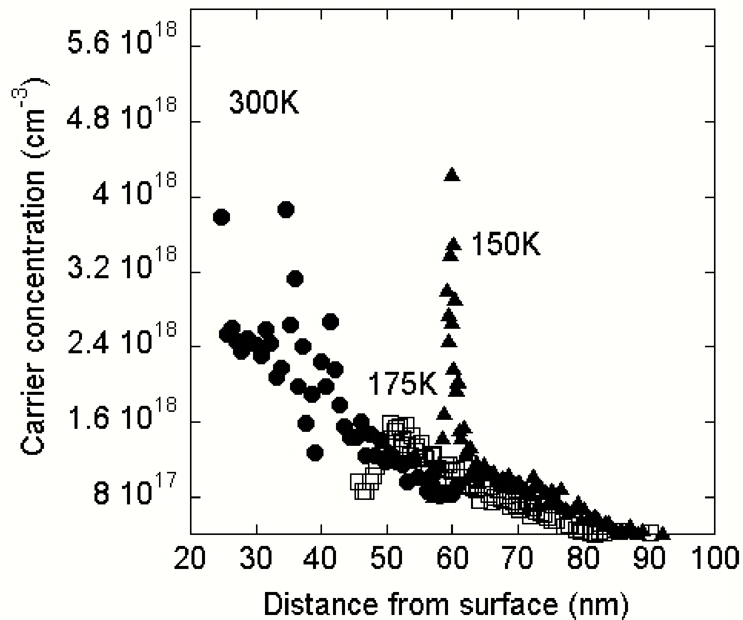

Figure 6.20: Carrier concentration profile of the $Al_{0.35}Ga_{0.65}N/GaN$ heterostructure (GANS1352) at temperatures of 300K (circles), 175K (squares) and 150K (triangles).

noncompensated donor profil is calculated and plotted in Fig. 6.20 for temperatures between 300K and 150K. As one can see in the figure, the concentration profile at room

temperature (circles) is nearly a constant value between $2.4 * 10^{18} cm^{-3}$ and $8 * 10^{17} cm^{-3}$ for a distance from the surface between 20nm and 60nm. The increase of the concentration in direction to the surface is may due to the presence of surface donor states in the AlGaN layer (see also chapter 4.2). At lower temperature of 175K (squares) the total concentration decreases to $1.4 * 10^{18} cm^{-3}$ due to the freeze out of free carriers at the impurities in the bulk layer of AlGaN and GaN. If the temperature is lowered again to 150K (triangles) a dramatical change in the profile occurs. The profile shows a maximum concentration of $4.8 * 10^{18} cm^{-3}$ at a distance from the surface of 60nm, whereas the concentration in the other regions between 65nm and 90nm is about $8 * 10^{17} cm^{-3}$ and also for a depth less than 57nm. The shift in the position of the maximum of the carrier concentration for 175K and 150K is caused by influence of the leakage resistance on the capacitance measurement (see chapter 2.3.3). In Fig. 6.21 the comparison of

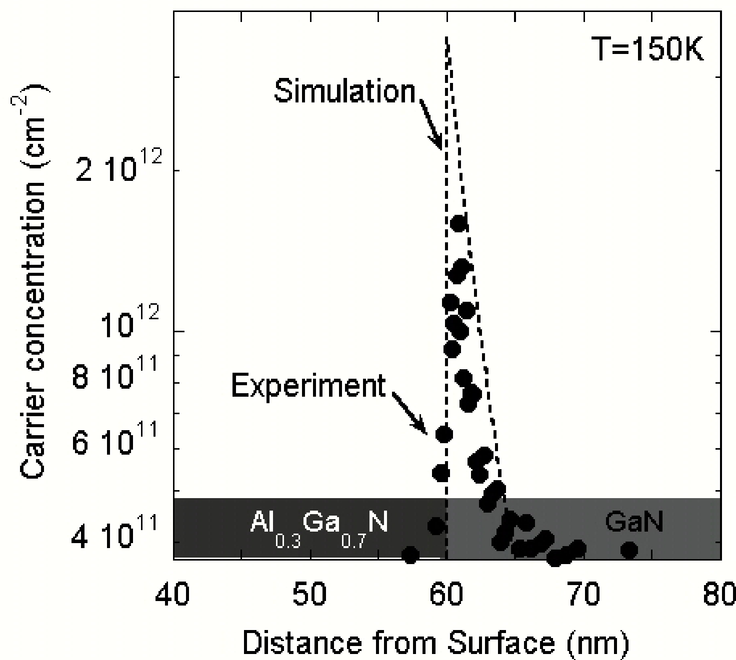

Figure 6.21: Experimental (full circles) and simulated (dotted line) carrier concentration vs. the distance from the surface. The experimental data were calculated from a CV measurement done at 150 K.

the simulated carrier profile (dashed line) in terms of the sheet carrier concentration of the sample with the experimental data (circles) from Fig. 6.20 for a temperature of 150K is plotted. The simulated profile shows a maximum sheet carrier concentration of $3.5 * 10^{12} cm^{-2}$ at a depth of 60nm which is correlated at the position of the AlGaN/GaN interface and the formation of a two dimensional electron gas. The experimental data, which we got from Fig. 6.20, reveal a sheet carrier concentration of $1.6 * 10^{12} cm^{-2}$. The value of the concentration is estimated from the width of the electron distribution and the peak electron concentration.

6.3.2 Hall effect analysis

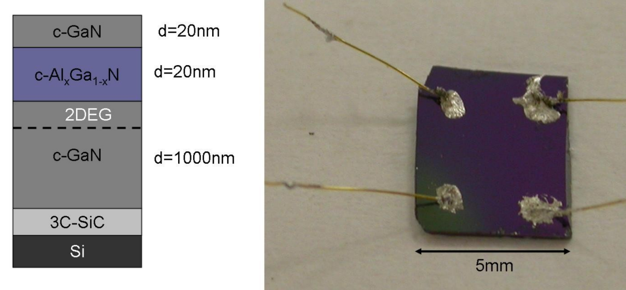

Figure 6.22: Structure and photograph of the AlGaN/GaN heterostructure which is used for the Hall-effect analysis.

Due to the conducting nature of the freestanding 3C-SiC substrates it is not possible to perform Hall-effect measurements on these sample, because the parallel conductivity in the substrate is in the same order of magnitude than the conductivity of the 2DEG. In order to avoid this problem, some carbonized Si wafers from the University of Ilmenau were used for the growth. They consist of a $395\mu m$ thick semiinsulating Si wafer with a 3nm thick 3C-SiC layer on top of it [79]. On this substrate a AlGaN/GaN heterostructure with a GaN buffer thickness of 1000nm is deposited followed by a 20nm thick $Al_{0.35}Ga_{0.65}N$ film and capped with a GaN layer of 20nm. For Hall-effect analysis the sample is cleaved into a piece of $5x5mm^2$ and In metal is used as the ohmic contact realized by microsoldering in van-der-Pauw geometry. A schematic drawing of the structure and a photograph of the sample is shown in Fig. 6.22. The sample is mounted into the cryostat and Hall effect measurements are performed in the temperature range from 10K to 300K. The results of the analysis are plotted in Fig. 6.23. The left side of Figure 6.23 shows the electron concentration of the $Al_{0.35}Ga_{0.65}N$/GaN (GANS1416) heterostructure as function of the temperature in the range from 10K to 300K measured for the total sample thickness of 1040nm. On the one hand the dependence of the carrier concentration looks like that for a bulk layer, because we observed a decrease from n=$1 * 10^{19}cm^{-3}$ at room temperature to n=$1 * 10^{17}cm^{-3}$ at 10K. A detailed analysis of the experimental data show, that the calculated concentration is above the effective density of states $N_C = 9.6 * 10^{17}cm^{-3}$. So semiconductor is degenerated and has no temperature dependence of the carrier concentration. With respect to this contradiction, the free carrier concentration is the sum of carriers in the thin 3C-SiC layer, the GaN buffer, the AlGaN and the 2DEG at room temperature. With decreasing temperature the 3D related carriers freeze out and at a temperature of 10K only the carriers of the 2DEG can be observed. The measured concentration of n=$1 * 10^{17}cm^{-3}$ at T=10K for a

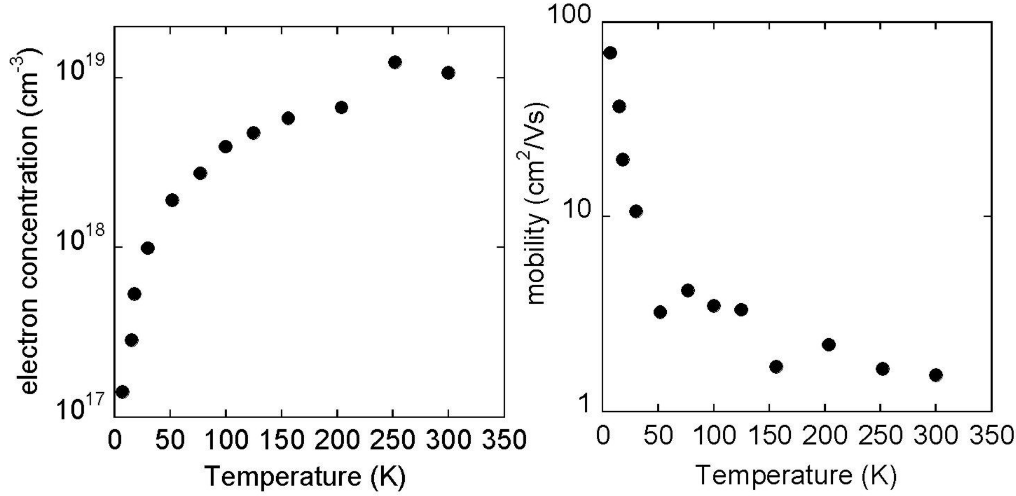

Figure 6.23: Electron concentration and mobility of a $Al_{0.35}Ga_{0.65}N$/GaN heterostructure for various temperatures between 10K and 300K.

thickness of 1040nm can be converted to a carrier concentration of $N_{2D} = 1 * 10^{13} cm^{-2}$ in the 2DEG channel using $N_{2D} = n_{3D} * L$, in with L is the width of the channel.
The evidence for the 2DEG in the structure is confirmed by the calculation of the mobility as function of temperature, like it is plotted in the right side of Fig. 6.23. A very low mobility in the order of $\mu = 1cm^2(Vs)^{-1}$ is observed for temperatures above 50K. If the temperature is decreased, an increase of the mobility up to $\mu = 70cm^2(Vs)^{-1}$ is found. This temperature dependence is typical for a 2DEG system in which a spatial separation between impurities and carriers is present, but nevertheless the value is rather low.

6.3.3 Theoretical description of carrier scattering

In order to find an explanation for the result, the influence of scattering on the motion of carriers in a two-dimensional channel has to be discussed. The most reasonable scattering mechanism in the group-III nitrides are acoustic phonon scattering, impurity scattering, dislocation and interface roughness scattering [80], [81].
The mobility μ of carriers in a semiconductor is calculated as

$$\mu = \frac{e}{m^*}\tau_{tot} \qquad (6.5)$$

where m^* is the effective mass of the electrons and τ_{tot} represents the total momentum relaxation time, given by:

$$\frac{1}{\tau_{tot}} = \sum \frac{1}{\tau_i} \qquad \text{(Matthiessen rule)} \qquad (6.6)$$

where τ_i are the relaxation times for the different processes, which can occur in a semiconductor. In contrast to a bulk semiconductor the scattering processes in 2DEG system are quite different. The relaxation time in this case is the superposition of the relaxation due to optical and acoustical phonon scattering and impurity scattering, which strongly depend on the temperature, as well as scattering by alloy disorder (proportional to the carrier density) and dislocation and interface roughness scattering. The relaxation time τ_i is given by

$$\tau_i = \frac{\hbar}{2\pi| < k_i|H_i|k_f > |^2 \delta(k_i - k_f)} \tag{6.7}$$

where H_i describes the Hamiltionian for the scattering process. From equation (4.42) one can see, that the process with the smallest relaxation time dominates the total relaxation time and the mobility. If an adequate description is found for the Hamiltonian of each scattering process, one can calculate the mobility limited by each process.
The first scattering mechanism is the influence of acoustic phonons on the mobility. Phonons can be described by a periodic pertubation of the semiconductor lattice. This is done in an approximation of a harmonic oszillator, the Hamiltonian is given by:

$$|H_{ap}| = |\frac{a_c e A_l}{V}| \int \text{Bloch} \quad \text{function} \quad dr^3 \tag{6.8}$$

in which a_c is the deformation potential of the conduction band and A_l the amplitude of the harmonic oscillator which is equal to the change in the position of the conduction band relative to the unperturbated crystal, and which is influenced by the absorption or emission of a accoustic phonon. A_l is given by

$$A_l = (\frac{N\hbar}{2M\omega_l})^{0.5}(\text{emission}) \text{ and } A_l = (\frac{(N+1)\hbar}{2M\omega_l})^{0.5} \text{ (absorption)} \tag{6.9}$$

describing the emission and absorption of a phonon. Due to the fact, that a crystal consists of many oscillators the number N can be approximated by the average number of phonons at a certain temperature T with respect to the Planck statistics. After some transformations of the equation we can calculate the relaxation time of accoustic phonons:

$$\frac{1}{\tau_{ap}} = \frac{3a_c^2(m^* k_B T)^{3/2}}{2\sqrt{2\pi}\hbar^4 c_{11}} \tag{6.10}$$

The equation shows that the mobility depends only on the temperature and is independent on the sheet carrier concentration of the 2DEG. The Fig. 6.24 shows the mobility limited by acoustic phonon scattering as function of the temperature in the range from 1K to 300K. As one can see in the figure, the mobility is limited by phonon scattering to $\mu = 4 * 10^6 cm^2(Vs)^{-1}$ at room temperature and exhibits a strong increase by orders of magnitude to $\mu = 6 * 10^8 cm^2(Vs)^{-1}$ at T=10K.
The next parameter, which can have an influence on the carrier mobility, is the scattering at ionized impurities. Especially in the case of our GaN, which has a relativly high impurity level of $N_D = 1 * 10^{17} cm^{-3}$, a strong influence is expected. Assuming a

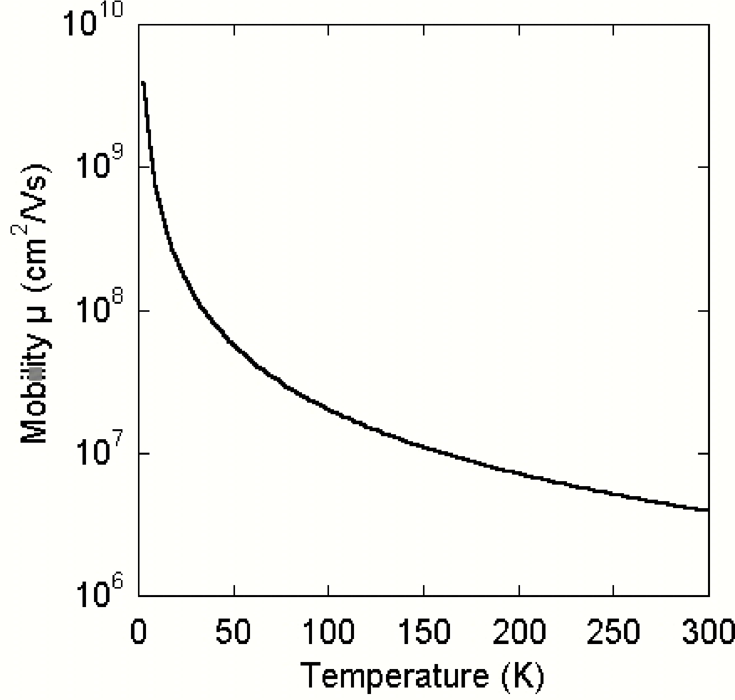

Figure 6.24: Electron mobility limited by acoustic phonon scattering for various temperatures between 1K and 300K.

high degenerated electron gas and a constant background density N_{ii} of impurities the relaxation time τ_{ii} is given by:

$$\frac{1}{\tau_{ii}} = \frac{N_{ii} m^*}{2\pi\hbar^3 k_F^3}(\frac{e^2}{2\epsilon}) \tag{6.11}$$

where $k_F = \sqrt{2\pi N_{2D}}$. Details of the calculation are presented in Ref. [71]. The results are plotted in Fig. 6.25 for impurity densities between $N_{ii} = 7 * 10^{16} cm^{-3}$ and $N_{ii} = 7 * 10^{17} cm^{-3}$ at a temperature of T=10K. We see, that the mobility increases proportional to $N_{2D}^{3/2}$ for a constant impurity level. In case of our typical background of $N_{ii} = 1 * 10^{17} cm^{-3}$ the mobility increases from $\mu = 4 * 10^4 cm^2 (Vs)^{-1}$ for $N_{2D} = 1 * 10^{12} cm^{-2}$ to $\mu = 1 * 10^6 cm^2 (Vs)^{-1}$ for $N_{2D} = 1 * 10^{13} cm^{-2}$. These values are three orders of magnitudes higher than the experimental data. So it is clear, that the mobility in our case is not limited by scattering at ionized impurities.

A further parameter, which can be important in our heterostructures, is the dislocation density. Due to the high misfit between the substrate and the layer, the typical dislocation density in 3C-SiC/GaN is about $1 * 10^9 cm^{-2}$(calculated from the FHWM of the rocking curve). The basic idea for calculation is the screening of a perfect 2DEG by an additional electrostatic potential, which refers to the dislocations. The dislocations can be modeled by a line of charge, like described in Ref. [82]. The Hamiltionian H_{Dis} can

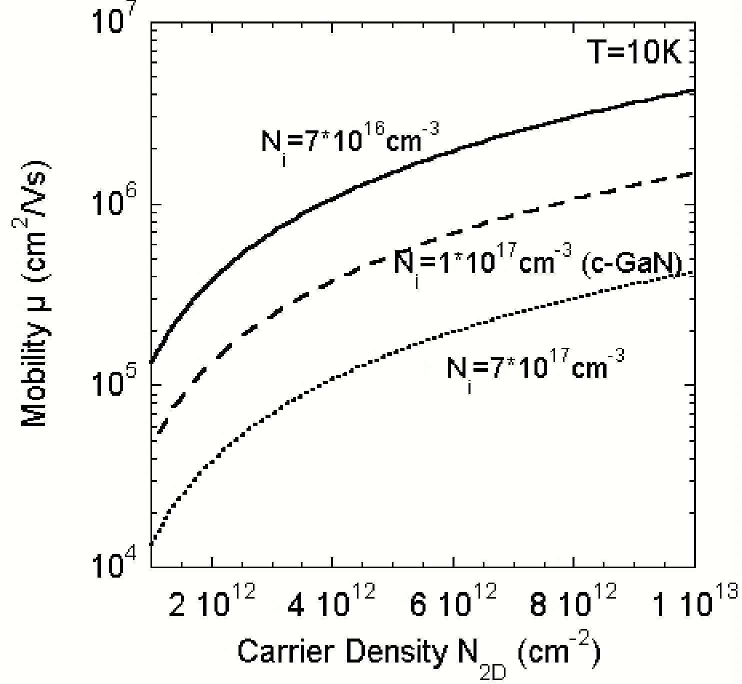

Figure 6.25: Electron mobility limited by impurity scattering for a temperature of T=10K.

be calulated and the relaxation time τ_{Dis} is equal to [83]:

$$\frac{1}{\tau_{Dis}} = \frac{\hbar^3 \epsilon^2 a_0^2}{N_{Dis} m^* e^4 f^2} \frac{16\pi k_F^4}{\frac{1.84 k_F}{q_{sc}} - 0.25} \tag{6.12}$$

where N_{Dis} is the dislocation density, f is the fraction of filled states in the charged dislocation. It can be extracted from the minimization of the free energy per dislocation line in the case of 60 dislocations after Weimann et al. [84] and depends on the concentration of carriers in the channel. In our case a value of f=0.84 is a resonable approximation, which leads to a carrier concentration of $n = 10^{19} cm^{-3}$ in the channel. a_0 refers to the in plane lattice parameter of GaN and describes the minimal spacing of two charged lines. k_F is the Fermi vektor given by $\sqrt{2\pi N_{2D}}$, where N_{2D} is the sheet carrier concentration. q_{SC} is the screening length, which is determined from $\frac{2}{a_B^*}$, where $a_B^* = 1.18 * 10^{-9} m$ is the effective Bohr radius. The results are plotted in Fig. 6.26, which shows the electron mobility of a 2DEG as function of the sheet carrier density for dislocation densities between $10^9 cm^{-2}$ and $10^{11} cm^{-2}$. The mobility increases with the carrier density at a constant dislocation density by a factor of 7, when the carrier density increases from $N_{2D} = 1 * 10^{12} cm^{-2}$ to $N_{2D} = 1 * 10^{13} cm^{-2}$. The curve shows a dependence which is roughly proportional to $N_{2D}^{3/2}$. For a dislocation density of $10^{10} cm^{-2}$ we expect a mobility between 10^4 and $7 * 10^4 cm^2 (Vs)^{-1}$ for a carrier density between $10^{12} cm^{-2}$ and $10^{13} cm^{-2}$. If the dislocation density is reduced by one order of magnitude,

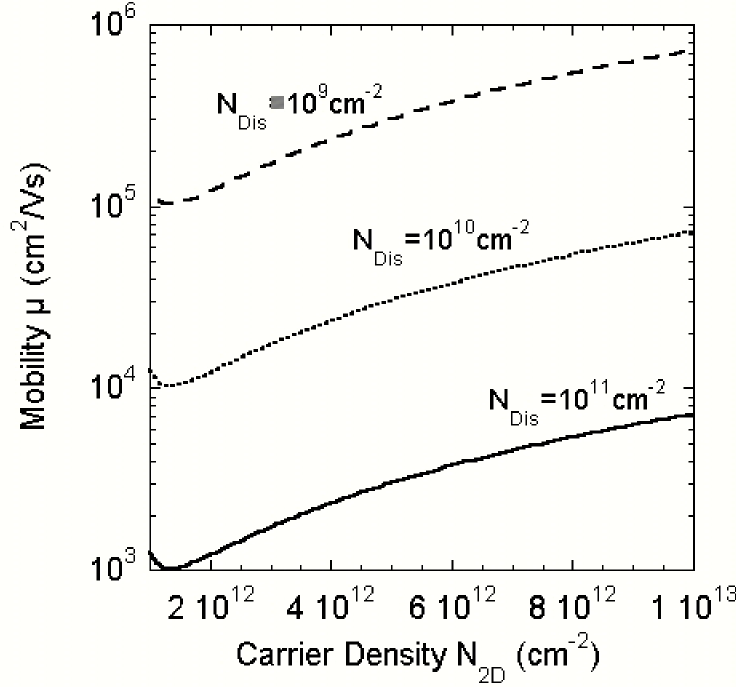

Figure 6.26: Electron mobility limited by dislocation scattering for various carrier densities in the channel in the range of $N_{2D} = 10^{12} cm^{-2}$ to $N_{2D} = 10^{13} cm^{-2}$.

the mobility increases by a factor of 10 due to the inverse proportional dependence in equation 4.48. The range between a dislocation of $10^9 cm^{-2}$ and $10^{10} cm^{-2}$ represents the values, which are state of the art for cubic GaN on freestanding 3C-SiC (lower density) and on carbonized Si (higher density). If the results are compared with hexagonal based structures it was found, that in the cubic regime the theoretical mobility at the same defect density is one order of magnitude higher than in the h-based samples due to lower effective masses and higher coherence length. Therefore, scattering at dislocations is also not the limiting parameter for mobility in our heterostructures. At the end the influence of the interface roughness is discussed. The roughness can be described by randomized position variation of the walls of a squared infinite quantum well. This results in a transformation of the coordinates for the well in z-direction and in an additional potential in the Schrödinger equation. The additional potential refers to intersubband and also to intrasubband transitions, which will be only consider in these calculations. In the end the relaxation time for roughness scattering is determined by [85]:

$$\frac{1}{\tau_{RMS}} = \frac{2\phi^3 \Lambda^2 E_1}{\hbar L^4} D^2 I(\Lambda k_F, \frac{k_F}{q_{sc}}) \tag{6.13}$$

Λ is the coherence length of the interface fluctuations and can be approximated by half of the terrace width of GaN (experimentally measured by quantitative RHEED analysis, see chapter 3.1), the value is about Λ=2.5nm. E_1 is the energy of the first

subband. The length L represents the width of well, in our case about 5nm. The factor D describes the interface roughness, approximated by the surface roughness measured by AFM. $I(\Lambda k_F, \frac{k_F}{q_{sc}})$ is an integral, which represents the influence of the roughness in combination with the coherence length and depends also on the Fermi vektor k_F. This integral can be expressed by the following equation:

$$I(\Lambda k_F, \frac{k_F}{q_{sc}}) = \frac{1}{2\pi} \int \frac{(1 - cos\frac{\Theta}{2})}{(1 + \frac{q_{sc}}{2k_F} sin\frac{\Theta}{2})^2} exp(-\Lambda^2 k_F^2 sin^2 \frac{\Theta}{2}) d\Theta \tag{6.14}$$

This integral is numerically calculated for different k_F, representing a sheet carrier concentration between $10^{12}cm^{-2}$ and $10^{13}cm^{-2}$ and fitted by a polynom of the fifth order. The value of the integral is given by:

$$I(\Lambda k_F, \frac{k_F}{q_{sc}}) = 0.102 + 9.34 * 10^{-14} N_{2D} - 2.79 * 10^{-26} N_{2D}^2 \tag{6.15}$$

$$+4.06 * 10^{-39} N_{2D}^3 - 2.95 * 10^{-52} N_{2D}^4 + 8.54 * 10^{-66} N_{2D}^5$$

The mobility is calculated for carrier densities between $10^{12}cm^{-2}$ and $10^{13}cm^{-2}$ and for interface roughnesses ranging from 1nm to 8nm. The value of 8nm is a reasonable value for GaN grown on carbonized Si on a $100x100\mu m^2$ scan range. The scan range is comparable to the free path length of the scattered electrons. The results are plotted in Fig. 6.27. The plot shows that the mobility is nearly independent of the carrier density and only influenced by the RMS roughness. If the roughness is reduced by one order of magnitude, the mobility increases by a factor of 100 due to the squared dependence. For example at a RMS roughness of 8nm (standard samples) the mobility will be expect in the range of $80cm^2(Vs)^{-1}$ and for the best value (3nm) we get $600cm^2(Vs)^{-1}$.
After the investigation of the different scattering mechanism and their influence on the mobility in the channel it is very helpful for future work to compare them. The comparison of impurity, dislocation and roughness scattering together with the experimental data (GANS1416) shows clearly, like depicted in Fig. 6.28, that impurities and dislocations are not the limiting parameter for mobility in our heterostructures. The scattering mechanism, which causes the lowest values for the mobility, is the interface roughness. The results are in the range of$80cm^2(Vs)^{-1}$, and two orders of magnitude lower, than for dislocations or impurities. In comparison with the experimental data of GANS1416, an excellent agreement is observed, if the measured RMS roughness of 8.5nm is take into account. In addition we get the information, that the RMS roughness has to be reduced below 1nm in order to reach the mobility limit due to dislocation scattering for a dislocation density of $10^{10}cm^{-2}$.

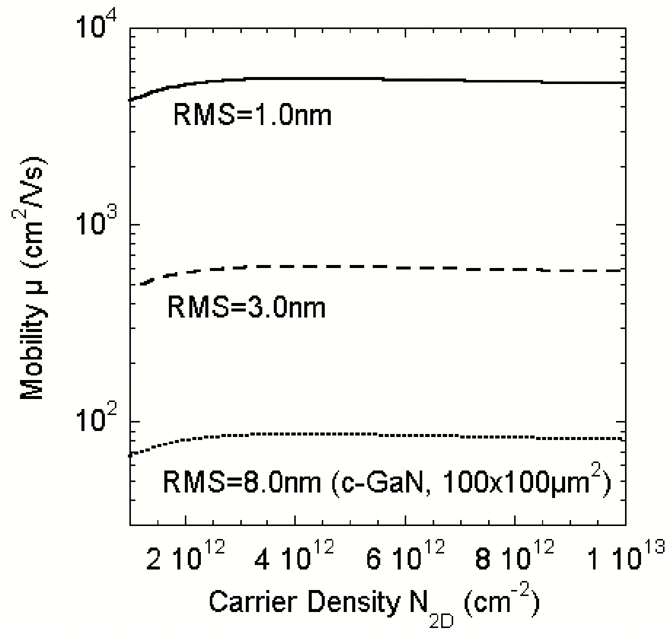

Figure 6.27: Electron mobility limited by roughness scattering for various carrier densities in the channel in the range of $N_{2D} = 10^{12} cm^{-2}$ to $N_{2D} = 10^{13} cm^{-2}$

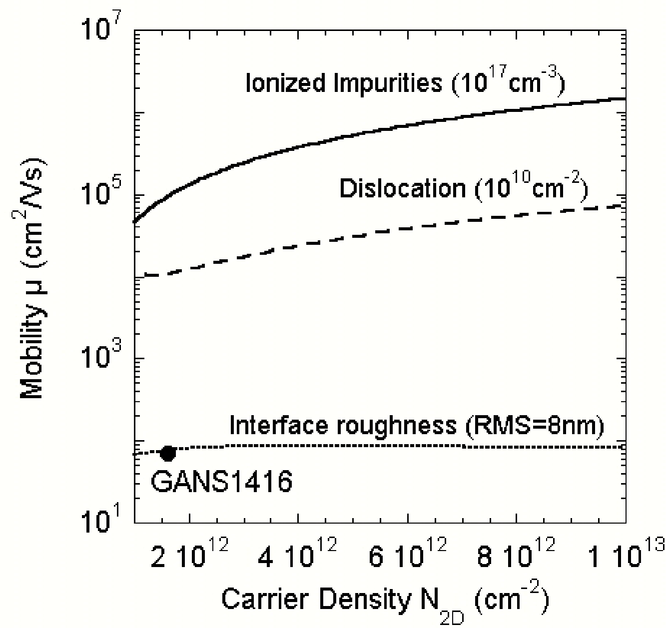

Figure 6.28: Electron mobility limited by different scattering mechanism for various carrier densities in the channel in the range of $N_{2D} = 10^{12} cm^{-2}$ to $N_{2D} = 10^{13} cm^{-2}$ and the comparison to experimental result

6.3.4 Fabrication and electrical characterization of HFET structures

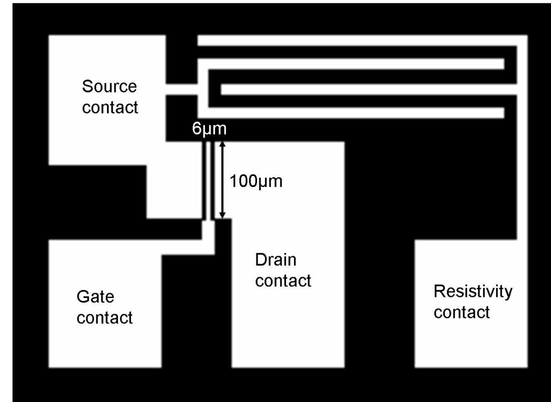

Figure 6.29: Arrangement of the source, drain and gate contact for our FET structures with a gate length of $6\mu m$ and a gate width of $100\mu m$ using Ref. [73].

Nevertheless some FETs were fabricated on Mesa structures and measure them at T=155K. Therefore the structural arrangement for the FET contacts was choosed using Ref. [73]. The structure, which is drawn in Fig. 6.29, consists of a source contact with a size of $70\mu m$x$100\mu m$ and a drain contact with a size of $170\mu m$x$100\mu m$. The separation of both contacts is $18\mu m$. The gate contact is placed in the center of the source and drain contact with a gate length of $6\mu m$ and a gate width of $100\mu m$. Additionaly the source is connected with a finger structure, with a finger length of $380\mu m$, a width of $30\mu m$ and a separation of $15\mu m$. The finger structure is completed by second finger structure connected with a further contact, having the same dimensions. The finger structure allows the determination of the insulation resistance of the structure as well as the insulation between different structures.
For the fabrication of the FET structures three steps are necessary. Therefore three types of masks are needed. Figure 6.30 illustrates the different masks. Figure 6.30a shows the Mesa structures in an arrangement of 3x3 Mesa. The size of one is $575\mu m$x$865\mu m$ with a separation of two different structures of $40\mu m$. The Mesa are $50\mu m$ wider than the source-drain contact mask, in order to ensure that the source-drain contact structure fits to the Mesa, even if the etching step produces flat edges between the Mesa and the groove. The 3x3 arrangement guarantees, that the mask fits to our 5x5mm^2 samples, which is normally used in our photolithography process. The mask is completed with a description for each column (A, B, C) and each row (1, 2, 3) in order to identify the FET on the sample. In Fig. 6.30b a picture of the mask for the source-drain contacts is drawn. They are also arranged in 3x3 structures together with the finger structure for the resistivity measurements. The Fig. 6.30c shows the mask for the gate contacts. All three masks are transfered by optical lithography to a glass substrate, which is covered with a 120nm thick Ni layer and with $2.3\mu m$ of a positive photo resist (AR-P3510).

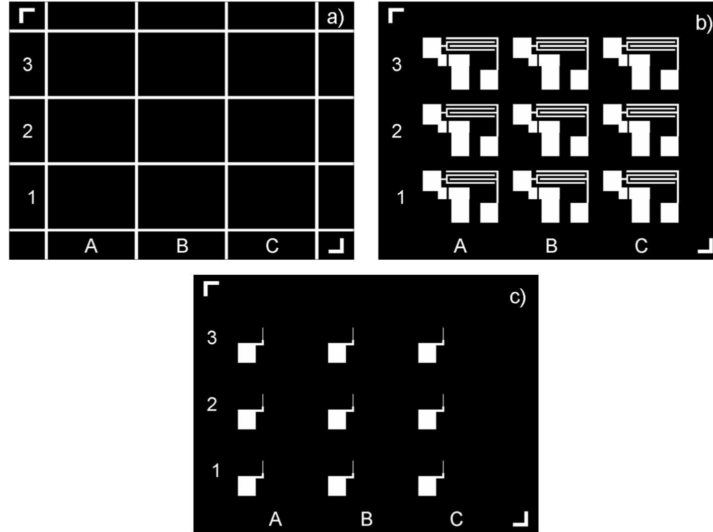

Figure 6.30: The different masks used for the fabrication of our FETs. a)Mesa structure b)Source and Drain contacts c)Gate contact.

Optical lithography means in this case that the model of the masks is converted to a bitmap data file and then projected onto the glass with a conventional beamer. Then the resist is exposed by the light of the beamer. After fixing the resist with a conventional developer, the Ni layer is etched for t=60s at room temperature using a solution of 500g Ammoniumcernitrat, 87.5ml ethanioc acid and 2.5l DI water. At the end it is rinsed in DI water and dried with pure nitrogen. This home-made mask is used for the fabrication of the FET structures.
For the fabrication of the FET structures an AlGaN/GaN heterostructure grown on carbonized Si substrate is used. A sketch of the structure and the Mesa arrangement is given in Fig. 6.31a. The FET bases on the sample GANS1416. On top of a carbonized Si substrate a 980nm thick, unintentional doped GaN buffer is deposited at a substrate temperature of 720°C. After that an AlGaN layer with a Al mole fraction of x=0.3 and a thickness of 20nm is grown using the same temperature without intentional doping. The sample is capped with a 20nm thick GaN layer. The Mesa structure is realized using reactive ion etching (RIE) technique [86]. The sample is etched in an Ar:$SiCl_4$=1:1 gas mix using a flow of 74sccm for both gases. The rf power is 1.4kW and the background pressure is about p=$2.5 * 10^{-2} mbar$. The temperature of the sample is about T=$20°C$. The etching rate for the GaN and AlGaN is about 1nm/min and the etched depth is 50nm. This guarantees, that the 2DEG of each structure is separated from the others. In the next step the source and drain contact are deposited by thermal evaporation using In as contact material. The thickness of the In is about 200nm, in order to prevent the structure of mechanical damage and to guarantee a small contact resistance. At last the gate contact is realized by thermal evaporation using Ni as Schottky contact material with a thickness of 50nm. Nine structures are fabricated on the sample in an

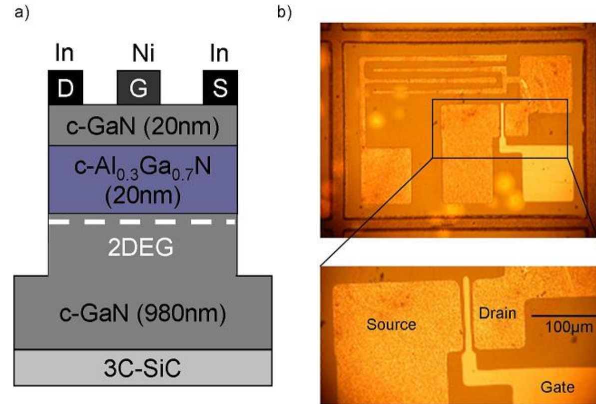

Figure 6.31: a)A schematic sketch of the FET structure and the Mesa arrangement realized on GANS1416, b)An optical micrograph with the contacts and an enlargement of the gate region (GANS1416).

arrangement of 3x3.
Figure 6.31b shows an optical micrograph of the whole MESA structure with the contact arrangement and an enlargement of the gate region. The MESA with a size $575\mu m$x$865\mu m$ can clearly be seen. The separation of the MESA is about $40\mu m$. The enlargement of the photo shows the gate region. The gate with a width of $100\mu m$ and a length of $6\mu m$ is also observed. The channel length (the separation between source and drain) is about $18\mu m$.
Before the feature of the FET is characterized, the sample is cooled down to a temperature of T=155K. This temperature guarantees on the one hand that the parallel conductivity in the GaN buffer is reduced by some orders of magnitude in order to ensure, that the conductance of the 2DEG is maybe the dominant contribution. On the other hand it allows the use of our tip prober in a modified setup. Therefore a box with a brass block was designed, which is cooled down with liquid nitrogen and on which the sample is mounted. The temperature is controlled by a thermocouple. The box posses some slits for the positioning of the tips and it is closed with a glass plate in order to look to the sample. The box is rinsed with nitrogen gas to prevent the humidity of the air from the sample and the tips.
After the sample preparation the measurements are performed in the same way as at room temperature. Before the field effect is investigated the source-gate and the source-drain I-V curves are checked. In Fig. 6.32 the source-gate I-V curve of the FET structure B-1 fabricated on GANS1416 is plotted in a linear scale for voltages between -4V and +4V. The curve is measured at a temperature of T=155K. A clear Schottky behaviour for this gate contact was observed. One can see a linear increase of the current up to 0.35mA as function of the forward bias for voltages above V_{bi}=1.7V. This value of V_{bi} is

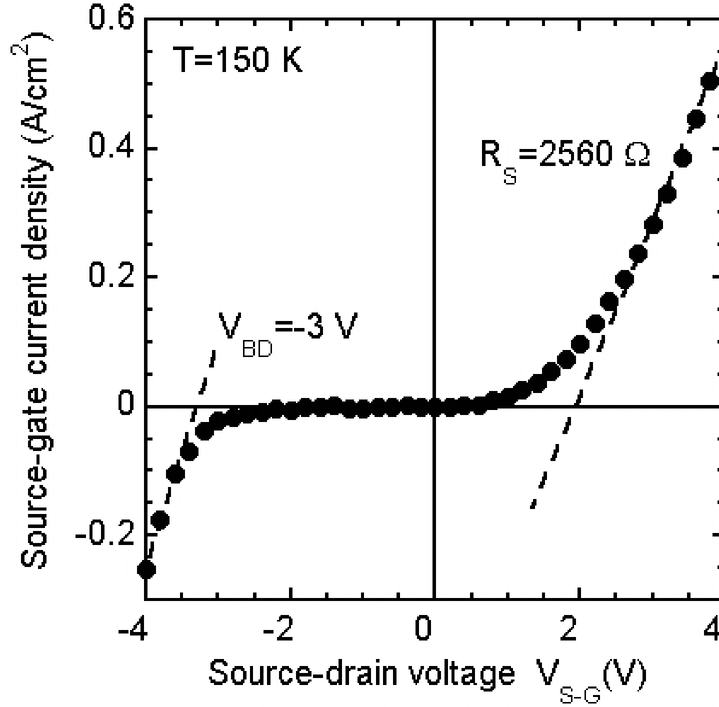

Figure 6.32: Source-gate I-V curve of FET structure B-1 realized on GANS1416 measured at a temperature of T=155K.

nearly a factor of 2 higher than on conventional Ni/c-GaN Schottky diodes and maybe correlated to a high background doping of $N_D = 10^{18}cm^{-2}$ (compare GANS1429). The serial resistance of the structure is about 6052Ω which is one order of magnitude higher than for the conventional samples. This can maybe explained by the dominance of the contact resistance on the serial resistance, because for these structures the contact area is reduced by a factor of 5. In reverse direction we found a nearly constant reverse current of -0.02mA for voltages down to -3.5V. At voltages below -3.5V a clear breakdown is observed by the increase of the current from -0.02mA to -0.2mA at a voltage of -4V. This fast breakdown occurs due to the high backround doping (compare Fig. 4.20).

In the Fig. 6.33 the source-drain I-V curve of FET structure B-1 measured at a temperature of T=155K is depicted in a linear scale using a gate voltage of V_G=0V. The current is measured at voltages between 0V and +7V. A linear increase of the current up to 2.7mA is observed for voltages up to 7V. The slope of the curve reveals a series resistance of $R_S = 2560\Omega$. This is quite high in comparison to our other Schottky diodes, but it is due to the partial freeze out of carriers and to the strong reduction of the contact area by one order of magnitude. Nevertheless the contacts can be used for the measurements.

Figure 6.34 shows a sketch of the current circuit used for the measurement of the source-drain current at different gate voltages. The source contact is set to negative potential for the source-drain measurement as well as for the control of the gate voltage, so the

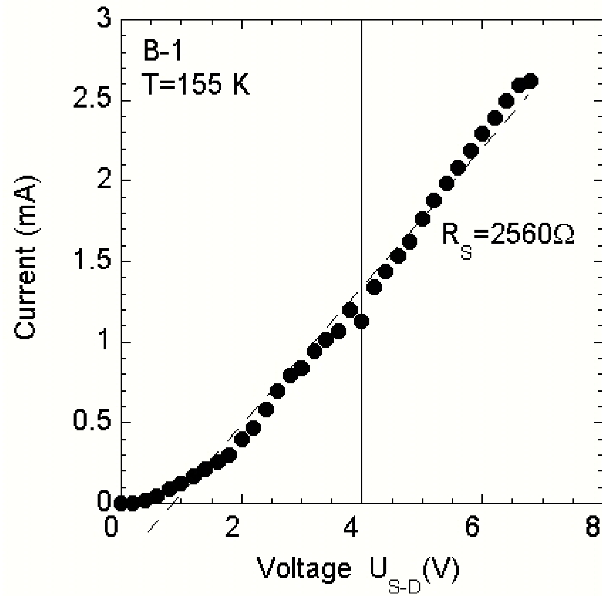

Figure 6.33: Source-drain I-V curve of FET structure B-1 realized on GANS1416 measured at a temperature of T=155K.

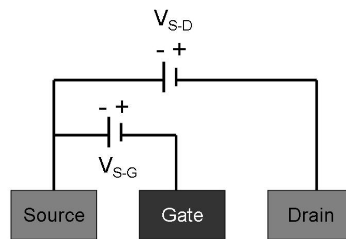

Figure 6.34: Current circuit used for the investigation of the field effect at our FET structure.

gate and drain contacts are set to positive potential, which can be independently controlled from each other. Then gate voltages between -0.25V and +1V were applied and the source-drain voltage source-drain current characteristics are measured as a function of the gate voltage. The results of these measurements are depicted in Fig. 6.35. The source-drain voltage is varied in a range between 0V and +7V. For all the I-V curves the linear increase of the current is observed with increasing voltage. The results are comparable to those measured on h-AlGaN/GaN FETs without a seminsulating buffer [87]. In addition the plot shows, that the slope of the source-drain current varies as function of the source-gate voltage. With increasing gate voltage from +0.25V and further to 0.75V and 1V the slope also increases caused by the field-effect of the gate. This is the first

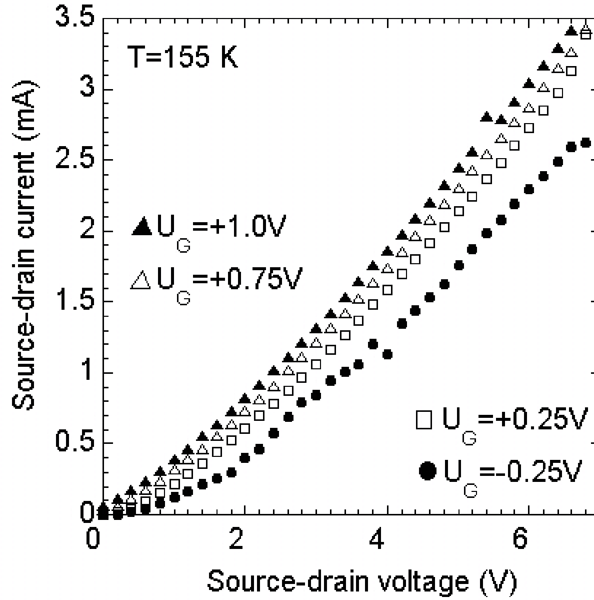

Figure 6.35: Source-drain I-V curve of FET structure B-1 for different gate voltages between -0.25V and +1V realized on GANS1416 measured at a temperature of T=155K.

hint of a field-effect operation in c-AlGaN/GaN based FET structures. Nevertheless, there are two differences to conventional FETs. The first one is, that no saturation in the source-drain current is observed, which we believe, is due to a non-neglegtable part of the current caused by parallel conductivity in the GaN buffer.

In order to investigate the influence of the buffer conductivity, the banddiagrams were

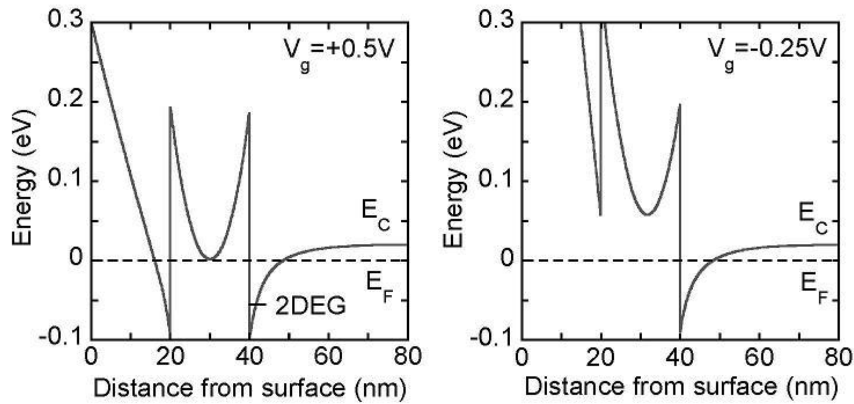

Figure 6.36: Calculated banddiagrams of the FET structure for V_G=+0.5V and V_G=-0.25V.

calculated for gate voltages of +0.5V and -0.25V. The results are plotted in Fig. 6.36.

A more detailed description of the band edge curvate is given in Fig. 6.3. The calculation of the band diagrams for the applied gate voltages shows, that at V_G=-0.25V a 2DEG ground state does not exsist. In this case the current transport is only realized by the GaN buffer. For a gate voltage of 0.5V the exsistence of a 2DEG ground state is investigated and therefore a parallel conducting of the current via the GaN buffer and the 2DEG is measured.
Therefore the source-drain current-source-drain voltage curve for a gate voltage of -0.25V is substracted from each other and then plotted again as function of the gate voltage. The results are shown in Fig. 6.37. Neglecting the influence of the GaN buffer, we can observe a clear field-effect behaviour of our FET structure. An additional feature is, that

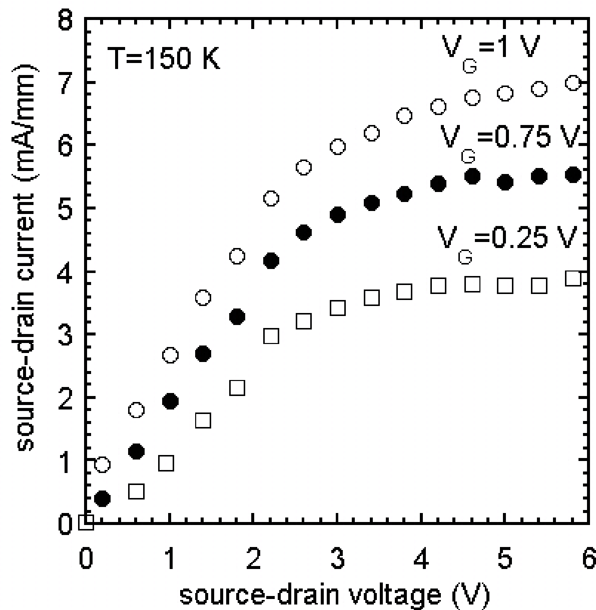

Figure 6.37: Source-drain I-V curve of FET structure B-1 for different gate voltages between +0.25V and +1V without the influence of the buffer conductivity realized on GANS1416 measured at a temperature of T=155K.

a saturation of the drain current occurs at voltages above 3V, which is a clear evidence for the current transport via a 2DEG. At this voltage the channel reaches the maximum filling level with carriers and an increase of voltage cannot increase the current. The saturation current increases as function of the gate voltage due to the increasing depth of the 2DEG channel. If we compare the saturation voltage of 3V and the saturated drain current of 0.38mA (V_G=+0.25V) to 0.70mA (V_G=+1.00V) with data of hexagonal based AlGaN/GaN FETs [88], we find that the values are in the same range. Here a saturation voltage of 3V and a drain current in the order of 1mA is typical, if the gate voltage is varied in the same range.

7 Conclusion

Phase-pure cubic GaN films on freestanding 3C-SiC (001) substrates were grown by rf plasma-assisted molecular beam epitaxy. AFM investigations showed that the RMS roughness directly depend on the defect density of the samples, due to the formation of grooves on the surface by the domain defects. Best values were obtained for wafers with a rocking curve half width of 4.5arcmin, which had a RMS roughness of 1.8nm. It was demostrated, that the properties of the substrate directly influenced the quality of the GaN buffer.
Using the best substrates, 600nm thick c-GaN films with a rocking curve width of 20arcmin and a RMS of 5.2nm could be realized. For these parameters the influence of the buffer type as well as the growth temperature were investigated. It was found, that a 8nm thick c-AlN buffer, deposited at $T_{Subs} = 720°C$ revealed the smoothest surface. With the variation of the growth temperature one can show, that the rocking curve half width decreased with increasing temperature, on the other hand the RMS roughness increased. Both were caused by the increasing surface mobility of the Ga at higher temperatures. For a growth temperature of $T_{Subs} = 720°C$, a rocking curve width of 20arcmin and a RMS of 5.2nm was obtained. The phase purity of the c-GaN was better than 99.5%.
On top of the optimized c-GaN, cubic-$Al_xGa_{1-x}N$ films ($0 < x < 0.74$) were deposited. Measurements of the RHEED intensity were employed in order to obtain well defined metal-rich growth conditions. The Al content of our layers was directly proportional to the Al flux while the roughness of the layers was strongly depending on the excess Ga-coverage during growth. Lowest values of the RMS roughness which was independent of the Al content x were obtained with a 1ML coverage. Pronounced oscillations of the RHEED intensity which were observed after growth interruptions indicate predominant two-dimensional growth of our c-$Al_xGa_{1-x}N$ films. It was found, that the background doping of the AlGaN increased with increasing Al content, due to the high affinity of oxygen to Al. The level increased from $N_D = 1*10^{17}cm^{-3}$ for GaN to $N_D = 2*10^{18}cm^{-3}$ for a $Al_{0.45}Ga_{0.55}N$ layer. The conductivity of our AlGaN films increased by a factor of 3 at x=0.45 in comparison to GaN and then decreased by one order of magnitude for c-AlN, caused by the increasing activation energy of the oxygen impurity.
The c-GaN and c-AlGaN films were used to realize Schottky diodes by the deposition of Ni as contact material. Temperature dependent I-V measurements showed a strong deviation between the classical thermionic emssion theory and the current flow in our structures. The high leakage current, which was observed, originated in the presence of surface donor states with a concentration of $N_{SD} = 2 * 10^{19}cm^{-3}$ at room temperature. Temperature dependent C-V analysis revealed a ionization energy between 14meV and 23meV. It was demonstrated that the surface donors can be influenced by thermal an-

nealing. Using a temperature of $200°C$ for 10min the leakage current was reduced by three orders of magnitude and the breakdown voltage increased by one order from -9V to -80V. The breakdown voltage directly depend on the background concentration of the films.
Therefore cubic $Al_xGa_{1-x}N/GaN$ heterostructures were fabricated by MBE on 3C-SiC (001) substrates. An additional luminescence band at 3.250eV was observed at low temperature which was attributed to a 2DEG transition. The position of the luminescence was influenced by the Al content and the background doping of the AlGaN barrier. Intensity dependent and voltage dependent PL measurements showed characteristic shifts of this transition of 3.3meV/decade and 1.3meV/V, respectively, due to the change in the carrier confinement by varying the laser excitation power or the external bias voltage. These shifts are quantitatively verified by a self consistent solution of the Schrödinger and Poisson equation. C-V measurements at T=150K reveal a clear evidence for the existence of a 2DEG, and a sheet carrier concentration of about $1.6 * 10^{12} cm^{-2}$ is measured at the interface in good agreement with the numerical simulation. Temperature dependent Hall-effect analysis revealed a carrier mobility of $100 cm^2 (Vs)^{-1}$ at 5K for the 2DEG. The influence of different scattering mechanisms like phonon, impurity, dislocation or roughness scattering was investigated. It was found, that the mobility of the 2DEG was limited by scattering at the interface roughness. Then c-AlGaN/GaN based HFET structures were fabricated. The MESA structures were realized by RIE technique. The source and drain contacts were made from pure In, for the gate contact Ni was used. The samples were prepaired for device operation. The presence of the field effect operation was demonstrated at a temperature of 155K.

Bibliography

[1] L. Shen, R. Coffie, D. Bultari, S. J. Heikman, A. Chakraborthy, A. Chini, S. Keller, S. P. DenBaars and U. K. Mishra, IEEE Elec. Div. Lett. **25**, 7 (2004)

[2] S. Rajan, P. Waltereit, C. Poblenz, S. J. Heikman, D. S. Green, S. P. DenBaars and U. K. Mishra, IEEE Elec. Div. Lett. **25**, 247 (2004)

[3] M. D. Craven, P. Waltereit, F. Wu, J. S. Speck, and S. P. DenBaars, Jpn. J. Appl. Phys. **42** L235 (2003)

[4] P. Waltereit, O. Brandt, A. Trampert, H. T. Grahn, J. Menniger, M. Ramsteiner, M. Reiche, and K. H. Ploog, Nature (London) **406**, 3850 (2000)

[5] H. M. Ng, Appl. Phys. Lett. **80**, 4369 (2002)

[6] S. Potthast, J. Schörmann, J. Fernandez, D. J. As, K. Lischka, H. Nagasawa and M. Abe, phys. stat. sol. (c), **3**, No 6, 2091 (2006)

[7] J. Schörmann, S. Potthast, D.J. As, and K. Lischka, Appl. Phys. Lett. (accepted)

[8] D. J. As, in *Optoelectronic Properties of Semiconductors and Superlattices*, series editor M. O. Manasreh, (Taylor and Francis Books, Inc. , New York, 2003), Vol. **19** chapter 9, pp. 323-450

[9] I. Petrov, E. Mojab, R. C. Powell and J. E. Greene, Appl. Phys. Lett. **60**, 2491 (1992)

[10] T. Lei, M. Fanciulli, R. J. Molnar, T. D. Moustakas, R. J. Graham and J. Scanlon, Appl. Phys. Lett. **59**, 944 (1991)

[11] S. K. Pugh, D. J. Dugdale, S. Brand and R. A. Abram, Semicond. Sci. Techn. **14** (1), 23 (1999)

[12] C. G. van de Walle and J. Neugebauer, Appl. Phys. Lett. **70** (19), 2577 (1997)

[13] K. Kim, W. R. L. Lambrecht and B. Segall, Phys. Rev. **B53** (24), 16310 (1996)

[14] S. H. Park and S. L. Chuang, J. Appl. Lett. **87** (1), 353 (2000)

[15] J. W. Matthews and A. E. Blakeslee, J. Cryst. Growth **27**, 118 (1974)

[16] M. E. Sherwin and T. J. Drummond, J. Appl. Phys. **69**, 8423 (1991)

[17] M. A. Herrmann and H. Sitter *Molecular Beam Epitaxy: Fundamentals and current status*, Springer Verlag, Berlin 1989

[18] B. Schöttker *Molecular Beam Epitaxie and Characterization of doped and undoped cubic GaN Layers*, Ph.D. thesis, Shaker Verlag Aachen 1999

[19] J. Schörmann, S. Potthast, M. Schnietz, S. F. Li, D. J. As and K. Lischka, phys. stat. sol. (c), No 6, 1604 (2006)

[20] H. Beneking *Halbleitertechnologie*, Teubner Verlag Stuttgart (1991)

[21] Brodie, J. J. Murray *Semiconductor Microfabrication*, New York 1982

[22] W. M. Moreau *Semiconductor Lithography, Principles, Practices and Materials*, New York (1993)

[23] B. E. Warren, *X-ray diffraction*, Dover, New York 1968

[24] L. Pavesi, M. Guzzi, J. Appl. Phys. , **75**, 4779 (1994)

[25] P.Y. Yu, M. Cardona, *Fundamentals of Semiconductors*, Springer Verlag, Berlin, Heidelberg 1996

[26] C.F. Klingshirn *Semiconductor Optics*, Springer Verlag, Berlin Heidelberg 1995

[27] E. F. Schubert, *Doping in III-V Semiconductors*, University Press, Cambrigde 1993

[28] S. M. Sze *Physics of Semiconductor devices*, John Wiley and Sons, New York 1981

[29] D. C. Look *Electrical Characterization of GaAs Materials and Devices*, John Wiley and Sons, New York 1989

[30] D. K. Schroder *Semiconductor Material and Device Characterzation*, Wiley Interscience, 1998

[31] R. A. Bowling and G. B. Larrabee, *Surface Characterization*, Anal. Chem. **55** 133R-156R, (1983)

[32] R. A. Bowling and G. B. Larrabee, *Surface Characterization*, Anal. Chem. **57** 130R-175R, (1985)

[33] G. E. McGuire *Surface Characterization*, Anal. Chem. **59** 294R-308R, (1987)

[34] R. E. Honig, *Surface and Thin Film Analysis of Semiconductor Materials*, Thin Solid Films **31**, 89 (1976)

[35] T. Wolff, M. Rapp and T. Rotter phys. stat. sol. (c) **1**, No. 10, 2417 (2004)

[36] J. Neugebauer, Z. Zywietz, M. Scheffler, J. E. Northrup and C. G. van der Walle, Phys. Rev. Lett. **80**, 3097 (1998)

[37] S. Potthast, J. Schörmann, E. Tschumak, D. J. As and K. Lischka, Jour. Appl. Phys. *submitted*

[38] D. L. Smith, *Thin Film Deposition* (McGraw-Hill, New York, 1995)

[39] J. Schörmann, S. Potthast, M. Schnietz, S. F. Li, D. J. As and K. Lischka, phys. stat. sol. (c), **3**, 1604 (2006)

[40] C. S. Lent and P. I. Cohen, Phys. Rev. B **33** (12), 8329 (1986)

[41] H. Nagasawa, T. Kawahara and K. Yagi, Mater. Sci. Forum **389-393** (2002)

[42] H. Nagasawa, K. Yagi, T. Kawahara and N. Hatta, Mater. Sci. Forum **433-4** (2002)

[43] W. A. Harrison, *Electronic Structure and the Properties of Solids* (Dover, New York, 1980)

[44] J. Neugebauer, T. Zywietz, M. Scheffler, J. E. Northrup, H. Chen and R. M. Feenstra, Phys. Rev. Lett. **90**, 056101 (2003)

[45] C. Adelmann, R. Langer, G. Feuillet and B. Daudin Appl. Phys. Lett. **75**, (22), 3518 (1999)

[46] J. H. Edgar, S. Strite, I. Akasaki, H. Amano and C. Wetzel *Galluim Nitride and related Semiconductors*, INSEPC 1999

[47] M. Stutzmann, O. Ambacher, A. Cros, M. S. Brandt, H. Angerer, R. Dimitrov, N. Reinacher, T. Metzger, R. Höpler, D. Brunner, F. Freudenberg, R. Handschuh and Ch. Deger, Mat. Sci. Eng. **50**, 212 (1997)

[48] A. C. Smitz, A. T. Ping, M. Asif Khan, Q. Chen, J. W. Yang and I. Adesida, Semicond. Sci. Technol. **11**, 10,1464 (1996)

[49] J. H. Edgar *Properties of Group III Nitrides*, INSPEC, Short Run Press Ltd. Exeter (1994)

[50] J. Singh, *Physics of Semiconductors*, Mc Graw Hill, (1997)

[51] H. A. Bethe, *Theory of the boundary layer of crystal rectifiers*, MIT Radiat. Lab. Rep. 43-12 (1942)

[52] J. Fernandez, *Growth and Characterization of c-GaN based Schottky diodes*, Master thesis (2005)

[53] D. J. As, S. Potthast, J. Fernandez, J. Schörmann and K. Lischka, Appl. Phys. Lett. **88** 152112 (2006)

[54] J. H. Werner, Appl. Phys. **A47**, 291 (1988)

[55] S. N. Mohammad, J. Apl. Phys. **97**, 063703 (2005)

[56] V. Adivarahan, G. Simin, J. W. Yang, A. Lunev, M. A. Kahn, N. Pala, M. Shur and R. Gaska Appl. Phys. Lett. **77**, 862 (2000)

[57] J. D. Guo, M. S. Feng, R. J. Guo, F. M. Pan and C. Y. Chang, Appl. Phys. Lett. **67**, 2657 (1995)

[58] A. C. Schmitz, A. T. Ping, M. A. Kahn, Q. Chen, J. W. Yang and I. Adesia J. Electron. Mater. **27**, 255 (1998)

[59] D. K. Schroder *Semiconductor Material and Device Characterization*, Wiley, New York 1990

[60] H. Hasegawa and S. Oyama, J. Vac. Sci. Technol. **B 20**, 1647 (2002)

[61] J. M. Langer and P. Revva, Mat. Sci. Forum **83-87**, 1545 (1992)

[62] J. M. Langer, Jpn. J. Appl. Phy. **32**, Suppl. 32-1, 83 (1993)

[63] P. Revva, J. M. Langer, M. Missous and A. R. Peaker J. Appl. Phys **74** (1), 416 (1993)

[64] F. A. Padovani and R. Stratton, Solid-State Electron. **9**, 695 (1966)

[65] J. D. Guo, F. M. Pan, M. S. Feng, R. J. Guo, P. F. Chou and C. Y. Chang, J. Appl. Phys. **80**, 1623 (1996)

[66] K. Matocha, T. P. Chow and R. J. Gutmann, Mater. Sci. Forum **383-393**, 1531 (2002)

[67] J. J. Bandic, P. M. Bridger, E. C. Piquette and T. C. McGill, Appl. Phys. Lett. **74**, 1266 (1999)

[68] G. T. Dang, A. P. Zhang, M. M. Mshewa, F. Ren, J. I. Chyi, C. M. Lee, C. C. Guo, G. C. Chi, J. Han, S. N. G. Chu, R. G. Wilson, X. A. Cao and S. J. Pearton, J. Vac. Sci. Technol. A **18**, 1135 (2000)

[69] Y. -Z. Chiou, Y. K. Su, S. -J. Chang and C. -H. Chen, IEE Proc. Optoelectron. , Vol. 150, No. 2, (2003)

[70] C. K. Wang, S. J. Chang, Y. K. Su, Y. Z. Chiou, C. S. Chang, T. K. Lin, H. L. Liu and J. J. Tang, Semicond. Sci. Technol. **20**, 485-489, (2005)

[71] J. H. Davies *The Physics of Low Dimensional Semiconductors*, Cambridge University Press, 1997

[72] A. Nakadaira and H. Tanaka, Appl. Phys. Lett. **70** (20), 2720 (1997)

[73] S. Müller, K. Köhler, R. Kiefer, R. Quay, M. Baeumler and L. Kirste, phys. stat. sol. (c),**2**, No 7, 2639 (2005)

[74] I. H. Tan, G. Snider and E. L. Hu, J. Appl. Phys. **68**, 4071 (1990)

[75] D. J. As, F. Schmilgus, C. Wang, B. Schöttker, D. Schikora and K. Lischka, Appl. Phys. Lett. **70**, 1311 (1997)

[76] Y. R. Yuan, M. A. A. Pudensi, G. A. Vawter and J. L. Merz, J. Appl. Phys. **58**, 397 (1985)

[77] G. Ramirez-Flores, H. Navarro-Contreras, A. Lastras-Martinez, R. C. Powell and J. E. Greene, Phys. Rev. B **50**, 8433 (1994)

[78] S. R. Kurtz, A. A. Allerman, D. D. Koleske, A. G. Baca, R. D. Briggs, J. Appl. Phys. **95** 4 (2004)

[79] V. Cimalla, Th. Stauden, G. Eichhorn, J. Petzold; Mat. Sci. Eng. **B61-62**, 553-558 (1999)

[80] L. Hsu and W. Walukiewcz, Phys. Rev. B **56**, No 3, 1520 (1997)

[81] X. Han, D. Li, H. Yuan, X. Sun, X. Liu, X. Wang, Q. Zhu and Z. Wang, phys. stat. sol. (b) **241**, No 13, 3000 (2004)

[82] F. A. Ponce, MRS Bull. **22**, 51 (1997)

[83] D. Jena, A. Gossard and U. K. Mishra, Appl. Phys. Lett. **76** (13), 1707 (2000)

[84] N. G. Weimann, L. F. Eastman, D. Doppalapudi, H. M. Ng and T. D. Moustakas J. Appl. Phys. **83**, 7, 3656 (1998)

[85] V. V. Mitin, V. A. Kochelap and M. A. Stroscio in *Quantum Heterostructures-Microelectronics and Optoelectronics*, p.249 Cambridge University Press (1999)

[86] M. Panfilova *Reactive Ion Etching and Photoenhanced Wet Chemical Etching of cubic group-III Nitrides* Masterthesis (2006)

[87] C. Poblenz, P. Waltereit, S. Rajan, S. Heikman, U. K. Mishra and J. S. Speck, Jour. Vac. Sci Technol. B **22** (3), 1145 (2004)

[88] D. Kikuta, J. P. Ao and Y. Ohno, Sol. Stat. Elec. **50**, 316 (2006)

List of samples

Sample	Subs.	$T_{GaN}(°C)$	$t_{GaN}(nm)$	$T_{AlGaN}(°C)$	$t_{AlGaN}(nm)$	x
GNSJ951	SiC	720	628			
GNSJ953	SiC	750	623			
GNSJ954	SiC	780	643			
GNSJ955	SiC	810	607			
GNS982	SiC	720	595			
GNSK987	SiC	720	580			
GNSK988	SiC	720	560			
GANJ998	SiC	720	354	720	300	0.22
GANJ1000	SiC	720	400	720	360	0.22
GANJ1001	SiC	720	400	720	440	0.22
GANJ1005	SiC	720	420	720	160	0.22
GANJ1006	SiC	720	390	720	90	0.22
GANJ1007	SiC	720	400	720	50	0.22
GANS1034	SiC	720		720		0.18
GANS1052	SiC	720	270	720	300	0.25
GANS1074	SiC	720	240	720	480	0.52
GNSC1108	SiC	720	70	720	540	0.20
GNS1183	SiC	720	780			
GNJ1204	SiC	720	850			
GANS1211	SiC	720	520	720	540	0.25
GANS1228	SiC	720	900	720	90	0.25
GANS1239	SiC	720	900	720	90	0.30
GNS1285	SiC	720	850			
GANS1352	Si	720	800	720	40	0.35
GANS1356	Si	720	800	720	40	0.35
GANS1357	Si	720	800	720	40	0.35
GNS1382	SiC	720	755			
GANS1384	SiC	720	750	720	20	0.35
AGN1397	SiC	675		675		0.33
AGN1398	SiC	700		700		0.44
AGN1403	SiC	725		725		0.57
GANS1416	Si	720	980	720	20	0.30

Sample	Subs.	$T_{GaN}(^{\circ}C)$	$t_{GaN}(nm)$	$T_{AlGaN}(^{\circ}C)$	$t_{AlGaN}(nm)$	x
AGN1426	SiC	700		725 700		0.14 0.25 0.38 0.67
GNP1429	SiC	720	740	720	20	0.35
AGN1436	SiC	700		700		0.18 0.32 0.52
AGN1437	SiC	700		700		0.80
AGN1441	SiC	735		735		0.74
AGN1445	Si	690		690		0.44
AGN1447	SiC	640		640		0.48
AGN1448	SiC	700		700		0.54
AGN1449	Si	700		700		0.54
AGN1452	SiC	725		725		0.54
AGN1455	SiC	720		720		0.63
AGN1459	SiC	745		745		0.82
AGN1463	SiC	750		750		0.65

Acknowledgements

This is the last chapter of my thesis, which I have to write down, and believe me, it will be the most difficult. This Ph. D. thesis would have been much harder to do and to finish without the help, support, contributions and encouragement of many people, who I have to mentioned here.
First I have to thank Prof. Dr. D. J. As, who offered me this interesting, fascinating work, which contains the field of basic research and device physics, as well as entailed engineering. Without his support it would not be possible to solve the problem he gave me (cite: The goal is a HEMT device!). I will not forget to thank Prof. K. Lischka and Dr. D. Schikora for sharing their own experiences, knowledge and readiness to engage in sometimes rather longish discissions (especially on friday!).
The next I have to mentioned are my dear colleagues of the last years. At first I have to name my earlier Diplom student and office partner J. Schörmann. I thank him for everything (this includes: correcting my thesis, growing samples for my thesis, the sweets, the after-work beers...)!
In addition I would like to thank my other fellow Ph. D. students C. Arens and S. Preuss for the physical and technical discussions made many things clearer to myself (especially Ohms law!). I will not forget our Postdoc Dr. A. Pawlis, who shows me that life continious after finishing of the Ph. D. thesis.
And I have also to named the Diplom students M. Schnietz, C. Peitzmeyer and D. Mügge, they are not present anymore, but I would thank them also for the discussions and the social events.
And last but not least, here comes the special section for our ladies! I did not forget them, my favoured Bachelor student M. Panfilova, my favoured Master student J. Fernandez and my favoured Ph. D. student E. Tschumak. I thank them for showing me and the rest of the group that women exist, who study physics and for the sucessful and unsucessful discussions we had, for the cakes, apples and icecream...
I will thank all of you for the last years and the friendly atmosphere in the group- I will definitely miss everybody!
Of course I am also grateful for the (not only technical) help of our optoelectronics staff, I. Zimmermann, S. Igges and B. Vollmer.
At the end I would like to thank my parents for more than thirty years of endless patience, help and support.

Publication list

D. J. As, U. Köhler, **S. Potthast**, A. Khartchenko, and K. Lischka, V. Potin and D. Gerthsen *Cathodoluminescence, high-resolution x-ray diffraction and transmission-electron-microscopy investigations of cubic AlGaN/GaN quantum wells*, phys. stat. sol. (c) 0, **no. 1**, 253-257 (2002)

O. C. Noriega, J. R. Leite, E. A. Meneses, J. A. N. T. Soares, S. C. P. Rodrigues, L. M. R. Scolfaro, G. M. Sipahi, U. Köhler, D. J. As, **S. Potthast**, A. Khartchenko and K. Lischka *Photoluminescence and photoreflectance characterization of cubic GaN/AlxGa1-xN quantum wells*, phys. stat. sol. (c) 0, **no. 1**, 528 (2002)

U. Köhler, D. J. As, **S. Potthast**, A. Khartchenko, K. Lischka, O. C. Noriega, D. G. Pachenco-Salazar, A. Tabata, S. C. P. Rodrigues, L. M. R. Scolfaro, G. M. Siphari, J. R. Leite *Optical charachterization of cubic AlGaN/GaN quantum wells*, phys. stat. sol. (a) 192 **(1)**, 129 (2002)

D. J. As, **S. Potthast**, U. Köhler, A. Khartchenko and K. Lischka *Cathodoluminescence of MBE-grown cubic AlGaN/GaN multi-quantum wells on GaAs (001) substrates* MRS Symp. Proc. Vol. **743** L5.4 (2003)

J. R. L. Fernandez, F. Cerdeira, E. A. Meneses, M. J. S. P. Brasil, J. A. N. T. Soares, A. M. Santos, O. C. Noriega, J. R. Leite, D. J. As, U. Köhler, **S. Potthast**, and D. G. Pacheco Salazar *Optical and x-ray studies on the incorporation of carbon as a dopant in cubic GaN*, Phys. Rev. B **68**, 155204 (2003)

D. J. As, D. G. Pacheco Salazar, **S. Potthast** and K. Lischka *Carbon doping of cubic GaN under gallium-rich growth conditions*, phys. stat. sol. (c) 0, **no. 7**, 2537-2540 (2003)

D. J. As, D. G. Pacheco-Salazar, **S. Potthast**, K. Lischka *Electrical and optical properties of carbon doped cubic GaN epilayers grown under extreme Ga excess*, MRS Symp. Proc. Vol. **798**, Y8.2 (2004)

R. Goldhahn, C. Buchheim, V. Lebedev, V. Cimalla, O. Ambacher, C. Cobet, M. Rakel, N. Esser, U. Rossow, D. Fuhrmann, A. Hangleiter, **S. Potthast**, and D. J. As *Dielectric function and critical points of the band structure for hexagonal and cubic GaN and AlN*, BESSY (Berliner Elektronenspeicherring-Gesellschaft fr Synchrotronstrahlung m.b.H.) Annual Report 2005, ed. K. Godehusen, p. 206

D. J. As, **S. Potthast**, J. Fernandez, K. Lischka, H. Nagasawa, M. Abe *Cubic GaN/AlGaN Schottky-barrier devices on 3C-SiC substrates*, Microelectronic Engineering **83** (2006) 34-36

D. J. As, **S. Potthast**, J. Fernandez, J. Schörmann, and K. Lischka *Ni Schottky diodes on cubic GaN*, Appl. Phys. Lett. **88**, 1521112 (2006)

S. Potthast, J. Schörmann, J. Fernandez, D. J. As, K. Lischka, H. Nagasawa, M. Abe *Two-dimensional electron gas in cubic AlxGa1-xN/GaN heterostructures*, phys. stat. sol. (c) 3,**No. 6**, (2006) 2091

J. Schörmann, **S. Potthast**, M. Schnietz, S. F. Li, D. J. As, and K. Lischka *Growth of ternary and quaternary cubic III-nitrides on 3C-SiC substrates*, phys. stat. sol. (c) 3, **No. 6** (2006) 1604

D. J. As, **S. Potthast**, J. Fernandez, K. Lischka, H. Nagasawa, M. Abe *Mechanism of current leakage in Ni Schottky diodes on cubic GaN and AlxGa1-xN epilayers*, MRS Symp. Proc. Vol. 892, 283 FF 13.4.1 (2006)

D. J. As, **S. Potthast**, J. Schörmann, S. F. Li, K. Lischka, H. Nagasawa, M. Abe *Molecular beam epitaxy of cubic group III-Nitrides on free-standing 3C-SiC substrates*, Mat. Sci. Forum Vol. 527-529, 1489 (2006)

M. Abe, H. Nagasawa, **S. Potthast**, J. Fernandez, J. Schörmann, D. J. As, and K. Lischka *Cubic GaN/AlGaN HEMTs von 3C-SiC substrate for normally-off operation*, IEICE Trans. Electron. Vol.E89-C, **No. 7**, 1057 (2006)

J. Schörmann, **S. Potthast**, D. J. As, and K. Lischka *Near UV emission from nonpolar cubic AlxGa1-xN/GaN Quantum Wells*, Appl. Phys. Lett. 2006 (accepted)

S. Potthast, E. Tschumak, J. Schörmann, D. J. As, and K. Lischka *Growth and Properties of nonpolar cubic $Al_xGa_{1-x}N$ films*, Jour. Appl. Phys. (submitted)